# X-ray photon correlation spectroscopy experiments of protein dynamics at molecular length scales - potentials and limitations.

DISSERTATION

zur Erlangung des Grades eines Doktors

der Naturwissenschaften

vorgelegt von

M.Sc. Mohammad Sayed Akhundzadeh

eingereicht bei der Naturwissenschaftlich-Technischen Fakultät

der Universität Siegen

Siegen 2023

Erster Gutachter und Betreuer:
Prof. Dr. Christian Gutt
Universität Siegen

Zweiter Gutachter:
Prof. Dr. Foivos Perakis
Universität Stockholm

Tag der mündlichen Prüfung:
18.01.2024

# Abstract

Protein dynamics play an essential role in the functionality of biomolecules, and their behavior within dense environments presents a fascinating and complex field of study. Various factors, such as macromolecular crowding agents, have an impact on the dynamics of proteins in crowded conditions. Protein dysregulation in crowded cellular environments is associated with pathological conditions such as neurodegenerative diseases and blindness. The investigation of protein dynamics in solution plays a key role in various disciplines, including biophysics and pharmaceuticals, as it provides insights into essential aspects of protein behavior, aggregation, and interactions. However, due to the experimental challenges related to measuring dynamics on a molecular-length scale, the dynamics are still mostly unknown.

X-ray photon correlation spectroscopy (XPCS) has been considered an excellent technique for investigating protein dynamics at molecular-length scales. This thesis provides a comprehensive description of a current study that explores the potential and limitations related to the use of XPCS to determine the dynamics of protein solutions (specifically IgG+PEG and BSA+$YCl_3$) at molecular length scales. Additionally, it examines the impact of dose rate on X-ray-induced dynamics in highly concentrated antibody-protein solutions. A comprehensive understanding of the capabilities and limitations of XPCS is essential for optimizing its potential to enhance our understanding about protein dynamics and its various applications in different disciplines.

XPCS has several notable advantages, including the ability to achieve spatial resolution at the nanoscale. Additionally, XPCS demonstrates compatibility with a wide range of sample environments, encompassing aqueous and opaque solutions. Moreover, XPCS enables the determination of collective dynamics within the studied systems. Although this approach has numerous advantages, it is also constrained by a number of obstacles. This study addresses the challenges related to radiation damage, data analysis complexities, and the necessity for coherent X-ray sources.

Furthermore, this work presents a new dimension of the research, focusing on the influence

of X-ray dose rates on the corresponding dynamics in concentrated solutions of proteins. By systematically varying the dose rates, this research aims to evaluate how X-ray radiation influences protein dynamics and interactions in crowded environments. This exploration has implications for both biophysical research and the field of soft matter, where X-ray-based techniques are becoming increasingly relevant.

# Zusammenfassung

Die Dynamik von Proteinen spielt eine wesentliche Rolle für die Funktionalität von Biomolekülen, und ihr Verhalten in dichten Umgebungen stellt ein faszinierendes und komplexes Forschungsgebiet dar. Die in dichten Umgebungen herrschenden Bedingungen wirken sich dabei ganz unmittelbar auf die Dynamik von Proteinen aus. Die Untersuchung der Proteindynamik in Lösung spielt in verschiedenen Disziplinen, darunter Biophysik und Pharmazie, eine Schlüsselrolle, da sie Einblicke in wesentliche Aspekte des Verhaltens, der Aggregation und der Wechselwirkungen von Proteinen bietet. Aufgrund der experimentellen Herausforderungen, die mit der Messung der Dynamik auf der Längenskala von einigen Nanometern verbunden sind, ist insbesondere die kollektive Dynamik weitgehend unbekannt.

Die Röntgenphotonen-Korrelationsspektroskopie (XPCS) gilt als hervorragende Technik zur Untersuchung der kollektiven Proteindynamik auf diesen kleinen Längenskalen. In dieser Arbeit werden das Potenzial und die Grenzen der Verwendung von XPCS zur Bestimmung der Dynamik von Proteinlösungen (insbesondere IgG+PEG und BSA+$YCl_3$) auf molekularen Längenskalen untersucht. Zusätzlich wird der Einfluss der Dosisleistung auf die röntgeninduzierte Dynamik in hochkonzentrierten Antikörper-Protein-Lösungen untersucht. Ein umfassendes Verständnis der Möglichkeiten und Grenzen von XPCS ist für die Optimierung ihres Potenzials zur Verbesserung unseres Verständnisses der Proteindynamik und ihrer verschiedenen Anwendungen in unterschiedlichen Disziplinen unerlässlich.

XPCS hat mehrere bemerkenswerte Vorteile, darunter die Fähigkeit, eine räumliche Auflösung im Nanobereich zu erreichen. Darüber hinaus zeigt XPCS Kompatibilität mit einer Vielzahl von Probenumgebungen, darunter wässrige und undurchsichtige Lösungen. Darü-ber hinaus ermöglicht XPCS die Bestimmung der kollektiven Dynamik innerhalb der untersu-chten Systeme. Obwohl dieser Ansatz zahlreiche Vorteile hat, ist er auch durch eine Reihe von Hindernissen eingeschränkt. Diese Studie befasst sich mit den Herausforderungen im Zusammenhang mit Strahlenschäden, der Komplexität der Datena-

nalyse und der Notwendigkeit kohärenter Röntgenquellen.
Darüber hinaus stellt diese Studie eine neue Dimension der Forschung dar, die sich auf den Einfluss der Röntgendosisraten auf die entsprechende Dynamik in konzentrierten Lösungen von Proteinen konzentriert. Durch systematische Variation der Dosisraten soll untersucht werden, wie Röntgenstrahlung die Dynamik und die Wechselwirkungen von Proteinen in überfüllten Umgebungen beeinflusst. Diese Untersuchung hat Auswirkungen sowohl auf die biophysikalische Forschung als auch auf den Bereich der weichen Materie, wo röntgenbasierte Techniken zunehmend an Bedeutung gewinnen.

# Contents

# Introduction

Proteins govern essential physiological processes within the human body, and nearly all biological activities in cells are under the control of proteins [60, 126]. These entities serve as the tiny components that facilitate the functioning of the complex mechanisms of life. The description of protein structure encompasses various levels, ranging from the sequence of amino acids, which are the fundamental constituents of proteins, to a comprehensive representation that includes the three-dimensional coordinates of each atom within the protein [60]. With all of these essential functions, it's no surprise that proteins are a major field of biological study [60, 126].

Obtaining information regarding protein dynamics is crucial for understanding the functioning of organs and will serve to explain why something doesn't work properly and causes disease. The underlying causes of impaired functionality and the onset of diseases. Because protein aggregation has the potential to induce protein condensation diseases, such as eye cataracts or sickle cell anemia [21, 109]. Additionally, the presence of fibrous depositions has been observed in the brains of people affected by Alzheimer's disease [126, 82].

The proteins have the ability to undergo conformational changes and form many higher-order structures, including but not limited to liquids, glassy solids, and amyloid fibers, depending on the prevailing conditions. The condensed phases exhibit distinct characteristics in terms of molecular dynamics, internal organization, and reversibility [21, 109, 39].

The understanding of cellular mechanisms depends extensively on the study of protein diffusion occurring at length scales comparable to their own size. Furthermore, a comprehensive understanding of the dynamic characteristics of concentrated protein solutions is crucial in order to facilitate the development of future protein-based pharmaceuticals [126, 109]. The liquid-liquid phase separation (LLPS) process has many complicated parts, such as the evolution of domains into new phases, the microscopic dynamics of density fluctuations, the thermal fluctuations of domain interfaces, and the global diffusive motion [126, 77]. The problem with studying the dynamics of LLPS lies in the fact that

these dynamics may occur within a wide range of time and length scales. The observed dynamics exhibit complex non-equilibrium behaviors on length scales spanning from $\mu$m to the size of individual proteins ($\sim$ nm) and occur over a time scale ranging from 100 s to $10^{-6}$s [38, 109].

Dynamic light scattering (DLS) is a reliable technique for investigating the dynamic behavior of protein samples. However, multiple scatterings in dense and opaque environments have an impact on it and limit its ability. The remarkable brilliance provided by third-generation X-ray sources has facilitated the implementation of X-ray photon correlation spectroscopy (XPCS) investigations [108]. The advantage of XPCS in comparison to DLS is its capability to facilitate the investigation of dense and opaque samples. Additionally, XPCS enables the exploration of collective dynamics across a wide range of time scales, spanning from 100 s to $10^{-6}$ s, as well as length scales ranging from $\mu$m to nm [21, 109]. This time- and length-scale window is particularly useful in relation to protein investigations. In various soft condensed matter research areas, XPCS has been used to study the dynamics of liquids, colloids, and polymers. However, only preliminary developments have been achieved to investigate protein systems using XPCS due to the experimental challenges of working with highly beam-sensitive materials [108].

This thesis aims to demonstrate the possibility of using XPCS experiments to investigate protein dynamics on the molecular length scale. Therefore, an experiment was conducted to study the dynamics of a protein model system in an aqueous solution consisting of $\gamma$-globulin antibody (IgG) and polyethylene glycol (PEG). In order to determine the type of motion in the proteins solution, the dynamics are determined at various time and length scales. At large q-values, the system exhibits characteristic behaviors similar to ballistic motion, comparable to what is observed in colloidal gels [38]. However, the impact of the beam on the structure and the dynamics of the sample are observed.

One of the primary obstacles discovered in the implementation of Bio-XPCS experiments relates to the control of radiation-induced damage. The comprehension of the impacts of X-ray radiation on structure and dynamics has significant importance within several scientific disciplines that depend on using synchrotron sources. There are two significant paths through which X-ray-matter interactions occur: direct damage to the molecules and indirect damage, which involves the radiolysis of water and additional chemical reactions with the subsequent radiolysis side effects [109, 123]. Nevertheless, the current understanding of the processes and behaviors in action remains incomplete, mostly due to the intricate time-dependent chemical interactions and the significant exclusivity of the samples [121, 123].

The essential variables for evaluating and measuring the impacts of radiation involve the total amount and rate of absorbed energy per unit of volume (i.e., the X-ray dose, and the dose rate). Atomic-scale XPCS investigations typically use small beam sizes, which result in the accumulation of doses, approaching the MGy in the sample [123]. Synchrotron sources emit an X-ray beam with high intensity, capable of inducing structural and dynamic modifications in the material. Consequently, we implement a new approach for measuring the effect of X-ray dose and dose rate on the structure and dynamics of Ig+PEG and BSA+$YCl_3$ protein gels using XPCS. And this study focuses on the issue of radiation-induced dynamics in an experimental setup. This kind of approach enables the control of radiation impacts and the acquisition of relevant information regarding long-time diffusion dynamics [20].

The structure of the thesis is as follows: in Chapter 1, we provide an overview of phase transitions and interactions in protein solutions, and in Chapter 2, we discuss the theoretical background of the measurement methodologies used. Then the experimental approach is described in Chapter 3. In Chapter 4, methods for handling large XPCS datasets are introduced, along with a detailed explanation of the data processing that led to the key findings discussed in Chapter 5. In Chapter 6, we explain the findings and provide a discussion, conclusions, and outlook for future research.

# Chapter 1

# Phase transitions and interactions in protein solutions

Proteins are naturally biopolymers composed of amino acid monomers kept together by peptide bonds [60]. The properties of proteins are determined by the side chains of amino acids, which vary in charge, size, polarity, and ability to form hydrogen bonds [52, 28]. Understanding phase separation, diffusion in crowded solutions, gelation, glass transition in concentrated protein systems, and dynamics of proteins are thus important [7].
This chapter will present the theoretical framework to describe protein interactions and liquid-liquid phase separation. Some parts of this chapter, especially the spinodal decomposition, phase transition, and glass transition sections, are based on the book (The Physics of Phase Transitions [87]).

## 1.1 Possibilities and restrictions of a colloidal approach for protein solutions

In this section, I will present the status quo of our understanding about the colloidal picture for protein interaction. There is a growing awareness that proteins are large enough to display colloidal behavior in an aqueous solution, similar to other biopolymers [122]. Colloid scientists have studied globular proteins for a long time [7, 122]. Actually, a significant part of the earliest colloid literature concentrated on protein solutions. But it has also been found that proteins are much more complicated than the usual hard-sphere model of colloids. Using theories designed for such particles is clearly inadequate in many circumstances due to the non-spherical nature of proteins and the non-isotropic

nature of their interaction potentials. Colloid science has only recently come back into focus in the protein community [114, 122]. The primary motivation for this was the lack of knowledge about the theoretical foundations of protein crystallization and the requirement to develop more effective methods for crystallizing proteins and obtaining their high-resolution structures using X-ray and neutron-based crystallography. Previous studies linked the capability of proteins to crystallize with broad measurements of their interaction potential, like the second virial coefficient $B_2$. Thus, the results of these findings were subsequently linked to theoretical and computational studies of how interaction potential and the resulting phase behavior are related [114, 85].

Proteins are composed of lengthy chains of small building blocks called amino acids. They have a complex, hierarchical structure. In principle, to get an accurate description of the system, it is important to take into account how each atom of the proteins moves and interacts with the other protein atoms, the solvent atoms, and all the ions in the solution [57]. Since many of these interactions are irrelevant for predicting the phase diagram, this is not the most effective method to approach the problem. The most straightforward approximation to characterize the interactions between proteins is to imagine them as spherical objects with an effective potential between them. This has the advantage of offering a theoretical foundation created for other spherical colloids which have already been investigated. In colloidal science, phase diagram predictions are frequently estimated for colloids that are spherical and rigid [62, 113]. Strong similarities were found between the existing experimental phase diagrams of globular proteins and those of colloids that interact through a composition of hard sphere repulsion as well as a short-range attraction. It was proposed to use a universal phase diagram for globular proteins to identify the optimal circumstances for protein crystallization [114, 28]. The extended law of related states played a crucial role in the development of scientific understanding. This law established the universality of the applicable phase diagram and provided a straightforward connection between the binodal's position and a reduced second virial coefficient ($B_2^* = B_2/B_{2,HS}$) [28]. $B_{2,HS}$ represents the hard sphere second virial coefficient. [114, 28].

Protein interactions depend on parameters like the pH, the strength of ions, and temperature of the solution, and colloid interactions also depend on the mentioned parameters [28]. Although conformational changes in proteins can be caused by pH or other external factors, the overall (tertiary) structure of proteins remains globular. It is also obvious that much more emphasis will need to be paid to the anisotropic and patchy character of protein interactions and their influence on the many structural and dynamic aspects of

protein solutions [114].

One of the most important areas of research in the field of soft matter physics is the study of non-equilibrium phenomena in colloidal suspensions. Experimental and theoretical soft matter researchers have paid a lot of efforts to answer questions such as whether a metastable liquid-liquid binodal exists or not, how spinodal decomposition and glass formation interact, and whether a dynamical arrest or jamming occurs through suspensions of (weakly) short-range attractive colloids or not. When a weak and short-range attraction is applied to hard-sphere particles, it leads to the notable phenomenon of glass melting. This is followed by the formation of re-entrant glass or solids if stronger attractions are present [32, 114]. In the presence of intense particle interactions, a phenomenon known as irreversible aggregation occurs. This regime leads to the formation of soft fractal gels, even at very small volume fractions [48, 114, 61].

Colloids often have electric charges, so they interact with each other through a screened Coulomb repulsion. Indeed, the phase behavior of protein solutions and the occurrence of dynamical arrest with increasing concentration are of essential importance in a wide range of circumstances. Figure 1.1 presents a simplified state diagram for colloids that interact with each other through short-range attractions and long-range repulsions [48, 36]. The red line represents the binodal line, indicating a metastable liquid-liquid phase separation caused by short-range attractive interactions. This process can lead to the formation of new arrested states if it engages with the arrest or gel line [114, 36]. When a short-range attraction is added, new states emerge, the metastable liquid-liquid phase separation is repressed, and (transient) equilibrium clusters form. It is especially interesting that the clusters undergo an arrest transition from a fluid state to a glass state at a significantly lower volume fraction compared to the hard-sphere glass at $\phi = 0.58$ [114, 56, 52].

Since proteins are typically not perfect spheres, shape anisotropy is a very important factor in this context. In recent years, have observed a wide variety of colloid synthesis techniques, which have led to an amazing number of colloids with different shapes, compositions, and functions. These advancements have contributed to our understanding of how anisotropy in shape and interactions affects clustering, self-assembling, and phase behavior in colloidal suspensions. Similarly, progress has been made in computer simulations of anisotropic particles. [114]. However, most of the research has focused on phase behavior and self-assembly, and we still know very little about the dynamics of particles with different shapes or how shape anisotropy affects dynamical arrest. Most of the existing model systems for these particles are very turbid at high concentrations, which makes it hard or impossible to study dynamic properties like the collective or self-diffusion

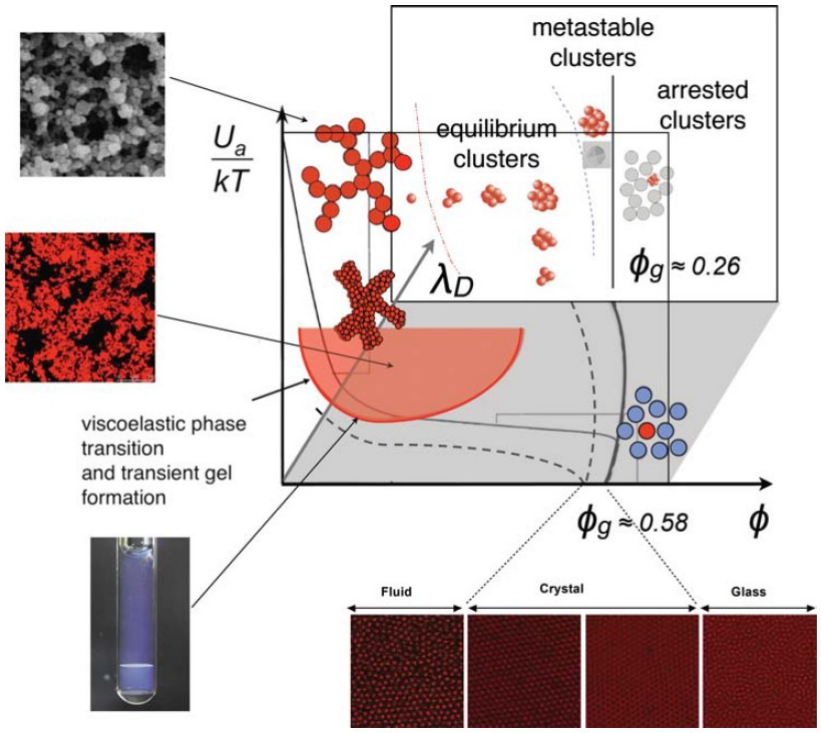


Figure 1.1: Colloidal particles in a schematic state diagram with mixed interaction potentials that include a screened Coulomb repulsion with screening length $\lambda_D$ and a short-range attraction with strength $U_a$. Both the freezing line (dashed line) and the arrest line (solid line) are shown as functions of the volume fraction $\phi$, $U_a$, $\lambda_D$. These cases particularly highlight the metastable liquid-liquid phase separation in short-range attractive particles, pure repulsive systems, and particles with mixed potentials, in which the range of the soft repulsion is considerably larger than the attraction, and where one further finds an equilibrium cluster phase as well as a cluster glass [114, 36].

coefficient or even the particle mean square displacement with standard optical tools. Only recently developed techniques like differential dynamic microscopy and X-ray photon correlation spectroscopy have made it possible to study these properties at high concentrations near the glass transition for such model anisotropic particles [114, 61].

Few studies provide experimental confirmation of the various hypotheses regarding the phase behavior of patchy colloids, and hardly any research has been done on the effects of patchy interaction on the dynamics of such suspensions. The current limitations in using molecular structure-based models for calculating structural and dynamic properties of proteins, and their dependence on solution parameters such as ionic strength, temperature, pH, and proteins concentration, are due to the constraints imposed by classical spherical

particles at centrosymmetric potentials [114, 36]. This is especially important for an extension of a colloid approach to protein solutions beyond these classical spherical particles with centrosymmetric potentials [114, 36].

### 1.1.1 Protein phase behavior

For biological functionality or medication formulation with so-called biopharmaceutics, solution stability of the protein is crucial, and globular proteins are typically well-tuned against non-functional interactions [46, 114]. Although new and exciting evidence suggests that phase transitions in living cells may be an important part of how cells organize themselves, protein phase separation has frequently been linked to so-called protein condensation diseases [21]. The link between liquid–liquid phase separation in solutions of proteins in the eye lens and the development of cataracts, which are still one of the leading causes of blindness across the world. It leads to a systematic study of the phase diagrams of different types of $\gamma$-crystallin. Information on experimental phase diagrams is only available for a small subset of proteins, like lysozyme and $\gamma$-crystallin variations, however it does cover a wide range of solution conditions [114].
The first scientific basis was found in the striking similarities between the known phase diagrams of different globular proteins and George and Wilson's discovery that the second virial coefficient $B_2$ of crystallizable proteins were all obtained in a narrow range of slightly negative values. Another important factor was the extended law of corresponding states, which showed that the reduced second virial coefficient $B_2^*$ can be used as a essential route to measure the strength of the short-range attractive potential. For such potentials, $B_2^*$ largely determines where the binodal and the liquid–solid phase boundaries are for a given protein system. Crystallization is most likely happen in a crystallization window between the liquid–solid phase boundary and the binodal at concentrations below an expected gel line or arrest line above the critical concentration. Muschol and Rosenberger postulated a typical phase diagram for globular proteins, which is depicted in Figure 1.2 [114, 36].
We have been focusing exclusively on globular proteins so far. However other types of proteins have attracted a lot of interest, especially in respect to the development of new biopharmaceuticals. Monoclonal antibodies (mAbs), like immunoglobulin gamma (IgG), are widely considered to be an important platform for future drug prospects. However, stability and low viscosity high concentration formulations are necessary for a successful mAb applications [29, 114]. This is because mAb have a tendency to show reversible self-association at high concentrations, which results in enhanced viscosity, and they are also

known to exhibit strong turbidity due to the presence of liquid-liquid phase separation [29].

The binodals found in mAbs are very different from those found in globular proteins. Their critical concentrations ($C_c$) and temperatures ($T_c$) are usually lower than those of globular proteins, and their binodal and spinodal regions are wider, like those of low-valency patchy particles. This indicates that this protein is not perfectly described by the colloidal approximation. The phase diagram becomes symmetric again when polyclonal antibodies and polyethylene glycol (PEG) are used, most likely because the depletion interaction generated by the polymers is more powerful than the protein-protein interaction. So, determining whether or not the colloidal approximation is valid requires careful consideration of each individual circumstance [114, 111, 78].

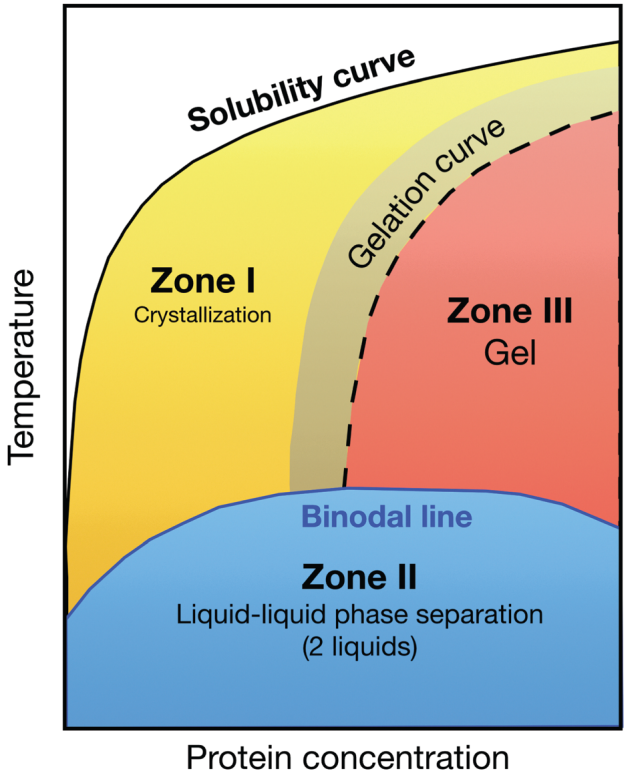


Figure 1.2: A typical example of a protein system's phase diagram,postulated by Muschol and Rosenberger. The samples in the blue region phase separate into a dense phase and a dilute phase after falling below the binodal line. When it comes to crystallization, the samples below the solubility line are metastable. The yellow-shaded area in zone I is the optimum place for protein crystallization, while zone III tends to gel [114, 56].

### 1.1.2 Protein interactions

In order to achieve a comprehensive understanding of the system, it is essential to take into account the dynamic behavior and intermolecular interactions of individual protein atoms, as well as their collective interactions with other protein atoms and the surrounding ions within the solution. Intermolecular interaction potentials on a length scale of Å to a few nm can control the crystal growth properties and liquid-liquid phase behavior of biological macromolecules. The pairing potential of two particles has been described in terms of effective interactions. The effective protein pair interaction potential, $V(r)$, for protein systems such as lysozyme molecules in solution, with centers separated by a distance $r$ is modeled within the Derjaguin-Landau-Verwey-Overbeek (DLVO) theory as the combination of a repulsive hard-sphere potential, $V_{HS}(r)$, a long-ranged screened Coulomb potential, $V_{SC}(r)$, and a short-ranged attractive Yukawian–like potential, $V_Y(r)$ [61, 93]. The interparticle interaction potential $V(r)$ for protein solutions is given as:

$$V(r) = V_{HS}(r) + V_{SC}(r) + V_Y(r) + V_{depl}(r) + V_a(r). \tag{1.1}$$

$V_{HS}(r)$ is the excluded-volume repulsive hard-sphere potential, which can be given as:

$$V_{HS}(r) = \begin{cases} \infty & , r \leq \sigma \\ 0 & , r > \sigma \end{cases}. \tag{1.2}$$

Where $\sigma$ describes the protein's effective hard-sphere diameter. The repulsive hard-sphere potential expresses that the particles can not occupy the same space due to their impenetrability. The long-range screened Coulomb potential, $V_{SC}(r)$, is given by

$$V_{SC}(r) = \begin{cases} 0 & , r \leq \sigma \\ \dfrac{Z^2 e^2 \, \exp -(r-\sigma)/\lambda_D}{4\pi\epsilon_0 \, \epsilon_r (1 + 0.5\,\sigma/\lambda_D)^2 \, r} & , r > \sigma \end{cases}. \tag{1.3}$$

The effective net charge of the protein is fixed at a constant value called $Z$ ($Z = +8e$ for Lysozyme at pH 7), which is almost true for all of the different conditions of the solutions [61, 93]. The Debye-Hückel screening length, $\lambda_D$, tells us how far the interaction extends and depends on the ionic strength of the solution and is defined as:

$$\lambda_D = \sqrt{\frac{\epsilon_0 \, \epsilon_r \, k_B \, T}{2 N_A \, e^2 \, I}},$$

where $I$ is the ionic strength, $N_A$ is the Avogadro´s number, $\epsilon_0$ is the dielectric permittivity of the vacuum, $k_B$ is the Boltzmann constant, $\epsilon_r$ is the pressure dependent solvent's static dielectric permittivity, and $T$ is the temperature of the solution [61, 122].
The Asakura and Osawa theory describes depletion forces, which are the forces caused by entropic effects, present in solutions of colloids and non-absorbing polymers. This is the type of interaction that is most relevant to the study in this thesis. Polymer-protein mixtures have been studied a lot because adding polymers to solutions of proteins leads to both phase separation and crystallization. Due to this concept, it is simple to find colloidal approaches to understanding the phase diagrams of these protein systems [122, 126].
The Asakura-Oosawa model predicts that favorable depletion protein interactions arise from an osmotic pressure when non-adsorbing polymers, such as polyethylene glycol (PEG), are added to the solution. In the presence of polymers, the depletion potential is defined by:

$$V_{depl}(r) = \begin{cases} \infty & r \leqslant \sigma \\ \Pi_p \, V_{overlap} & \sigma < r \leqslant \sigma + 2r_g \\ 0 & r < \sigma + 2r_g \end{cases} . \tag{1.4}$$

With the osmotic pressure of the polymer $\Pi_p$, the radius of gyration of the polymer $r_g$, and the volume of the overlapping depletion areas between two particles at an inter-center distance of $r$ is $V_{overlap}$. The square-well potential $V_a(r)$ describes how the proteins stick together on their own, which is resulted by strong short-range interactions like hydrogen bonds, hydrophobic bonds, and ionic bonds [61, 126, 93].

$$V_a(r) = \begin{cases} \epsilon_{AB} & , r_{AB} < r_c \\ 0 & , r_{AB} > r_c \end{cases} \tag{1.5}$$

where $r_{AB}$ is the distance between bonding sites A and B, $\epsilon_{AB}$ is the bonding potential, and $r_c$ is the cut-off distance of the bonding sites. The osmotic-attraction potential and the attractive van-der-Waals dispersion forces can be modeled in the form of a Yukawa potential.

$$V_Y(r) = \begin{cases} 0 & , r \leq \sigma \\ -J\sigma \, \dfrac{\exp -(r-\sigma)/d}{r} & , r > \sigma \end{cases} \tag{1.6}$$

where $J$ is the depth of the interaction potential at $r = \sigma$, and $d$ is the range of the attractive potential.

The mean intermolecular space of the protein molecules decreases significantly with increasing crowder concentration, and this effect is most pronounced for small-sized PEG molecules. Strong repulsive forces, such as soft enthalpic protein-PEG interactions and/or hydration-shell repulsion, must exist at small distances in order to stabilize the protein against depletion-induced aggregation [61, 126].

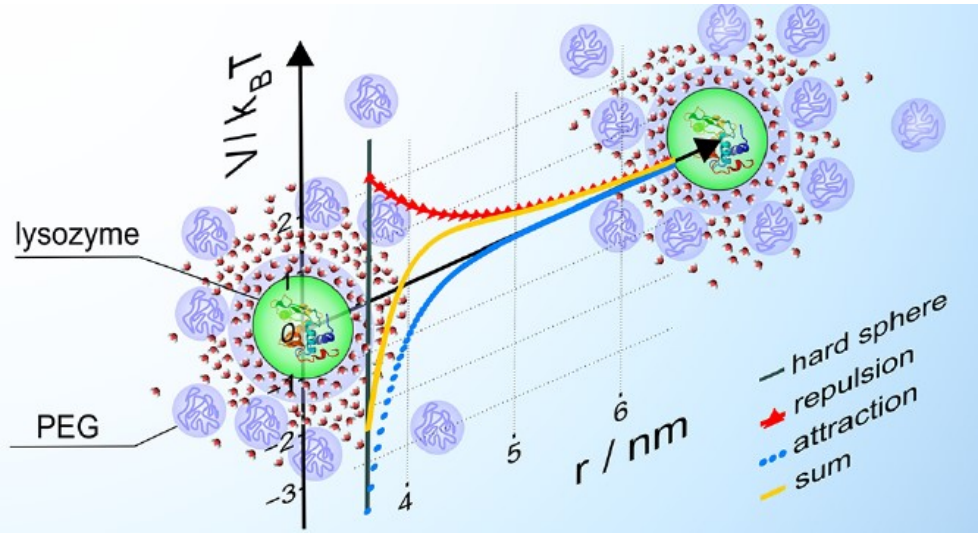


Figure 1.3: The Derjaguin Landau Verwey Overbeek potential and its contributions of two lysozyme proteins in solution. Small-size PEG molecules have the strongest effect, and as the concentration of crowders goes up, the average distance between protein molecules gets much closer [61].

## 1.2 Phase transition and spinodal decompostion

The phase separation of a binary mixture $AB$ may take place when a material finds itself in the thermodynamically unstable region of the phase diagram. The $AB$ mixture liquid crystallizes by nucleation mechanism followed by growth of nuclei when quenching occurs due to the temperature changes. Gibbs was the first to report this behavior by proposing a clear distinction between the regions of metastable and unstable equilibrium. Outside of the spinodal the physical system becomes unstable [87, 56].

When the liquid is quenched from temperature $T_i$ to point (a), which is located between the coexistence line and the spinodal, the liquid crystallizes by a nucleation process followed by the growth of nuclei (microcrystallites). However, if the quenching process is terminated at point (b) far beyond the spinodal, the unstable liquid phase separate

through a mechanism known as spinodal decomposition. Its transition to a stable state is caused by the spontaneous fluctuations in concentration. This kind of situation presented in Figure 1.4 for a binary mixture [87, 11, 56].

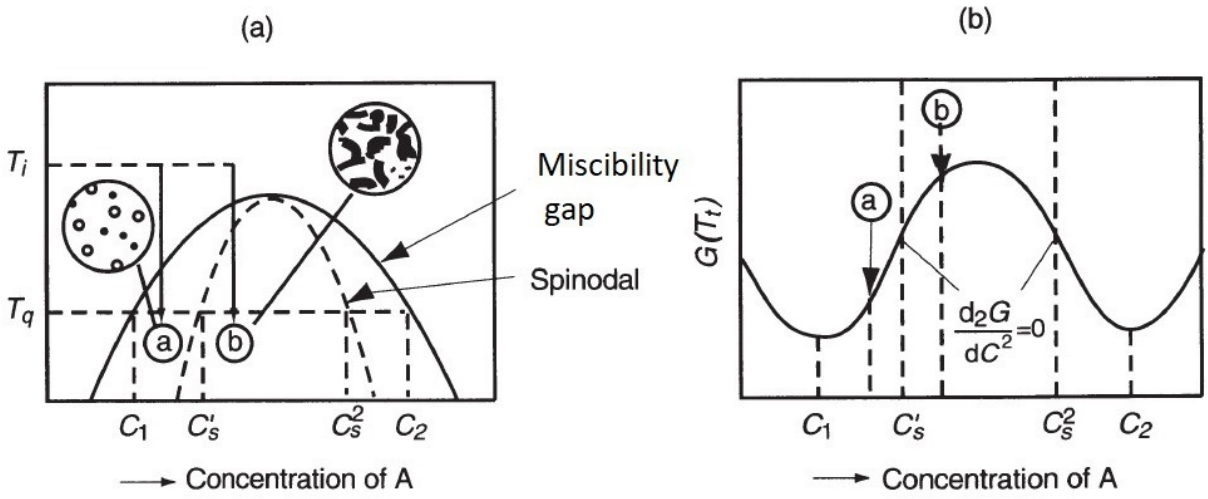


Figure 1.4: Phase diagram of a separation process (a) when the system is quenched from temperature $T_i$, local concentration fluctuations within the spinodal at point b cause a phase transition in the system, which is known as spinodal decomposition. (b) Diagram of free energy at quenching temperature $T_i$ [87].

### 1.2.1 Thermodynamics of spinodal decomposition and Cahn-Hilliard equation

Our focus here is on the termodynamics of spinodal decomposition, which can be modeled mathematically using a liquid-binary system A-B. The concentration of substance $A$ in the binary mixture is given as:

$$c = X_A/(X_A + X_B),$$

where $X_A$ and $X_B$ are mole fractions of A and B components in the binary mixture and $X_A + X_B = 1$. We will assume that the mixture is still homogenous even though we have passed the spinodal and are entering the thermodynamic instability area. The inhomogeneity in the mixture arises from local, random fluctuations in the concentration c, which then becomes a local function $c(r)$ [87].

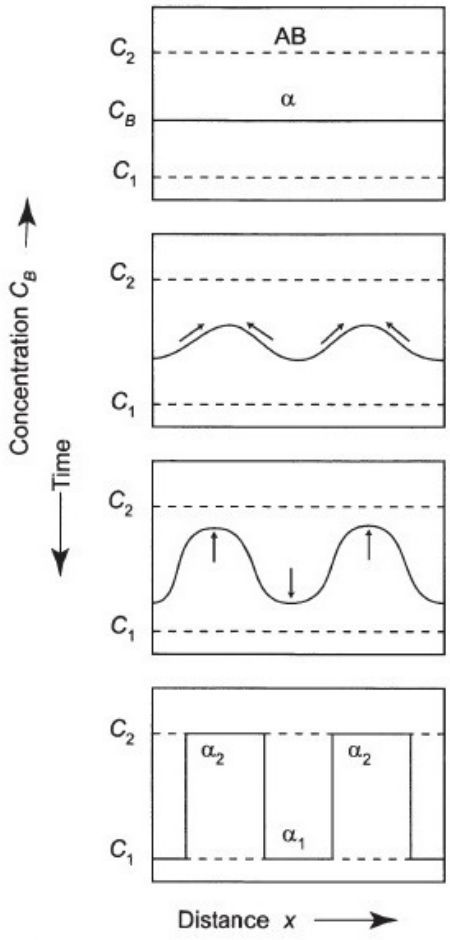


Figure 1.5: Spinodal decomposition. The local changes in the concentration $c$ of constituent $A$ in binary mixture $AB$. The spontaneous fluctuation in concentration produce two different phases $\alpha_1$ and $\alpha_2$ within the initial homogeneous binary mixture $\alpha$. The concentration fluctuation increasing in the mixture by spinodal decomposition [87].

In this case, there are significant concentration discontinuities that are related to the appearance of the new phase's nucleus at the outset of the transition. When spinodal decomposition occurs, concentration fluctuations are essentially homogeneous, whereas when the transition occurs via nucleation, they are essentially heterogeneous [54, 87].
In a binary system AB, the average concentration can be defined as $c_0$. The free energy per unit of volume $f(c)$ around $c_0$ can be written as a series:

$$f(c) = f(c_0) + (c - c_0)\left(\frac{\partial f}{\partial c}\right)_{c_0} + \frac{1}{2}(c - c_0)^2\left(\frac{\partial^2 f}{\partial c^2}\right)_{c_0} + ... \tag{1.7}$$

We assume that the amplitude of the fluctuations is relatively low, which is clearly an approximation. The system's total free energy $F$ will then be expressed as:

$$F = \int \left[ f(c) + \frac{1}{2} K |\nabla c|^2 \right] dV. \tag{1.8}$$

The term $K|\nabla c|^2$ for $K > 0$ is an energetic term that depends on the concentration gradient in the system, and in some ways, it is similar to the interfacial energy for fluctuations. The free energy for the formation of a new phase corresponds to the difference in free energy between the homogeneous and inhomogeneous parts of the material and can be written as:

$$\Delta F = \int \left[ \frac{1}{2} (c - c_0)^2 \left( \frac{\partial^2 f}{\partial c^2} \right)_{c_0} + \frac{1}{2} K |\nabla c|^2 \right] dV. \tag{1.9}$$

In Equation 1.7 eliminated the first-order terms because of the average concentration definition $\int (c - c_0) dV = 0$. In the expansion, terms beyond the second order were neglected. According to the Equation 1.9 if this condition $(\partial^2 f / \partial c^2) > 0$ and $\Delta F > 0$ are fulfilled the homogeneous solution will remain stable and the concentration fluctuation will tend to decrease.

The concentration fluctuation is assumed to be both a local variable and a function of time. The Fourier transformation can be used to describe it as:

$$\delta c(k, t) = \int \delta c(r, t)\, e^{ikr} dr. \tag{1.10}$$

To make the explanation more simple, let's assume that we are working with a one-dimensional material where fluctuations have the same amplitude A, and take the form $\delta c_k = A\, cos(kx)$. Using the following relation $\Delta F = \int \Delta F_k dk$ and taking the integral from Equation 1.9 in the total volume of the material and the difference in free energy of the system $\Delta F_k$ can be written as:

$$\Delta F_k = \frac{1}{4} V A^2 \left[ \left( \frac{\partial^2 f}{\partial c^2} \right)_{c_0} + K k^2 \right]. \tag{1.11}$$

One can see immediately in Equation 1.11 that the short wavelength (large $k$) fluctuations will tend to raise the free energy and stabilize the homogenous mixture if it is in a zone of thermodynamic instability $(\partial^2 f / \partial c^2) < 0$. Large wavelength fluctuations (low $k$) cause a decrease in the free energy $\Delta F_k < 0$, which stabilizes the inhomogeneous system and tend

to the phase transition corresponding to spinodal decomposition. The critical wave-vector $k_c$ can be written as:

$$\left(\frac{\partial^2 f}{\partial c^2}\right)_{c_0} + Kk^2 < 0$$

with

$$k_c = \sqrt{-\frac{1}{K}\left(\frac{\partial^2 f}{\partial c^2}\right)_{c_0}}. \tag{1.12}$$

It follows that:

• for $k > k_c$ the homogeneous solution is stable

• for $k < k_c$ the inhomogeneous solution is stable and there is spinodal decompositton.

Spinodal decomposition will occur if $\lambda > \lambda_c$, where $\lambda_c = 2\pi/k_c$.

Using a diffusion equation, one can determine the kinetics of the transformation of a binary mixture. J. W. Cahn calculated this equation. The concentration current J in the binary mixture is created by the potential gradient, which is also called the "thermodynamic force," and linked to the chemical potential ($\mu = \partial F/\partial c$) through the following equation:

$$J = -M_0 \nabla \mu, \tag{1.13}$$

where $M_0$ is the mobility coefficient in the solution. The concentration currents for the binary mixture $J_A$ and $J_B$ are given as:

$$J_A = -J_B = M_0 \nabla(\mu_A - \mu_B). \tag{1.14}$$

In the absence of a chemical potential reaction, the diffusion equation can be defined as:

$$\frac{\partial c(r,t)}{\partial t} + \nabla J = 0. \tag{1.15}$$

Here $c(r,t)$ is a variable that describes the inhomogeneous material. If the number of atoms $A$ and $B$ in the mixture is $n_A$ and $n_B$, respectively with $N = n_A + n_B$, we can write:

$$\mu_A - \mu_B = \frac{1}{n_A + n_B}\frac{\partial F}{\partial c} \tag{1.16}$$

and thus:

$$\frac{\partial c(r,t)}{\partial t} = \frac{M_0}{N}\nabla^2\left(\frac{\partial F}{\partial c}\right) = M\nabla^2\left(\frac{\partial F}{\partial c}\right). \tag{1.17}$$

We can take the functional derivative of free energy $F$ with respect to $c$

$$\delta F = \int \left[ \frac{\partial f}{\partial c} \delta c + \frac{1}{2} K \nabla_r \, \delta c \, \nabla_r c + \frac{1}{2} K \nabla_r \, c \nabla_r \, \delta c \right] dr. \tag{1.18}$$

Integration from Equation 1.18 and assuming that $\nabla_r c = 0$ gives the following equation:

$$\delta F = \int \left[ \frac{\partial f}{\partial c} - K \nabla^2 c \right] \delta c dr \tag{1.19}$$

and thus:

$$\frac{\partial F}{\partial c} = \frac{\partial f}{\partial c} - K \nabla^2 c. \tag{1.20}$$

Therefore:

$$\frac{\partial \delta c(r,t)}{\partial t} = M \nabla^2 \left[ \frac{\partial f}{\partial c} - K \nabla^2 c(r,t) \right] \tag{1.21}$$

This is called the Cahn-Hilliard equation, which expresses the time-dependent evaluation of the concentration, and it is a non-linear diffusion equation [15].
As we are interested in relatively low amplitude concentration fluctuation a linearized diffusion equation can be defined as:

$$\frac{\partial \delta c(r,t)}{\partial t} = M \nabla^2 \left[ \left( \frac{\partial^2 f}{\partial c^2} \right)_{c_0} - K \nabla^2 \right] \delta c(r,t). \tag{1.22}$$

Assuming that fluctuations have an exponential relaxation mechanism, the Equation 1.22 can be solved by using the Fourier transform of Equation 1.10 as:

$$\delta c(k,t) = \delta c(k,0) \exp(-\omega_k t). \tag{1.23}$$

Where $\omega_k$ is relaxation coefficient and by substituting Equation 1.10, and Equation 1.23 into Equation 1.22, we immediately identify:

$$\omega_k = M k^2 \left[ \left( \frac{\partial^2 f}{\partial c^2} \right)_{c_0} + K k^2 \right] \tag{1.24}$$

By introducing the wave vector $k_c$, $\omega_k$ is rewritten as:

$$\omega_k = M K k^2 \left[ k^2 - k_c^2 \right]. \tag{1.25}$$

In Equation 1.25, the following two components combine to form the damping coefficient

$\omega_k$ :

• The first part $Mk^2$ is outcome from diffusion in the solution.

• The second part $K(k^2 - k_c^2)$ expresses the inhomogeneities in the concentration and assists spinodal decomposition for small wave vectors.

In the thermodynamically unstable region for $k < k_c$, $\omega_k < 0$, the concentration fluctuations are no longer damped and increase with time. This is called spinodal decomposition [87, 13].

## 1.3 Introduction to the Glass transition

Most solid mineral compositions and elements melt when heated to high temperatures and turn into liquids with low viscosities (a few centipoises), and when the temperature is lowered, the liquids solidify back into crystalline solids [8]. Alternatively, there are also some materials that, when melted, transform into liquids that have a very high viscosity ($10^5 - 10^7\, cP$ ). When these liquids are cooled below their melting points, they don't solidify immediately. Instead, they stay in a state called supercooled [129], in which the viscosity of the liquid significantly increases when the temperature is reduced, and it freezes into a noncrystalline solid called glass. The glass's viscosity can reach $10^{12}$–$10^{13}\, cP$ [87].

Glasses are made by rapidly chilling or pressurizing a liquid, which causes molecular motion to slow down. When these operations are done at a constant rate, the required time for the structure to relax will eventually be longer than the time we give it to get back to equilibration. Because of this, the system is no longer in equilibrium, and this process is known as the glass transition [85, 87].

The vibrational energy in glass, which has a uniform temperature, is equilibrated, and local redistribution of temperature is ensured by thermal conduction. Thus, we can conclude that glass is partly in a state of metastable thermodynamic equilibrium. An entropy can be defined for glass even if it is not equivalent to the entropy of a liquid at the same conditions (p, v, T). To determine the entropy of glass, one must integrate the specific heat at a constant pressure and then compare the resulting value to the entropy of a crystal at the same temperature. As expected, glass doesn't have the lowest entropy. Instead, it has more entropy $\Delta S$ than the crystalline state, however this gap between the two entropies gets smaller as the temperature drops down [85, 87]

$$\Delta S = S_{\text{liq. or glass}} - S_{\text{cryst}}$$

and then

$$\Delta S = \frac{L_f}{T_m} - \int_T^{T_m} (C_{pl} - C_{ps}) \frac{dT}{T}. \tag{1.26}$$

The specific heats of the solid and liquid are, respectively, $C_{ps}$ and $C_{pl}$ and $L_f$ is the latent heat of fusion of a solid at the melting point $T_m$.

The glass transition can be described by looking at how several thermodynamic quantities change. When a liquid is cooled at a constant pressure, its volume goes down, and this decrease continues into the supercooled state except if crystallization is induced. Either the supercooled liquid will crystallize on its own or the rate of volume reduction will suddenly change at temperature $T_m$. Then the slope of the $V(T)$ curve will abruptly change Figure 1.6 [85, 7]. The glass transition temperature $T_g$ value also depends on how fast the liquid is cooled [72]. High quenching rates speed up the glass transition, whereas low quenching rates allow for a straight transition to the crystalline state without the creation of glass according to the laws of thermodynamics. Unlike the sudden changes seen during crystallization and melting, the glass transition is clearly gradual. There is no contribution of any latent heat [87, 66, 85].

## 1.4 Arrested state liguid-liquid phase separation

Phase separation and phase transition are the most fundamental phenomena that have been studied in most non-living and living materials. These studies show that phase transition plays a key role in living cells [120, 109, 133]. One of the most important phenomena of phase transition is phase separation, such as liquid-liquid phase separation inside of cells, which causes the formation of dense protein droplets, RNA, and other biomolecules. Phase separation in a solution can start from a molecular length scale and then the characteristic size of the phase-separated domains will increases to the macroscopic scale. The medical and food industries both benefit from a deeper knowledge of arrested LLPS in protein systems [109, 120, 11].

There are two phase transition boundaries in a typical phase diagram of a protein solution: the solubility line (also called the liquidus line) for crystallization and the coexistence curve for LLPS. Although there have been many direct observations of LLPS in solutions of globular proteins. It is possible that the conclusions about the features of the phase diagram of compressed globular proteins do not really apply to Y-shaped IgGs. In fact,

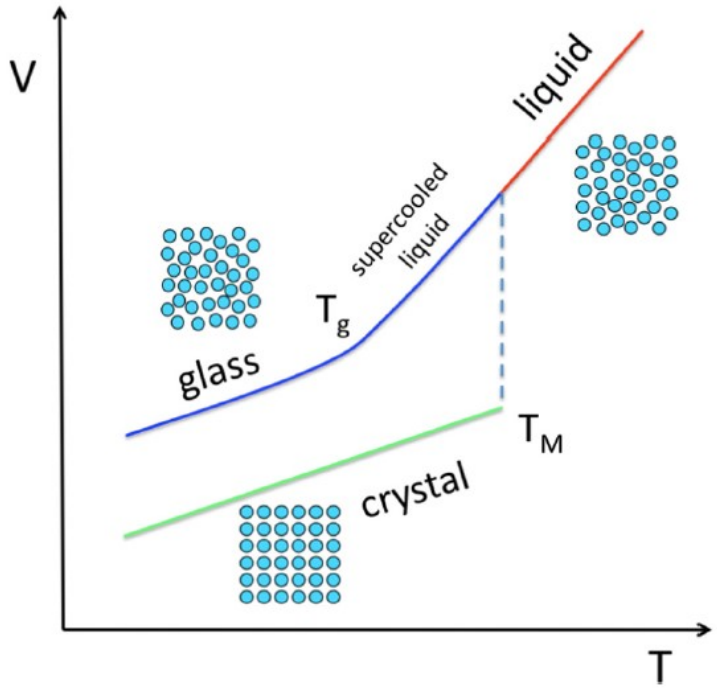


Figure 1.6: Glass transition, change in the volume $V$ as a function of the temperature $T$ in the liquid, glassy and crystalline states. The relationship between temperature and volume for an imaginary system in the liquid phase (red line), the crystalline solid phase (green line), and the supercooled regime (blue line). Melting ($T_m$) and glass transition temperatures ($T_g$) are indicated by labels. [87, 85].

the critical concentration for IgGs is much lower than that for quasi-spherical proteins [24, 126].

The polyvalent antibody mixture of bovine $\gamma$-globulin has effective interactions driven by short-ranged attractive interactions. This thesis studied a bovine IgG in vitro phase transition in the presence of polyethylene glycol (PEG). PEG induces a definite attraction between proteins in solution through so-called depletion forces. The depletion forces are caused by the steric restriction of PEG from the contact region between the protein molecules [78]. Therefore, with very few exceptions, PEG binding to proteins does not modify the existing inter-protein interaction. When the concentration of PEG is high enough, it raises the phase separation temperatures above the freezing point of the solution, indicating that PEG-induced attraction raises the temperature at which LLPS occurs. The coexistence curve of a pure IgG solution, which occurs at temperatures below the freezing point of the solution, can be obtained by measuring the phase boundaries at various PEG concentrations and then extrapolating to zero PEG concentration [24, 126,

58].

Figure 1.7a displays a phase diagram that summarizes the findings of numerical investigations of a spherical attractive short-range potential. There is no dynamic arrest above the spinodal, however, the dynamic arrest is observed in the spinodal region for quenches below $T_g$.

At the moment, the continuation of the glass line into the spinodal region is an open question. A study on lysozyme provides support for the scenario depicted in the figure, in which density fluctuations freeze before reaching their final spinodal value. Figure 1.7b depicts a binodal of the LLPS in the plane of $\gamma$-globulin concentration and temperature. In this model system, the LLPS with an upper critical solution temperature is demonstrated, as indicated by the green arrow depicting the usual quenching process of the dense phase. Dense gel-like phases are observed at low temperatures, indicating the presence of long-lived non-equilibrium states close to the glass line, which may have an impact on the binodal shape. In the phase diagram, the dynamics of the sample are arrested when there are deep quenches. The values of the protein volume fraction ($\phi$) are also shown on the top axis of Figure 1.7b. The highest volume fraction for the high concentration branch of LLPS binodal is about $\phi = 0.22$, which is much lower than that for globular proteins such as lysozyme and $\gamma_B$-crystallin, which is about $\phi = 0.35$. The Y-shape of these protein molecules may be the cause of this variation [120, 134, 24].

Small-angle scattering is a frequent experimental technique used to examine the kinetics of arrested phase separation. It is possible to observe the evolution of the domain size with this scattering technique, by monitoring the domain-domain correlation peak, also known as the spinodal peak. During phase separation, the growth of protein domains is related to an increase of the peak in the structure factor S(q). In addition, the peak position $q_{max}$ is shifting toward smaller scattering vectors, which is associated with an increase in the characteristic length ($\xi = 2\pi/q_{max}$) of protein droplets [120, 24].

After an initial slowdown, the power law of $\xi \approx t^{1/3}$ for diffusive growth describes the data reasonably well. Figure 1.8 shows how the value of $\xi$ changes over time for different concentrations of protein and PEG (samples I–IV), and also for increasing quench depths. Sample I (Figure 1.8a), which has the lowest total protein concentration, exhibits only a slight slowing of growth in the temperature range examined, and a complete arrested state is not reached. For samples with a higher PEG concentration (II and III) or a higher protein concentration (IV), a considerable kinetic slowdown and arrest is observed (Figure 1.8c and d). Coarsening is observed for quenches at intermediate temperatures, which is unexpected. At the first, the growth kinetics follow the 1/3 power law, and then there is a

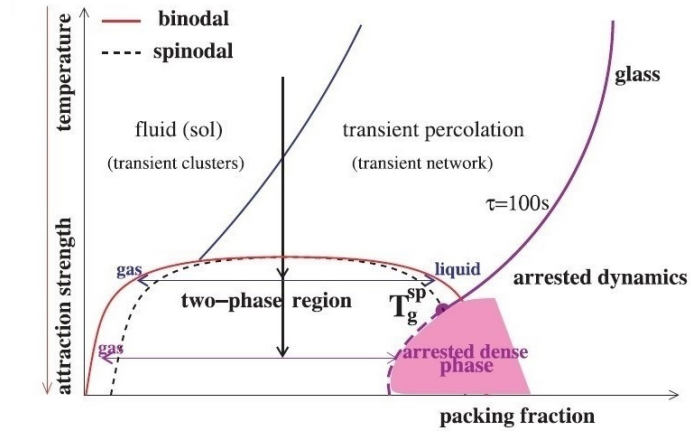


(a)

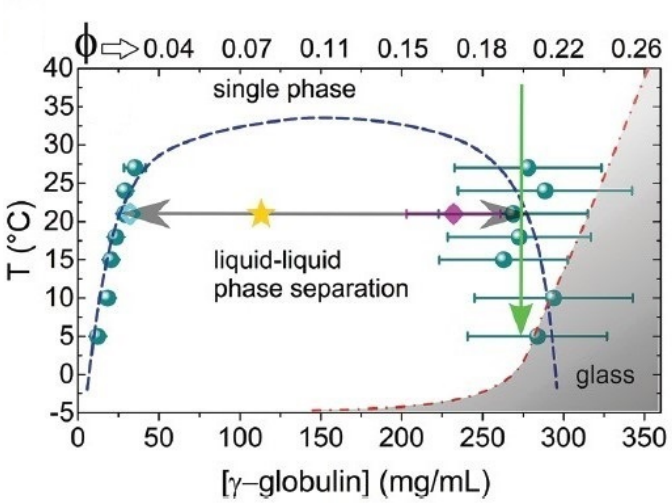


(b)

Figure 1.7: Schematic illustration of arrested state, phase separation, and glass transition. (a) A quench in the two-phase region may cause the denser phase to arrest. The continuation of the glass line into the spinodal region is a question at the moment. (b) LLPS binodal for a parent solution containing 110 mg/ml $\gamma$-globulin and 10% (w/w) PEG. Both the dashed and dash-dotted lines are eye guides for the LLPS binodal and also the glass line, respectively. [134, 24].

clearly visible slowdown. The length of this slowdown is dependent on the sample and the temperature of the quench. Therefore, we can conclude that the concentrations of protein and PEG can be adjusted to produce either a temporary or permanent gel [58, 24, 126].

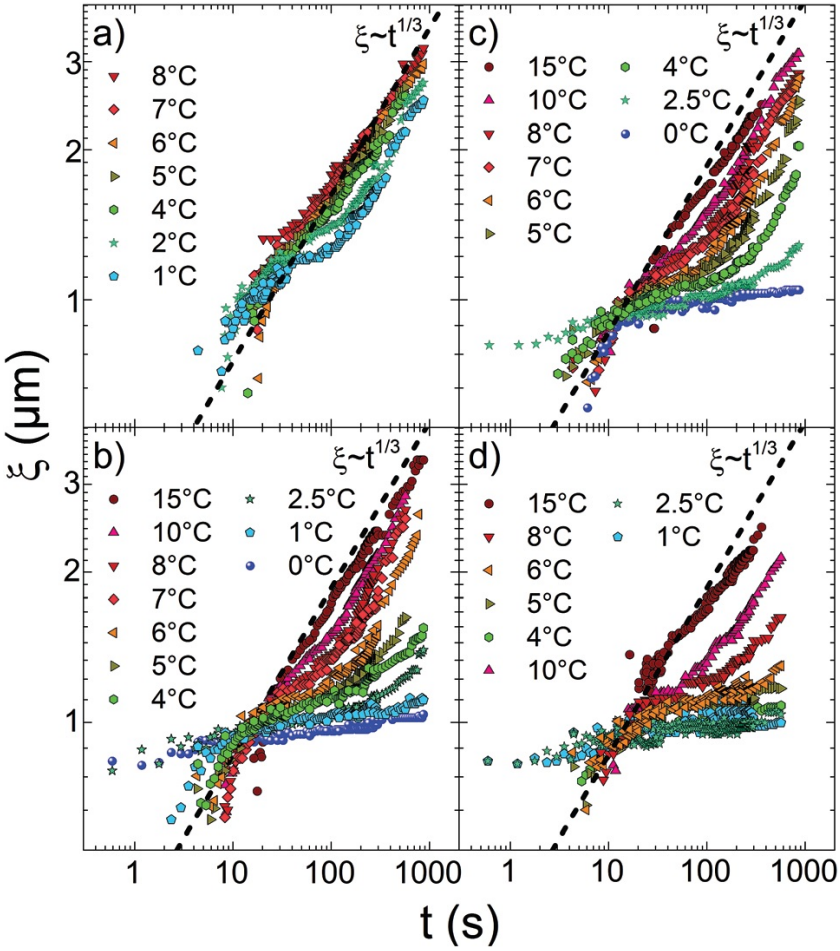


Figure 1.8: The power law or characteristic length represented with the dashed lines as a function of time for different samples, and for increasing quench depths. a) Sample I (220 ± 30 mg/ml Ig and 3.8± 1.2 % PEG) Shows only a minor slowdown and not fully arrested. b) Sample II (230 ± 30 mg/ml Ig and 4.3 ± 0.9 % PEG) With the higher PEG and protein concentration, significantly arrested kinetics can be observed. c) Sample III (246 ± 20 mg/ml Ig and 4.4 ± 1.2 % PEG) Same as Sample II. d) Sample IV (295 ± 30 mg/ml Ig and 2.7 ± 1.1 % PEG) With higher protein and low PEG concentration, an arrested state is observed [134, 24].

## 1.5 Immunoglobulin G (IgG) System

Antibodies, and in particular IgG antibodies, are an extremely valuable class of proteins because of the important role they play in human immunity. They are a type of protein that is very important to the body and is found in the blood plasma. Albumin, which is important for molecular transport in the body, is the most common mammalian plasma protein, followed by immunoglobulins, which are classified as $\alpha_1$-globulin, $\alpha_2$-globulin, $\beta$-globulin, and $\gamma$-globulin (IgG). In addition to their widespread use in labeling target epitopes for research and diagnostics, they are also increasingly being employed as medications for the treatment of a wide range of diseases, such as autoimmune disorders and cancers. All IgGs are derived from the same genetic stock and have the same shape and size, as presented in Figure 1. 9 [126, 24].

IgG is a complex, folded Y-shaped protein that consists of two heavy chains (red and yellow) and two light chains (blue and purple). Each heavy chain and each light chain have one crystallizable domain (Fc) and two antigen-binding domains (Fab), which are linked in the center of the molecule by disulfide bridges. The reported radius of gyration for an IgG monomer is 4.9–6 nm, and its molecular mass is 140–170 kDa. The maximum intermolecular distance is around 18.4 nm, and the specific amino acid sequences in Fab define the biological functions of IgG. However, researchers are aware of the fact that certain amino acid sequences of Fab can create a considerable increase in the total net attractive interprotein interaction among IgG molecules. Many forms of protein condensation, such as liquid-liquid phase separation (LLPS), crystallization, gelation, and reversible aggregation, are triggered by the net attractive interprotein interaction [73]. Since it is a plasma protein, a typical IgG is quite water-soluble under normal circumstances. However, solubility is not always maintained [126, 109].

Protein condensation in solution can be caused by non-specific attractive interactions among IgG molecules at high enough concentrations. In vivo, IgGs can be found in quite high concentrations, and the average total IgG blood level is between 10 and 25 mg/ml. In the rare case of multiple myeloma, the amount of monoclonal IgG can be higher than 70 mg/ml. When a high antibody dose is required for therapeutic purposes, pharmaceutical applications frequently make use of concentrated IgG solutions [126].

Crystallization, liquid-liquid phase separation (LLPS), colloidal aggregation, and gelation are all examples of the condensation of intact protein molecules that occurs in highly concentrated IgG solutions. A phase diagram perfectly describes the range of circumstances necessary for this type of protein condensation to occur. So, understanding the pathogenic

condensation of antibodies in the body and the colloidal stability of antibody medication formulations requires systematic studies of the phase behavior as well as phase diagrams of IgG solutions [126, 24].

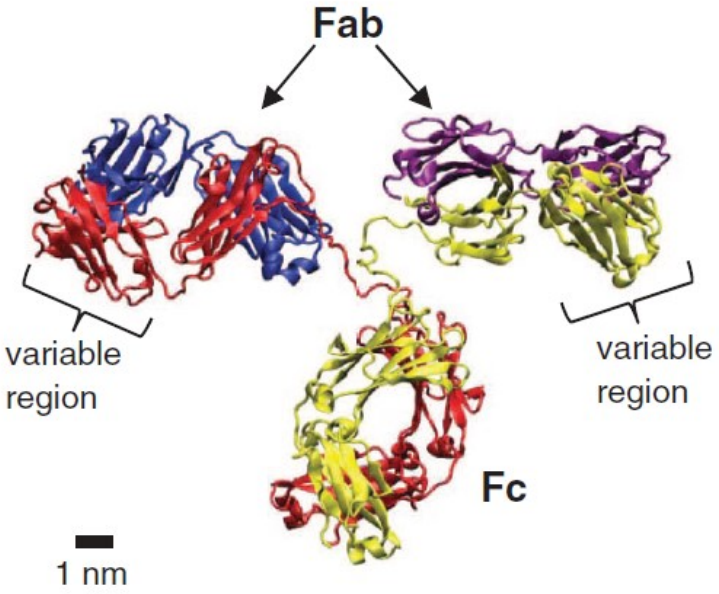


Figure 1.9: An IgG molecule's atomic structure was determined via X-ray crystallography. Two heavy chains (red and yellow) and two light chains (blue and purple) are shown here. Each heavy chain and each light chain consist of one crystallizable domain (Fc) and two antigen-binding domains (Fab) [126, 24].

# Chapter 2

# Theoretical concepts and x-ray scattering methods

Wilhelm Conrad Röntgen observed in 1895 that rapid electrons striking metals create extremely invasive radiation of an unidentified type. He named this interesting radiation X-rays. The electromagnetic radiation known as X-rays has wavelengths that range from around 0.1 to about 100Å, as is now widely accepted [5].
This chapter gives an overview to X-ray scattering concepts as well as a description of the experimental techniques employed for this thesis. The following sections provide an overview of coherent X-ray scattering and X-ray photon correlation spectroscopy (XPCS), which is a highly effective technique for studying the dynamics of a sample. Elements of Modern X-Ray Physics, by Jens Als-Nielsen [5], is the main source for this chapter.

## 2.1 Elastic X-ray scattering

X-rays scatter when they interact with a substance's electron density. Imagine a planar monochromatic X-ray wave impacting on a material with a spatially inhomogeneous electron density (such as colloidal particles dispersed in a fluid) [5, 104]. The electric field of the wave at point $r$ and time $t$ (ignoring the magnetic field for simplicity) is given by

$$E(r,t) = \epsilon\, E_0 \exp\Big(i(k_{in}r - \omega_{in}t)\Big). \tag{2.1}$$

Where $\epsilon$ is the unit vector for polarization, $E_0$ is the electric field's amplitude, and $\omega_{in}$ is its frequency. The wave vector is $k_{in}$, and its amplitude is inversely related to the

incoming wave's wavelength $\lambda$

$$k = \frac{2\,\pi}{\lambda}\,. \tag{2.2}$$

When an X-ray wave passes through a sample, electrons in the region of light begin vibrating at the same frequency as the incident radiation, creating secondary waves, as described by the classical theory of X-ray scattering. The phase shifts of these waves are different, but their frequencies remain the same (this is called "elastic scattering"), so waves can interfere with each other. Figure 2.1 shows a typical scattering scheme [5]. Consider a dispersed wave that propagates in the direction defined by the scattering wave

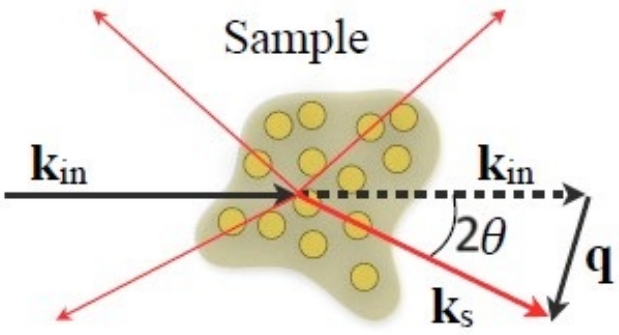


Figure 2.1: The geometry of scattering is depicted schematically. The sample scatters the incoming X-ray radiation, which has a wave vector of $k_{in}$, in many different directions. The wave vector transfer $q$ characterizes scattered radiation measured at an angle $\theta$ with respect to the incident wave [108].

vector $k_s$. Then, we can define $q$, the wave vector transfer, as

$$q = k_s - k_{in}. \tag{2.3}$$

In the case of elastic scattering, the moduli of the wave vectors that are scattered and incident are equal

$$|k_{in}| = |k_s|, \tag{2.4}$$

and the scattering vector's magnitude, q, is given by

$$q = \frac{4\pi}{\lambda}\, sin\left(\frac{2\theta}{2}\right). \tag{2.5}$$

Where the angle formed by wave vectors $k_{in}$ and $k_s$ is the scattering angle $2\theta$ [5, 103].

### 2.1.1 Scattering intensity

In the case of elastic scattering only, the scattered intensity is proportional to the absolute square of the scattered amplitude, and the total wave amplitude is simply the sum of all scattered amplitudes [5]

$$I(q) = \sum |A(q)|^2 .$$

Consider the most fundamental process of X-ray scattering on a single free electron, which is given by the well-known Thomson formula [40]

$$I = I_0 \, r_e^2 \frac{P}{L^2} \tag{2.6}$$

where $r_e$ is the classical electron radius ( $r_e = 2.82 \times 10^{-5}$Å), $L$ is the distance to the point of observation and $I_0 = |E_0|^2$ is the intensity of the incident beam. The polarization factor $P$, which is dependent on the X-ray source, describes the effect of the X-ray beam's polarization and can be calculated as follows [5, 86]

$$P = \begin{cases} 1 & \text{synchrotron: vertical scattering plane} \\ cos^2\theta & \text{synchrotron: horizontal scattering plane} \\ \frac{1}{2}(1 + cos^2\theta) & \text{unpolarized source} \end{cases} , \tag{2.7}$$

where the scattering angle is $\theta$.
The overall scattering amplitude $A(q)$ of $N$ electrons with the electron-electron distance $r$ is equal to the sum of scattered waves with a phase factor of $\exp(-iqr)$

$$A(q) = \frac{E_0}{L} \sum_j^N r_e \exp(-iqr_j). \tag{2.8}$$

Assuming a continuous density of electrons since there will be $\rho(r)$dr electrons in a dr-volume element, the total scattered amplitude can be written as

$$A(q) = \frac{E_0}{L} \, r_e \int \rho_e(r) \exp(-iqr) dr \, . \tag{2.9}$$

Therefore, the electron density distribution's Fourier transform is represented by the amplitude $A(q)$, and $q$ is the reciprocal space coordinate for momentum transfer.

In the case of the scattering from $N$ atoms, the scattering amplitude can be rewritten in the form of

$$A_{\text{atoms}}(q) = \frac{E_0}{L}\, r_e \sum_{j}^{N} f_j^{at}(q) \exp(-iqr_j) \tag{2.10}$$

where $f_j^{at}(q)$ represents the atomic form factor of the $j^{th}$ atom and $r_j$ specifies its location. If there are $N$ identical scatterers, then the amplitude form factor of a scatterer $F(q)$ can be calculated in the units of $r_e$. Through integrating over the particle volume $V_p$, $F(q)$ can be determined,

$$F(q) = \int_{V_P} \Delta\rho(r) \exp(-iqr) dr\,. \tag{2.11}$$

where $\Delta\rho$ is the density difference and is defined as

$$\Delta\rho(r) = \rho(r) - \tilde{\rho}\,. \tag{2.12}$$

In the Equation 2.12 $\rho(r) = r_e\rho_e(r)$ represents the scattering length density at point $r$, while $\tilde{\rho}$ represents the average scattering length density of the medium. The scattered intensity of $N$ particles is [5, 86]

$$I(q) = \sum |A(q)|^2 = \frac{I_0}{L^2} \left| \sum_{j}^{N} F(q) \exp(-iqr_j) \right|^2 . \tag{2.13}$$

Although it is true that Equation 2.13 has the same shape for scattering from atoms, molecules, and particles, the scattering from such systems will differ in the scattering angle or wave vector $q$.

## 2.2 Small Angle X-ray Scattering (SAXS)

SAXS is a technique based on elastic scattering to probe the structure of crystals, powders, gels, and liquid samples on length scales from nanometers to micrometers [108, 83]. There are numerous different approaches that can be categorized as small-angle scattering techniques, with distinctions mainly depending on the radiation source used and the distance between the sample and detector [5, 83]. Many researchers classify X-ray small-angle scattering as either small-angle X-ray scattering (SAXS) for $q > 0.1$ nm$^{-1}$ or ultra-small-angle X-ray scattering (USAXS) for 0.1 nm$^{-1}$ $< q <$ 1 $\mu$m$^{-1}$. The scattered intensity $I(q)$ can provide information regarding the sample's structure and shape [83, 104].

In the context of this research, SAXS and USAXS are the preferred methods for investigating protein dynamics. Due to the fact that the size of proteins ($\sim$ 5 nm) is larger than the wavelength of X-rays ($\sim$ 1Å), the scattering angles are extremely small.
The scattering patterns of proteins dispersed in solution reflect the size and shape of the proteins as well as their time-averaged spatial distribution [83]. The value of scattered intensity for identical particles exhibiting spherical symmetry can be characterized as the multiplication of the particle form factor $P(q)$ with the structure factor $S(q)$, which characterizes the spatial correlation among the particles

$$I(q) \sim P(q) \times S(q)\,. \tag{2.14}$$

For a diluted system with $N$ identical non-interacting particles, the interparticle interaction can be ignored, and it is acceptable to assume that the scattering length density is uniform [70, 88, 5]. The contrast of the scattering signal is then determined by the scattering length density difference, $\Delta\rho_s$, between particle material and the solvent, and the scattered intensity as a function of momentum transfer is calculated as follows [5, 108]

$$I_{saxs}(q) = I_0 \times V_s \times \phi_P \times \Delta\rho_s^2 \times V_p^2 \times |F(q)|^2\,, \tag{2.15}$$

where $V_s$ and $V_p$ represents the illuminated volume and the particle volume respectively and $\phi_p$ denotes the nanoparticle volume fraction. The scattering intensity per pixel of a protein solution can be calculated using

$$I_{saxs}(q) = F_c \times t_{exp} \times T_{sample} \times d \times \frac{d\Sigma}{d\Omega}(q) \times \Delta\Omega_{pix}\,, \tag{2.16}$$

here the incident flux is $F_c$, and $t_{exp}$ represents the exposure time, $T_{sample}$ is the transmission of the sample, and $d$ is the sample thickness. The solid angle that a single pixel covers is denoted by $\Delta\Omega_{pix} = (P/L)^2$, where $P$ is the pixel size and $L$ is the sample-to-detector distance [83]. The cross-sectional area for differential scattering in a protein solution, given as a function of volume, or the absolute scattering intensity, given as a function of unit $\mathrm{m}^{-1}$, is defined as

$$\frac{d\Sigma}{d\Omega}(q) = C \times M \times \bar{v}^2 \times \Delta\rho_s^2 \times p(q) \times S(q)\,, \tag{2.17}$$

where $C$ is denoting the protein concentration, $M$ is molar mass and $\bar{v}$ is the specific volume [83].

The formula for the average interparticle structural factor, S(q), is

$$S(q) = \frac{1}{N}\left\langle \sum_{j\neq k}^{N}\sum_{j}^{N} \exp(-iq(r_j - r_k))\right\rangle, \tag{2.18}$$

where $\langle ....\rangle$ represents the statistical mean of all orientations, $N$ is the number of particles, $r_j$ is the $j^{th}$ atom position, and $r_k$ is the $k^{th}$ atom position [83, 5]. Figure 2.2 depicts

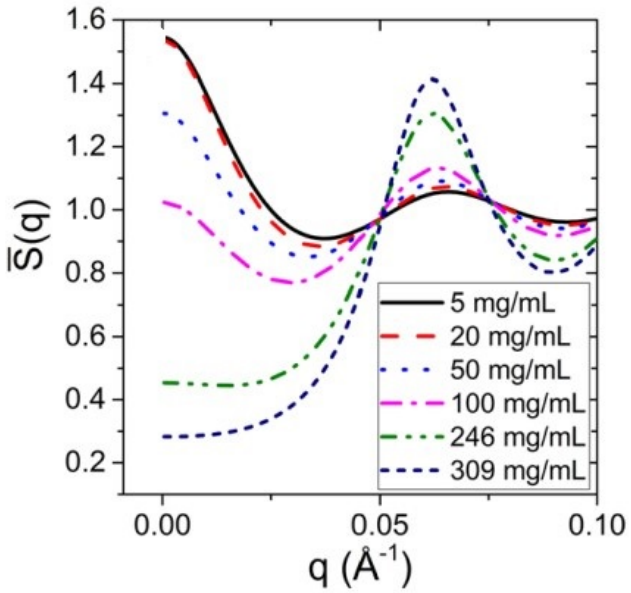


Figure 2.2: From the fit parameters for $\gamma$-globulin in buffer and pure water, structure factors were calculated [25].

the structure factor of IgG, which describes the intermolecular interactions between the proteins. Low protein concentrations, demonstrate a strong low $q$ upturn, confirming the presence of attractive interactions on the relevant length scale. The values of $S(q)$ for low $q$ diminish and eventually fall below one at higher protein concentrations [25, 84].
$P(q)$ is the particle form factor and defined as the square of the electric charge distribution's Fourier transform $\Delta\rho(r_j, t)$

$$F_j(q,t) = \int_V \Delta\rho(r_j,t)\exp(iqr_j)\,dV \tag{2.19}$$

$$P(q) = \langle |F(q)|^2\rangle \tag{2.20}$$

$$\begin{aligned} P(q) &= \langle F(q) \times F^*(q) \rangle \\ &= \left\langle \int \int_V \Delta\rho(r_1)\Delta\rho(r_2) \exp(iq(r_1 - r_2))\, dr_1 dr_2 \right\rangle \\ &= \left\langle \int \int_V \Delta\rho(r_1)\Delta\rho(r_1 - r) \exp(iqr)\, dr_1 dr \right\rangle \end{aligned} \tag{2.21}$$

applying $r = r_1 - r_2$. The auto-correlation function, $g(r)$, is calculated as the square of the density fluctuations $\Delta\tilde{\rho}^2(r)$.

$$g(r) = \Delta\tilde{\rho}^2(r) = \int_V \Delta\rho(r_1)\Delta\rho(r_1 - r) dr_1 \tag{2.22}$$

The particle form factor, using Equation 2.22 , can be rewritten as

$$P(q) = \left\langle \int g(r) \exp(iqr) dr \right\rangle. \tag{2.23}$$

Figure 2.3 depicts the form factors of geometric bodies as a function of momentum transfer $q$. If the q location of the first minimum is known, it is possible to estimate the particle radius $R$ [108, 84]. The form factor can be used to describe the shape of the protein and the effective protein-protein interactions [25].

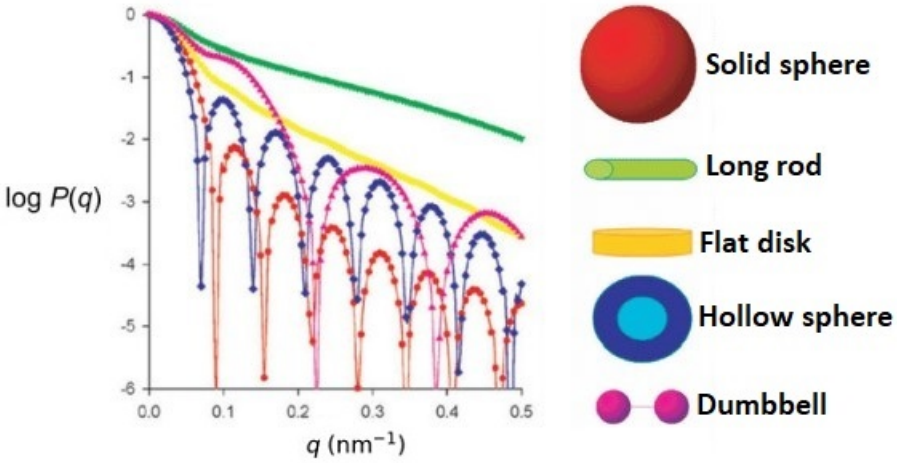


Figure 2.3: The form factors of geometric bodies with identical maximum sizes were calculated depending on the momentum transfer $q$, modified from [118].

## 2.3 Coherent x-ray beam and brilliance of the x-ray source

SAXS has been widely used at synchrotron light sources for decades. The emission of synchrotron radiation is triggered by the motion of charged particles along a curved path at relativistic speeds [5, 83]. An electron or positron beam is typically kept in circulation for several hours in a huge ring, where bending magnets maintain its circular route. Wigglers and undulators, two types of insertion devices, can be placed in the storage ring's straight parts [5, 128].
This research has taken full advantage of the synchrotron radiation's inherent brightness by performing scattering studies using X-rays generated in undulators. Figure 2.4 illustrates a simplified diagram of an undulator [5, 128]. Undulators are made up of vertically aligned dipole magnets of opposite polarity that are tightly spaced [90]. Since the electrons' paths through the undulator are not straight, they oscillate in the horizontal plane, and at each bend in the route. Then the electromagnetic radiation is released in a cone shape. When the radiation cones overlap, they cause constructive interference. This makes the X-ray beam have a high level of coherence. The advent of modern third-generation storage rings with partially coherent X-ray beams made possible a wide range of experimental techniques, such as X-ray photon correlation spectroscopy (XPCS)[5, 83, 128] .

## 2.4 Coherent X-ray scattering and speckle pattern

Experiments on coherent X-ray scattering are based on the measurement of interference events whose visibility rises as the coherence of the X-rays increases. Coherence is defined in terms of the mutual coherence function which is a measure of the correlation between the electric fields $E(r_1, t)$ and $E(r_2, t)$ [42]

$$C(P_1, P_2, \Delta t) = \langle E(r_1, t) \times E^*(r_2, t + \Delta t) \rangle_t \,. \tag{2.24}$$

$\langle .... \rangle$ represents a time average, which for any arbitrary function $f(t)$, can be calculated as

$$\langle f(t) \rangle_t = \lim_{t \to \infty} \frac{1}{t} \int_0^t f(t')dt' \tag{2.25}$$

The double-slit experiment of Young (Figure 2.5) is a fundamental illustration of a diffraction experiment. A plate with two pinholes, $P_1$ and $P_2$, is illuminated by a single

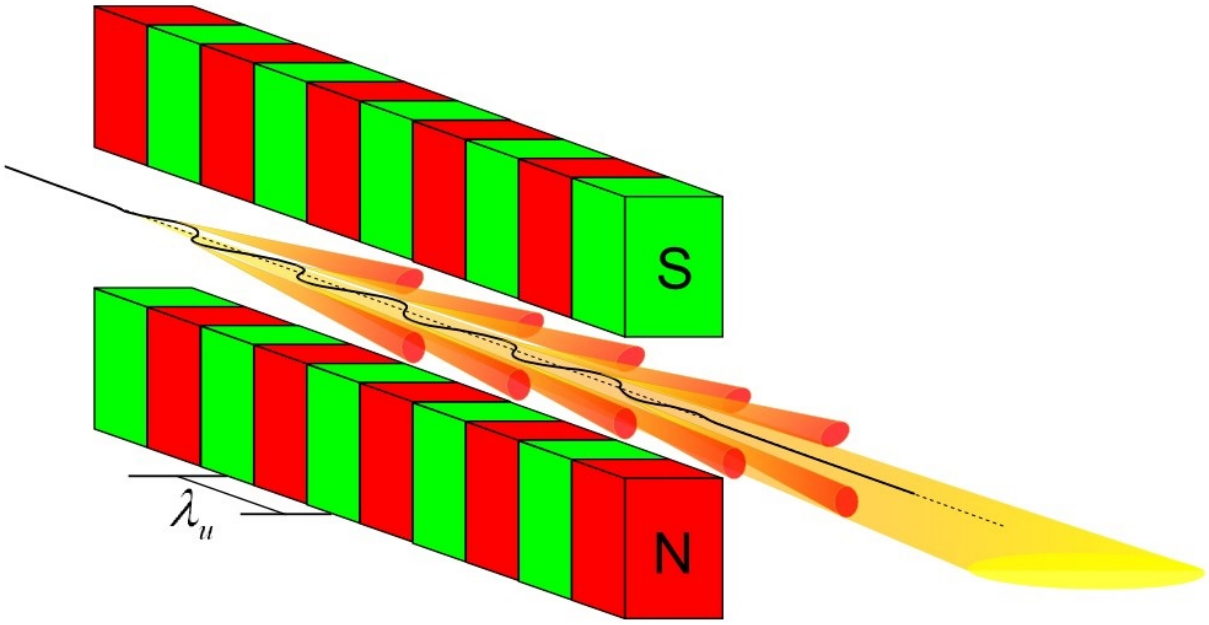


Figure 2.4: An undulator X-ray source, depicted above in schematic form, has a magnetic structure that generates a weaker magnetic field than a wiggler. Relativistic influences shorten the undulator's physical period length, $\lambda_u$, determining the wavelength of its maximum emission [127, 90]

light source, $S$. The intensity is measured at a point $q$ on the screen, which is located at coordinates $(r_1, r_2)$ behind the plate. As a function of $q$, the intensity is

$$I(q) = I_1(q) + I_2(q) + K_1 K_2^* C\Big(P_1, P_2, \frac{r_2 - r_1}{v_c}\Big) + K_2 K_1^* C\Big(P_2, P_1, \frac{r_1 - r_2}{v_c}\Big), \qquad (2.26)$$

where $v_c$ is speed of light and $K_1$ and $K_2$ are complex-valued vectors describing wave diffraction at the pinholes. According to Equation 2.26, the interference pattern is equal to the total of the intensities from the two pinholes $I_1(q)$ and $I_2(q)$, plus two interference terms that depend on the mutual coherence function. The normalized mutual coherence function is used to describe the complex degree of coherence.

$$\gamma(p_1, p_2, \Delta t) = \frac{C((p_1, p_2, \Delta t))}{\sqrt{I(P_1)\, I(P_2)}}, \qquad (2.27)$$

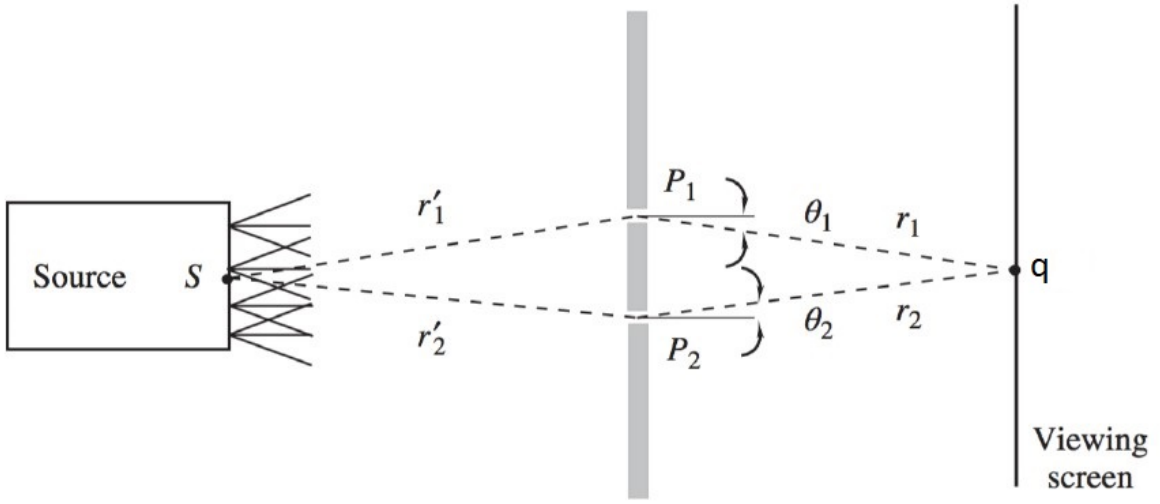


Figure 2.5: An illustration by Goodman depicts Young's double-slit experiment. Two pinholes, $P_1$ and $P_2$, are illuminated by light from source $S$. When the diffraction pattern is projected onto a screen, it is then evaluated at a certain point, $q$ [42].

where $I(P_1)$ and $I(P_2)$ are the averaged intensities shining through the pinholes. The following is a derivation of Schwarz's inequality [42]

$$0 \leq |\gamma(p_1, p_2, \Delta t)| \leq 1 \tag{2.28}$$

Equation 2.26, in its final form, can be expressed as

$$I(q) = I_1(q) + I_2(q) + 2\sqrt{I(P_1)\, I(P_2)}\left[\gamma\left(p_1, p_2, \frac{r_2 - r_1}{v_c}\right)\right]. \tag{2.29}$$

If the intensities on either side of the pinholes are identical ($I_1(q) = I_2(q)$), then the visibility of the fringes, also known as the contrast of the interference pattern, contrast $\beta_0$, is equal to the complex degree of coherence without a pathlength difference, $\gamma(p_1, p_2, 0)$.

$$\beta_0 = \frac{I_{max} - I_{min}}{I_{max} + I_{min}} = \gamma(p_1, p_2, \Delta t), \tag{2.30}$$

where $I_{max}$ and $I_{min}$ represent the interference pattern's maximum and minimum intensities, respectively [42, 118].

### 2.4.1 Speckle pattern

The conceptual concept of a double-slit experiment, in which just waves interfere, can be further extended to include the more complex situation of a speckle pattern (Figure 2.6). When coherent light is scattered from different components of a sample that arbitrarily add phase shifts to the incident radiation, then speckles will appear in the far field as an interference effect. The final waves display either constructive or destructive interference, or regions of an intermediate state, and this creates a complex pattern of dark and bright spots [17, 49] .

The scattered intensity from Equation 2.13, which describes speckles, is proportional to

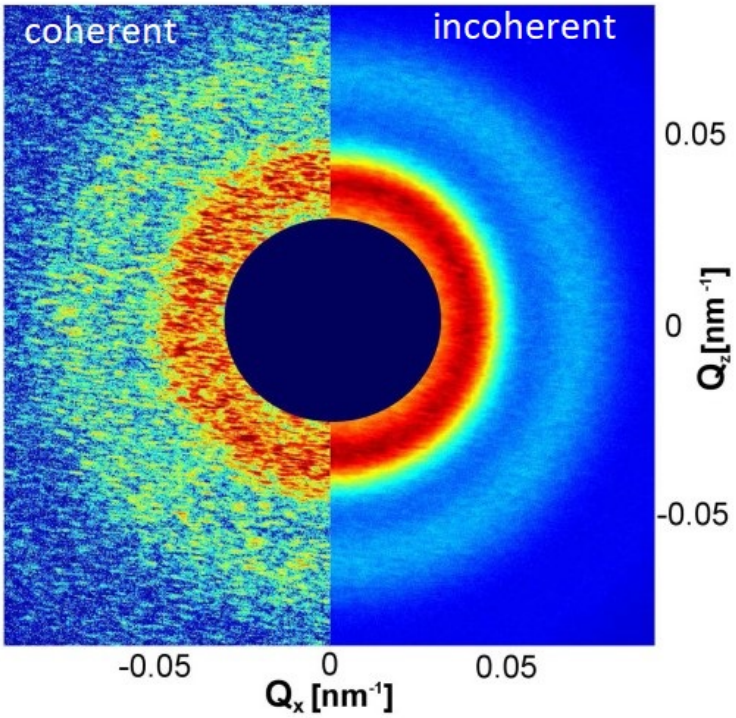


Figure 2.6: The colloidal sample's X-ray diffraction pattern. On the left is a single-shot coherent pattern. By comparing it to the scattering ring produced by a series of 50 separate shots, it is clear that there is a significant spatial intensity variability (right half). The direct beam is blocked from striking the detector by the circular shadow in the middle, which represents the beam stop [68].

the phasor amplitude $A(r)$ [41]

$$I(r) = |A(r)|^2 = \left| \sum_{k=1}^{n} |A_k(r)| \exp(-i\phi_k) \right| . \tag{2.31}$$

where amplitude and phase at the $k^{th}$ scattering zone are indicated by $|A_k|$ and $\phi_k$, respectively. As a result, in Equation 2.30, $\beta_0$ represents the speckle visibility or speckle contrast rather than the fringe visibility [116]. It can be approximated as [118, 118, 95],

$$\beta_0 = \int\int \exp\Big[-\Big(\frac{\Delta x}{\xi_t, h}\Big)^2\Big] \exp\Big[-\Big(\frac{\Delta y}{\xi_t, v}\Big)^2\Big] \exp\Big[-\Big(\frac{\tau_c v_c}{2\xi_l}\Big)^2\Big] dV_1 dV_2 \tag{2.32}$$

where $\xi_t, h$ and $\xi_t, v$ represent the horizontal and vertical transverse coherence lengths, respectively. V is the illuminated sample volume, and $\Delta_x$ and $\Delta_y$ are the horizontal and vertical distances between the two points on the observation plain [69]. The longitudinal coherence length, $\xi_l$, is the distance over which two waves can propagate before being completely out of phase. It is determined by the wavelength $\lambda$ and the wavelength variance $\Delta\lambda$ per [5, 99]

$$\xi_i = \frac{\lambda^2}{2\Delta\lambda}\,. \tag{2.33}$$

A higher degree of longitudinal coherence can be achieved by focusing on a single wavelength and limiting the bandwidth of a monochromator. In a similar manner, the transverse coherence length is defined as the spatial decorrelation lengths of two wavefronts caused by a finite divergence [42]

$$\xi_t = \frac{\lambda R_s}{2D_s}\,. \tag{2.34}$$

The variable $R_s$ is the size of the source, while the variable $D_s$ denotes the distance from the source. By reducing the emittance of a source, transverse coherence can be improved.

## 2.5 X-ray Photon Correlation Spectroscopy (XPCS)

X-ray photon correlation spectroscopy, often known as XPCS, can be used to analyze a wide range of materials and condensed matter systems [83, 82, 45]. In order to investigate nanoscale dynamics, XPCS employs a coherent X-ray scattering approach based on the observation of time-dependent fluctuations in the speckle pattern. Photon correlation spectroscopy, also called dynamic light scattering (DLS), is another method to study dynamics. It was first applied using coherent visible light [91, 117, 14].

Extending PCS to the X-ray region permits the study of dynamics on significantly smaller length scales. XPCS has an additional advantage over DLS because it is able to investigate opaque samples [89, 44, 135]. Figure 2.7 illustrates the frequency and wave vector range that XPCS can cover in compared to other methods. The present X-ray sources make

XPCS a powerful tool for investigating the slow nanoscale dynamics of matter, which cannot be studied using visible light techniques and cannot be probed using inelastic X-ray or neutron scattering. Also, Diffraction-Limited Storage-Rings (DLSRs) [128, 110] and X-ray Free Electron Lasers (XFELs) [75, 27], that have just been built or are in the process of being developed will make it possible to do ultrafast XPCS studies (up to $10^{13}$ Hz), giving a time-domain probe complementary to the inelastic scattering approaches.

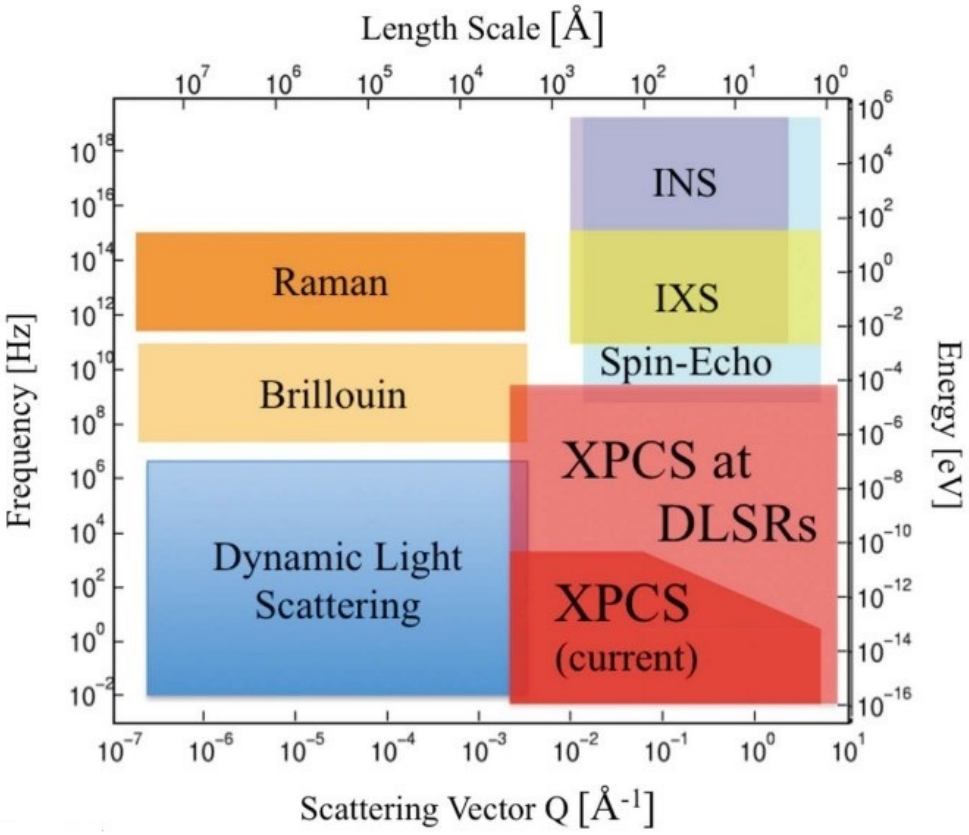


Figure 2.7: The approximate wave vector ranges and frequencies that can be accessed by various approaches using X-rays, visible light, and neutrons are depicted graphically [110, 27].

### 2.5.1 Intensity-intensity correlation function

Correlations in the intensity of X-ray scattering, measured in momentum space, are directly related to fluctuations in the order parameter, measured in real space [83, 89, 124]. Intensity fluctuations are monitored in an XPCS experiment as a result of the interference of X-rays scattered by particles that are randomly distributed. The resulting pattern is

known as a speckle pattern, and it contains areas of both constructive and destructive interference. In XPCS studies, the fluctuating intensity is used to learn about the dynamics of the sample by generating an intensity-intensity correlation function [81, 65]. A typical XPCS setup is illustrated in Figure 2.8. The intensity for every detector pixel fluctuates over time as a result of motion inside the protein sample. So, the intensity of a pixel at time $t$ is different from the intensity at time $t + \Delta t$, where $\Delta t$ is the delay time. $I(q, t + \Delta t)$ is correlated with $I(q, t)$ for minor delay times $\Delta t$ relative to the period of the measured fluctuation. The correlation disappears as the delay time increases [81, 101]. Autocorrelation functions measure the degree of correlation between images with total

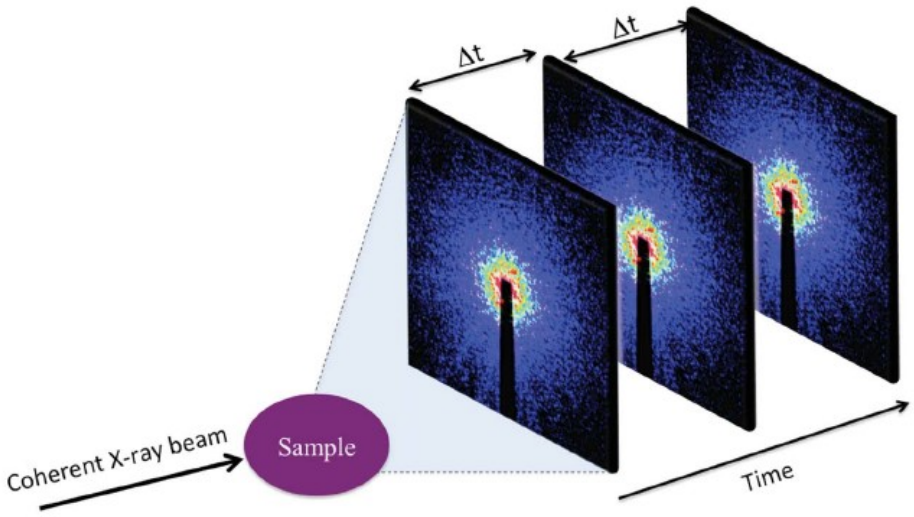


Figure 2.8: Schematic of a typical XPCS experiment: a protein sample scatters incoming coherent X-rays. A pixelated 2D array detector is used to capture speckle patterns with a delay time of $\Delta t$ [110].

time of measurement $T_e$

$$\langle I(q,t)I(q,t+\Delta t)\rangle = \lim_{T_e\to\infty}\frac{1}{T_e}\int_0^{T_e} I(q,t)I(q,t+\Delta t)dt\,. \tag{2.35}$$

Figure 2.9 illustrates the typical behavior of the correlation function, as described in Equation 2.35. If there is no time delay, then the equation becomes

$$\lim_{\Delta t\to 0}\langle I(q,t)I(q,t+\Delta t)\rangle = \langle I^2(q,t)\rangle\,. \tag{2.36}$$

$I(q,t)$ and $I(qt+\Delta t)$ fluctuations are uncorrelated for delay times much longer than the typical intensity fluctuation time $\tau$, therefore the average in Equation 2.35 can be divided in two for these situations

$$\lim_{\Delta t\to\infty}\langle I(q,t)I(q,t+\Delta t)\rangle = \langle I(q,t)\rangle\langle I(q,t+\Delta t)\rangle = \langle I(q,t)\rangle^2 . \tag{2.37}$$

The intensity correlation function thus decays from mean square intensity at short delay times to mean square intensity at long delay times.
The second-order correlation function of electric-field amplitude, expressed as a normalized version of the intensity correlation function

$$\begin{aligned} g^{(2)}(q,\Delta t) &= \frac{\langle I(q,t)I(q,t+\Delta t)\rangle_t}{\langle I(q,t)\rangle_t^2} \\ &= \frac{\langle E(q,t)E^*(q,t)E(q,t+\Delta t)E^*(q,t+\Delta t)\rangle}{\langle E(q,t)E^*(q,t)\rangle^2} . \end{aligned} \tag{2.38}$$

The Siegert relation establishes a relationship between the second-order correlation

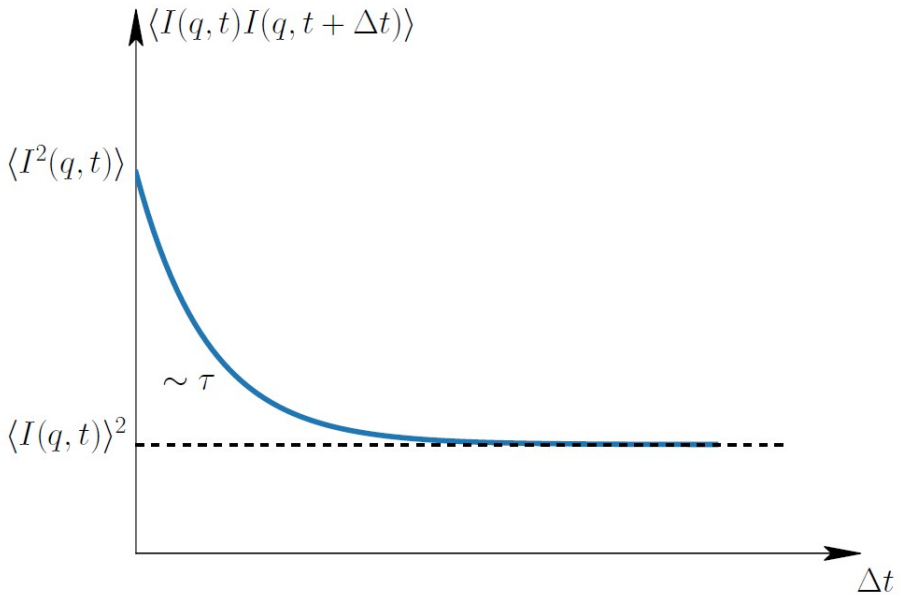


Figure 2.9: The time-dependent component of the correlation function decreases with a time constant that describes how long it usually takes for the scattered intensity to modify [108].

function $g^{(2)}(q,\Delta t)$ and the first-order correlation function $g^{(1)}(q,\Delta t)$ if the scattered

intensity follows Gaussian statistics

$$g^{(2)}(q, \Delta t) = 1 + |g^{(1)}(q, \Delta t)|^2 . \tag{2.39}$$

This relationship holds only if the source is fully coherent. When conducting a standard XPCS experiment, the source is only partially coherent, therefore Equation 2.39 requires some modification to

$$g^{(2)}(q, \Delta t) = 1 + \beta|g^{(1)}(q, \Delta t)|^2 . \tag{2.40}$$

The factor $\beta$ is known as the speckle contrast, Siegert factor, and coherence factor. The contrast is related to the complex degree of coherence, and it is possible to determine it experimentally by measuring the speckle patterns that come from a static sample [81].
The autocorrelation function denoted by $g^{(1)}(q, \Delta t)$ is also known as the normalized intermediate scattering function, which is used rather frequently. Depending on the dynamics of the sample, the intermediate scattering function can take on a variety of shapes. For diffusion in equilibrium, an exponential decay is a useful model

$$g^{(1)}(q, \Delta t) = \exp(-\Gamma \Delta t) . \tag{2.41}$$

Then the $g^{(2)}(q, \Delta t)$ can be written as

$$g^{(2)}(q, \Delta t) = 1 + \beta \exp(-2\Gamma \Delta t)^{\gamma} . \tag{2.42}$$

In the scenario of Brownian diffusive motion, the relaxation rate $\Gamma$ is determined by

$$\Gamma = Dq^2 . \tag{2.43}$$

Where $D$ refers to the Stokes-Einstein diffusion coefficient [34, 112]

$$D = \frac{k_b T}{6\pi\eta R_h} \tag{2.44}$$

where the hydrodynamic radius of the particle is $R_h$, and $T$ and $\eta$ are the temperature and viscosity of the medium, respectively.
In the Equation 2.42, $\beta$ is the speckle contrast and the dynamics of a sample can be characterized by the Kohlrausch-Williams-Watts (KWW) exponent ($\gamma$), and the decay rate ($\Gamma$). The exponent $\gamma$ provides information regarding the sample dynamics type. Brownian diffusive dynamics, for instance, lead to $\gamma = 1$. The colloidal gelation processes

are familiar with ballistic motion (a compressed exponential function), which results in KWW exponents $\gamma > 1$ and indicates a non-equilibrium dynamics [71, 47, 94]. Hence, the Equation 2.43 have a linear behavior

$$\Gamma \propto q\,. \tag{2.45}$$

Particles' sub-diffusive motion is commonly described by a stretched exponential function in the $\gamma < 1$, scenario. In metallic glasses, for instance, the evolution of correlation functions from a stretched exponential form ($\gamma < 1$) to a compressed decay mode ($\gamma > 1$) has been observed during the transition from the supercooled state to the glass state [6, 71].

The temperature dependency of the stretching exponential exponent (KWW) was also studied on sterically stabilized, $Si$ spherical nanoparticles mixed in a propanediol solution and a polypropylene glycol solvent [18, 22].

To characterize a system with two dynamical relaxations in a sample, a correlation function with two exponential terms is used as [12, 76]

$$g^{(2)}(q,\Delta t) = 1 + \beta_0 \left(\beta \exp(-2\Gamma_1 \Delta t)^{\gamma_1} + (1-\beta)\exp(-2\Gamma_2 \Delta t)^{\gamma_2}\right). \tag{2.46}$$

$\Gamma_1$ and $\gamma_1$ explain the localized dynamics, whereas $\Gamma_2$ and $\gamma_2$ describe the structural relaxation. $\beta_0$ is the speckle contrast determined by the experimental setup and scattering geometry, whereas $\beta$ represents the contrast between the two processes [16]. The relative contrast reduces as $q$ increases and is proportional to the localization length, $r_{loc}$, through a Debye-Waller-like factor [5]

$$\beta = \exp\left(\frac{r_{loc} q^2}{3}\right). \tag{2.47}$$

With Equation 2.47, XPCS measurements can be used to calculate the hydrodynamic correlation length. The localization length of the sample is related to the hydrodynamic correlation length through this relation [16]

$$\xi^* = r_{loc}^2\, 2R\,.$$

### 2.5.2 Two-time correlation function (TTC)

The time average in Equation 2.35 is only valid if the dynamics are stationary during the period of the measurement. If the measured system exhibits out-of-equilibrium behavior,

such as phase separation, aging, or radiation damage, it is not possible to obtain a reliable $g^{(2)}(q, \Delta t)$ using the same method [63]. Therefore, the analysis must be a function of the waiting time $t_w$ after the measurement begins. As an alternative to the temporal average, the ensemble average of equivalent scattering vectors can be utilized. In this context, we use the following definition for the two-time correlation function [12]

$$C(q, t_1, t_2) = \frac{\langle I(q, t_1) I(q, t_2) \rangle_q}{\langle I(q, t_1) \rangle \langle I(q, t_2) \rangle_q} \,. \tag{2.48}$$

Where, $\langle ... \rangle$ represents the average of all pixels, which corresponds to a spectrum of scattering vectors [63, 22]. Figure 2.10 displays a measured TTC of IgG+PEG protein system, which exhibits the influence of radiation damage.

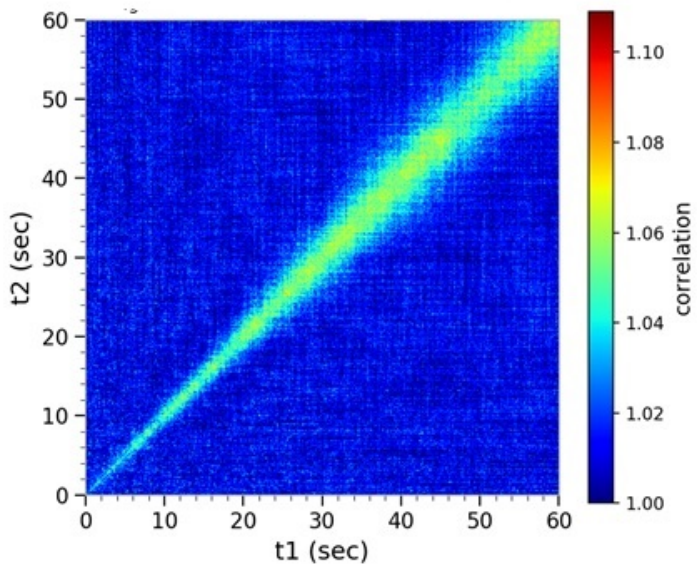


Figure 2.10: Two-time correlation function that describes non-equilibrium dynamics measured with an IgG-PEG protein sample.

## 2.6 Interaction of X-rays with Matter

The X-ray beam can be absorbed, scattered, or transmitted through the material without interaction [96]. The phenomenon of X-ray interaction with matter includes multiple components, such as the photoelectric effect, Compton scattering, elastic scattering, pair production, and nuclear interactions [5]. The signal under investigation in the USAXS-XPCS and SAXS-XPCS experiments relates to elastic scattering, as explained in section 2.1. The most significant interactions for attenuating photons in the XPCS energy range are the photoelectric effect and Compton scattering [5, 55].

During the photoelectric effect, the X-ray photon is completely absorbed, and a lower-level core electron is released from the atom. The radiation frequency has to be higher than the binding energy of a particular shell, which is dependent on the material's properties. Subsequently, the ionized atom has the capability to emit an Auger electron or X-ray with a unique characteristic. Photoelectron absorption may be predominant for energies up to 500 keV and atoms with large atomic numbers [5, 105].

In the Compton effect, an incident photon undergoes incoherent scattering with an electron, resulting in the transfer of a finite amount of energy to the electron. This phenomenon also results in the ionization of atoms. Compton scattering holds importance for low atomic numbers and energy levels within the range of 100 keV to 10 MeV [51].

The probability of the mentioned effects corresponds to their cross-sectional region. The energy dependency of the cross-section for various X-ray interactions with water is displayed in Figure 2.11. The experiments involving USAXS-XPCS and SAXS-XPCS, as described in this thesis, were conducted at energy levels of 8.54 keV and 13.8 keV. The predominant phenomenon in this energy range is the photoelectric effect, whereas the possibility of elastic scattering is comparatively lower by a factor of ten. The possibility of radiation damage may be attributed to the elevated occurrence of either the photoelectric effect or Compton scattering. In addition to the creation of high-velocity electrons, these interactions have the potential to induce the production of ions, secondary ionization occurrences, and free radicals. Soft-matter materials can suffer considerable harm to their molecular structure as a result [5, 105].

The study of the kinetics and dynamics of biological materials is hampered by the issue of radiation damage, which remains a significant obstacle. The biological sample undergoes primary damage within the femtosecond time frame subsequent to exposure under the influence of the extreme beam. Within the picosecond timeframe, there is a process of bond breaking and the generation of reactive objects such as solvated electrons, hydrogen,

and hydroxyl radicals. Within the temporal range of microseconds to milliseconds subsequent to exposure, the macromolecule exhibits bond breakage and the creation of additional radicals [119, 96].

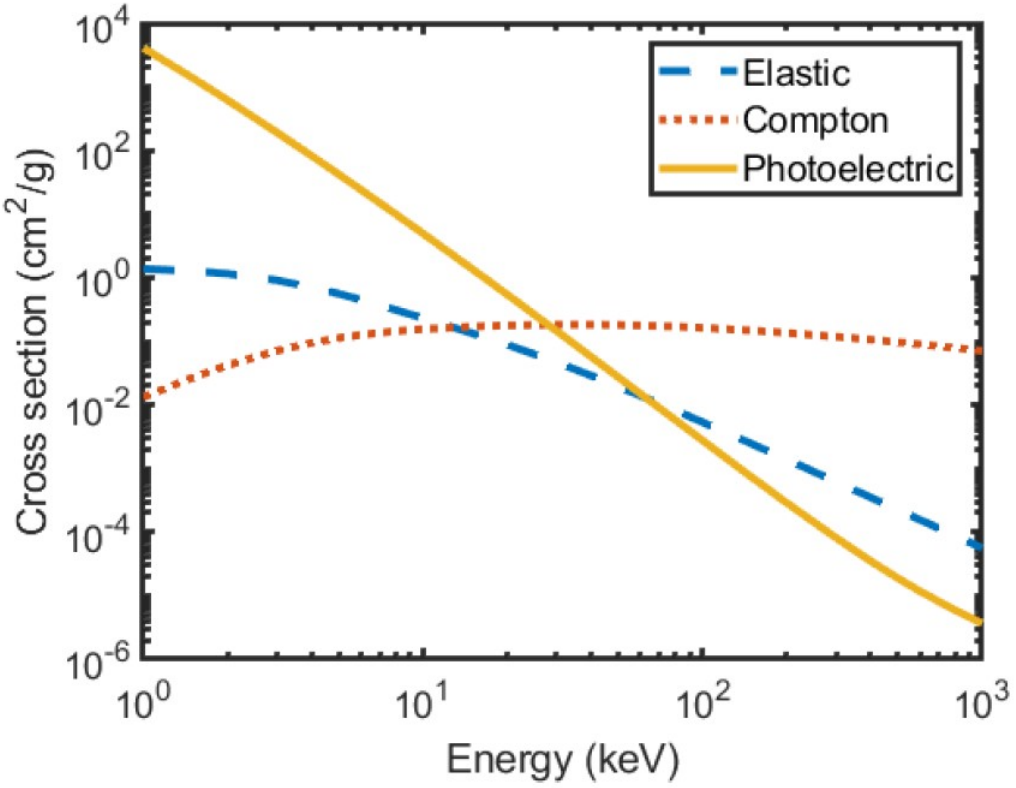


Figure 2.11: The depicted figures demonstrate cross-sectional representations of the photoelectric effect (yellow), elastic scattering (blue), and Compton scattering (red) at varying energy levels. The calculation of this dependency is related to water [96, 10].

### 2.6.1 X-ray Absorption

The absorption of an X-ray photon by an atom results in the transfer of excess energy to an electron, leading to its ejection from the atom and consequent ionization. The linear absorption coefficient $\mu$ is a quantitative indicator of x-ray absorption. The term $\mu dz$ denotes the attenuation of a beam as it passes through a sheet of infinitesimal thickness $dz$ situated at a depth z from the surface, as illustrated in Figure 2.12. Consequently, the condition that must be satisfied is that the intensity $I(z)$ passing through the sample should be fulfilled [5]

$$-dI = I(z)\mu dz, \tag{2.49}$$

which results in the differential equation

$$\frac{dI}{I(z)} = -\mu dz. \tag{2.50}$$

The solution is obtained by applying the condition that $I(z = 0) = I_0$, which represents the intensity of the incident beam at z = 0. This yields the following result

$$I(z) = I_0\, e^{-\mu z}. \tag{2.51}$$

The relationship between the number of absorption events, denoted as $N_{ab}$, occurring in a thin sheet and the incident intensity, I, is directly proportional. Additionally, $N_{ab}$ is also directly proportional to the atomic number density, $\rho_{at}$, which represents the number of atoms per unit area and is multiplied by the thickness of the sheet, $dz$. By definition, the absorption cross-section, $\sigma_a$, is the proportionality factor [5, 11]

$$N_{ab} = I(z)\, \rho_{at}\, \sigma_a dz\,. \tag{2.52}$$

The relationship between the absorption coefficient and the absorption cross-section is defined by

$$\mu = \frac{\rho_m N_a\, \sigma_a}{M}\,, \tag{2.53}$$

where $N_a$, $\rho_m$, and M represent, respectively, Avogadro's number, mass density, and molar mass. The total absorption probability for a layer of thickness $dz$ in a composite material comprising multiple atomic types, each characterized by a number density $\rho_{at,j}$ and an absorption cross section $\sigma_{a,j}$, is determined by the summation of $\sigma_{a,j}\, \rho_{at,j}\, dz$, which represents the total absorption probability for an atom of type j.

### 2.6.2 Effects of radiation on biological samples

In X-ray photon correlation spectroscopy, radiation damage is still a significant limitation and obstacle. Soft matter samples, particularly those of a biological nature, exhibit a high degree of susceptibility to radiation damage due to the relatively facile change of their molecular bonds. Protein aggregation is a result of radiation damage in X-ray experiments conducted at high-brilliance synchrotron sources [119, 105].
Water constitutes approximately 70% of the aqueous solution (protein solution), 60% of the human body and 80% of a cell [125]. It is possible that radiation primarily interacts

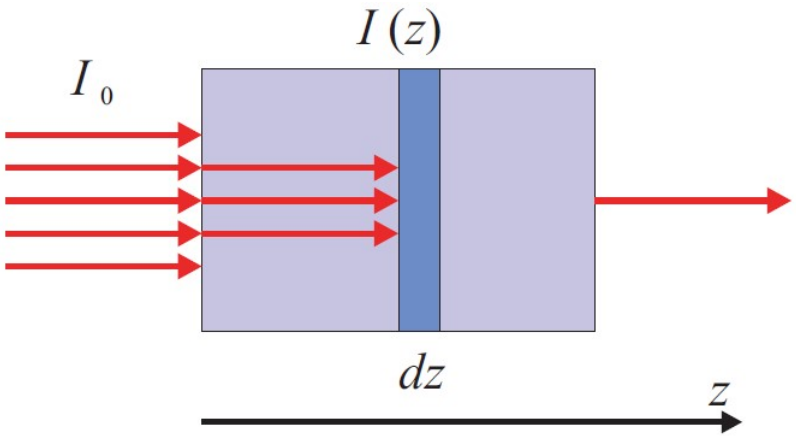


Figure 2.12: Absorption reduces the intensity of an X-ray beam passing through a material. For a given absorption coefficient $\mu$, the attenuation decreases at an exponential rate over a characteristic linear attenuation length of $\mu^{-1}$ [5].

with water molecules, resulting in the production of free radicals within the aqueous samples. In chemistry, a free radical is defined as an atom or molecule with an unpaired electron in its outer orbit [130]. The primary interaction of water with radiation, the water molecule may undergo ionization or excitation during the physical phase, leading to the production of excited water molecules ($H_2O^*$), ionized water molecules ($H_2O^+$), and sub-excitation electrons ($e^-$). During the physico-chemical stage, which occurs between $10^{-15}$ to $10^{-12}$ s, water molecules that are ionized and excited undergo transformations and release energy by transferring it to neighboring molecules and breaking bonds [105, 119]. This process happens in two steps. Initially, water molecules undergo ionization upon exposure to radiation, resulting in the formation of $H_2O^+$ and a liberated electron. Subsequently, the $H_2O^+$ ion and free radical exhibit a temporary existence, reacting with another water molecule shortly after their creation to produce hydroxyl radicals ($HO^{\cdot}$). The radical species diffuse in the solution after interacting with each other and surrounding molecules [119, 105].

Radiation has both direct and indirect effects. Direct radiation damage changes the molecular structure; however, in indirect radiation damage, X-rays interact with water molecules, leading to the formation of hydroxyl and hydroperoxyl radicals that have the potential to bind to proteins. Figure 2.13 depicts the production of free radicals resulting from the radiolysis and ionization of water [105, 119].

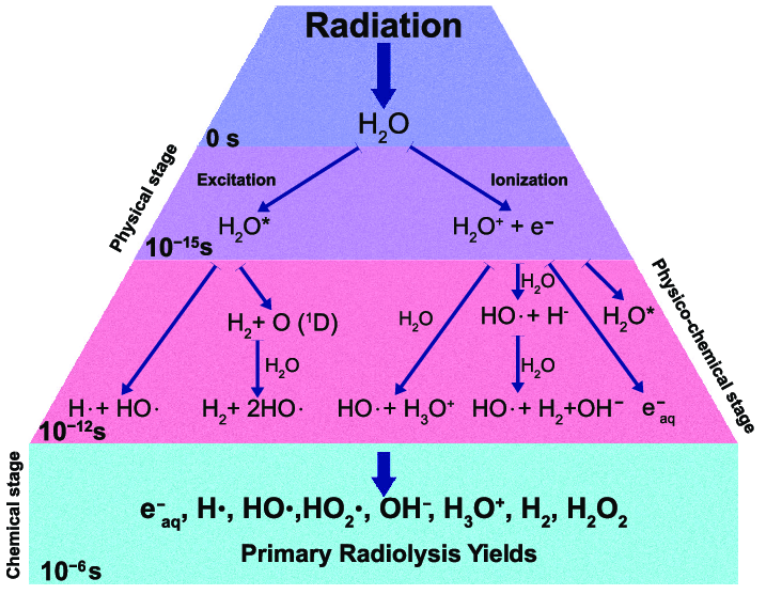


Figure 2.13: Schematic illustrating the production of free radicals during the radiolysis of water. The radiation reacts with the water, to make free radicals like hydrogen atoms ($H^+$), hydroxyl radicals ($HO\cdot$), and superoxide radical anion ($O_2^-$) [105, 125].

# Chapter 3

# Experimental part

In this chapter, we discuss the experimental realization of the methods that were introduced in the previous chapter (Chapter 2). In the beginning, we will discuss the preparation of the samples. After that, a brief introduction to synchrotron radiation is presented, followed by a description of the specific beamline setups utilized at PETRA III at the Deutsches Elektronen-Synchrotron (DESY). Measurement protocols that were created to work around technical challenges are discussed in the latter section of the chapter.

## 3.1 Sample preparation

The structure of immunoglobulin G (IgG) proteins as well as their interactions with each other were discussed in details in Sections 1.6 and 1.5. The protein utilized in this study was a polyclonal antibody purchased from Sigma-Aldrich (G5009) called bovine $\gamma$-globulin (Ig), also known as bovine $\gamma$-globulin. The agarose gel electrophoresis analysis indicates that the level of purity of this sample is higher than 99%. The protein product is composed of the immunoglobulin antibody classes: IgG (80%), IgM (10%), and IgA (less than 10%). Variations in protein powders can produce a slight shift in the phase borders of the solutions, but the phase behavior as a whole stays similar [24].

Polyethylene glycol (PEG), with a molecular weight of 1 kDa, is used as a depletion agent in the solution (Sigma-Aldrich, 81188, PEG 1000) [132, 30]. Polyethylene glycol, often known as macrogol, is a kind of polyether. It is found in many different foods, cosmetics, and medicines. The molecular formula is $C_{2n}H_{4n+2}O_{n+1}$, and its chemical structure is shown in Figure 3.1. The value of $n$ changes based on the molecule's molecular weight [132, 30].

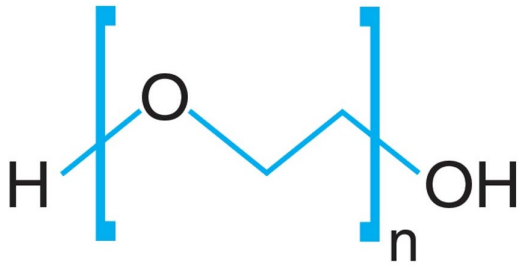


Figure 3.1: The chemical structure of polyethylene glycol 1000 [4].

### 3.1.1 IgG sample preparation

In order to prevent the proliferation of bacteria and yeast, the protein powder was dissolved in a buffer solution containing degassed pure water (Milli-Q grade), 20 mM HEPES pH 7.0, 150 mM NaCl, and 2 mM $NaN_3$. PEG 1000 (81188) and NaCl (106404) purchased from Sigma-Aldrich and Merck, respectively, were utilized as received. The parent solution included 200 mg $mL^{-1}$ of IgG and 10% PEG 1000. The concentration of each individual ingredient was adjusted to achieve the final result. All of the studied solutions were made at 21 °C and maintained at the same temperature for 24 hours [24]. The parent solution was quickly centrifuged to get two well-separated phases. Phase separation into a dilute and dense phase was apparent. Following this process, the dilute phase was removed and the dense phase was utilized. The dense phase was placed into quartz glass capillaries with a diameter of 1.5 mm and measured dynamic properties using USAXS-XPCS and SAXS-XPCS.

We used a Cary 50 Ultraviolet–Visible (UV-vis) spectrophotometer with an absorption coefficient of $\varepsilon_{280} = 1.4$ $mg^{-1}mL$ $cm^{-1}$, a quartz cuvette with a thickness of d = 1 cm, and the corresponding absorption values at $\lambda = 280$ nm to determine the concentration of the IgG stock solutions. Aromatic groups in the amino acids that compose proteins are effective at absorbing excess light at this wavelength. Using this information, one can estimate the concentration of proteins in a given volume of solution

$$C_p = \frac{A\lambda}{\varepsilon d}\,. \tag{3.1}$$

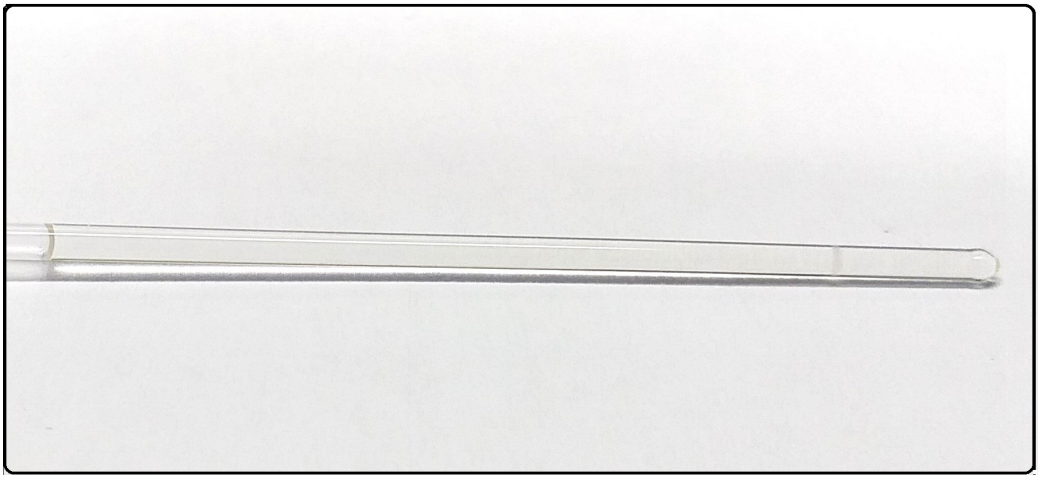

Figure 3.2: The IgG sample filled inside of capillary with a diameter of 1.5 mm.

Using a wavelength range of 300–800 nm and a scan speed of $2 \times 10^2$ nm $s^{-1}$ , spectra were collected against a background of pure water to measure the protein stability of solutions as a function of NaCl and $Na_2SO_4$ concentration [24].

### 3.1.2 BSA sample preparation

Bovine serum albumin (BSA) is another protein utilized in the present thesis work. BSA is a type of globular protein that is derived from cows and has a molecular weight of approximately 66 kDa [23]. It is composed of 583 amino acid residues and has hydrodynamic dimensions of 140 x 40 x 40 Å, reflecting an ellipsoid form factor. The structure of BSA has been reported to be about 55% helical and 45% disordered. Albumin is an essential factor in controlling plasma pressure. BSA has been extensively researched as a model protein due to its structural similarity to human serum albumin (HSA).
We used BSA from Sigma-Aldrich (Product No. A7906), with a stated purity of $\geq$ 98%, in this experiment. The protein stock solution was prepared by dissolving the required amount of BSA in ultrapure-degassed Milli-Q water (Merck Millipore, with a resistivity of 18.2 M$\Omega \cdot$ cm). Typically, the total protein concentration of the stock solution ranged between 300 and 400 mg $mL^{-1}$. The precise concentration value was determined through the utilization of UV absorption spectroscopy at a wavelength of 280 nm, employing Varian Inc [23].
In order to induce short-range attractive interactions between protein molecules, yttrium chloride ($YCl_3$) salt was added to a protein-containing aqueous solution. The phenomenon of lower critical solution temperature (LCST) through LLPS has been demonstrated in

the presence of Yttrium trichloride ($YCl_3$) for the BSA [79]. It has been observed that yttrium cations exhibit a binding affinity for proteins through an endothermic process driven by entropy. This interaction leads to the display of LCST behavior, which can be attributed to the entropic attraction between the two entities.
The compound $YCl_3$ was procured from Sigma-Aldrich under product code 451363, with a stated purity range of 99.9% to 99.99%. The salt stock solution was prepared by measuring the necessary quantity of salt and mixing it with ultrapure, degassed Milli-Q water to the desired concentration (typically 200 mM). The stock solutions of salt and protein were prepared at ambient temperature. The protein solution underwent homogenization for a duration of one day at a temperature of 4 °C [23].
For this work, stock solutions of protein and salt were combined at 21 °C by adjusting their concentrations with purified Milli-Q water to yield a final protein concentration of 175 mg $mL^{-1}$ and a salt concentration of 42 mM. The process of LLPS results in the separation of a protein solution into two distinct phases, one dense and the other dilute. Figure 3.3 depicts the phase diagram of the model system. Following the full-phase separation of the solution, the concentrated phase was selected for subsequent analysis. The dense phase was injected into capillaries made of quartz glass that had a diameter of 1.5 mm. The dynamic characteristics of the sample were then evaluated using SAXS-XPCS.

## 3.2 Experimental setup at PETRA III DESY

X-ray scattering experiments were performed at the German Electron Synchrotron (DESY) in Hamburg, which is equipped with a third-generation synchrotron called the Positron-Electron-Tandem-Ring-Anlage III (PETRA III) [1]. Synchrotron radiation refers to a type of electromagnetic radiation emitted by charged particles, typically electrons or positrons, while they undergo lateral acceleration perpendicular to their velocity direction [5]. At PETRA III, strong magnetic fields created by so-called bending magnets accelerate bunches of charged particles to relativistic energies of $E_e = 6$ GeV and drive them on a circular trajectory. Synchrotrons, also known as storage rings, are equipped with extra magnets that alter the direction and form of the particle bunches in order to maintain the circular orbit [5, 1].
For electromagnetic waves traveling at relativistic speeds, the Lorentz transform causes them to radiate in a forward-pointing cone in the laboratory reference frame. The emission of radiation caused by a relativistic charged particle that is travelling within

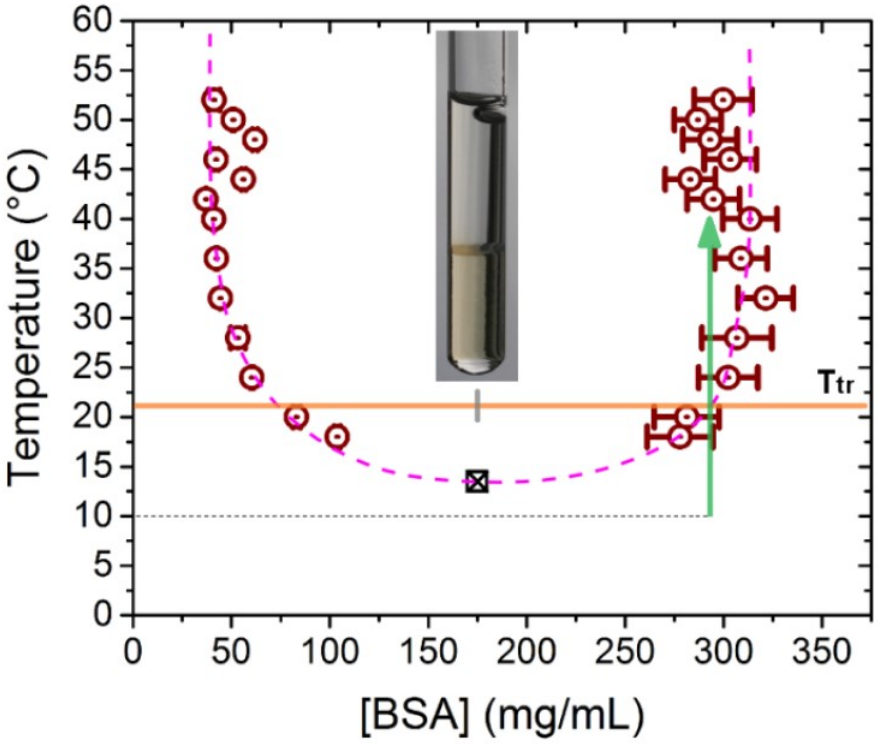


Figure 3.3: Binodal of the LLPS for the BSA-$YCl_3$ system with an initial concentration of 175 mg $mL^{-1}$ of protein and a salt concentration of 42 mM. The orange line indicates the sample preparation temperature for the primary solution. The critical temperature is indicated by a square in black. After phase separation, the dense phase is utilized in subsequent experiments. Its concentration is located where the green arrow and orange line intersect. The green arrow indicates an average temperature increase. The inset depicts a sample tube following LLPS and sedimentation. The yellowish portion represents the dense phase, whereas the transparent portion represents the dilute phase [23].

a circular orbit is concentrated into highly focused cones of radiation, as demonstrated in the simplified schematic in Figure 3.4, which shows a synchrotron radiation source sketching out its conical outward emission. The angle at which the X-ray cone opens is related to the inverse Lorentz factor and defined as

$$\gamma = \frac{1}{\sqrt{\left(1-\left(\frac{v}{c}\right)^2\right.}} \tag{3.2}$$

where $v$ is the electron velocity and $c$ is the velocity of light [5].
Brilliance $B$ is a common defining feature of synchrotron radiation sources, which is given

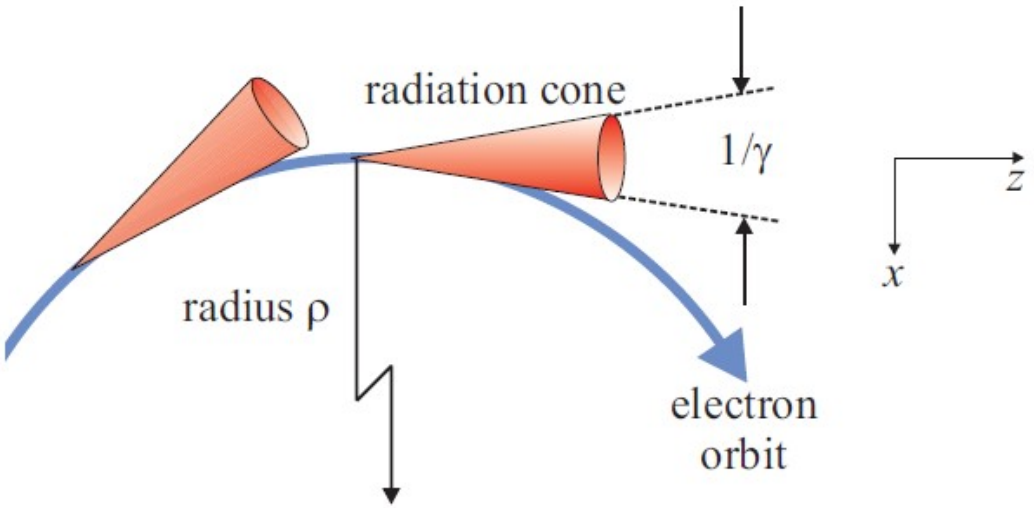


Figure 3.4: An electron traveling at relativistic speeds over a circular path of radius $\rho$. Emitted radiation is focused into a small cone centered on the instantaneous velocity and having an opening angle of $1/\gamma$ [5].

by

$$B = \frac{F_{ph}}{4\pi^2 \varepsilon_x \varepsilon_y} \tag{3.3}$$

where $F_{ph}$ represents the photon flux and $\varepsilon_x$, $\varepsilon_y$, indicate the emittance in the horizontal beam direction and the vertical beam direction, respectively. In most cases, the photon flux is expressed as ph $s^{-1}$ (0.1% BW)$^{-1}$, where BW refers to the energy bandwidth. High brilliance sources are advantageous for investigations that need coherent X-rays in particular because the coherent photon flux, $F_{ph}$, is proportional to both brilliance and photon wavelength, ($\lambda$) [1, 5]. The coherent flux of the source of X-ray radiation is

$$F_{ph} = \frac{B\lambda^2}{4}. \tag{3.4}$$

At PETRA III, undulators are installed in order to increase the photon flux. The undulator is constructed from arrays of permanent magnets that generate alternating magnetic fields with a spatial period of $\lambda = 2.9$ cm. Electron bunches are passed through undulators, which cause the charged particles to oscillate quickly in a direction perpendicular to their circular trajectories as a result of the Lorentz force.
The brilliance of PETRA III is on the order of $10^{21}$ ph $s^{-1}$ $mm^{-2}$ $mrad^{-2}$ (0.1% BW)$^{-1}$, which is approximately a factor $10^{13}$ greater compared to a conventional X-ray tube and

a factor $10^9$ greater compared to first-generation synchrotrons built on bending magnets [5, 1]. The fundamental wavelength that an undulator emits can be calculated as follows

$$\lambda = \frac{\lambda_u}{2\gamma^2}\Big(1 + \frac{K^2}{2}\Big)\,. \tag{3.5}$$

The undulator period, as well as the magnitude of the magnetic field $B_0$, are both important factors in determining the undulator parameter defined as K [5].

$$K = \frac{B_0 e \lambda_u}{2\pi m_e c} \approx 0.934 \lambda_u B_0\,, \tag{3.6}$$

where e and $m_e$ represent the charge and mass of the electron, respectively. Equation 3.6 demonstrates that the wavelength can be altered by simply adjusting the value of $B_0$, which can be accomplished by adjusting the distance that separates the two parts of the undulator.

### 3.2.1 P10 Beamline Setups

Since all experiments were conducted on the P10 synchrotron beamline, this part will describe the fundamental concept of an XPCS beamline. A schematic of the P10 and its optical components that are used to tune the beam characteristics is presented in Figure 3.5. At PETRA III, the 5 m-long undulator called U29 supplies the beamline's synchrotron radiation with a brilliance of

$$B = 4 \times 10^{20}\,\frac{\text{photons}}{\text{s}\,\text{mm}^2\,\text{mrad}^2\,0.1\,\%BW}\,.$$

P10 has three hutches, one is for optics (OH), and the other two are for experiments (EH1 and EH2). After the undulator, two power slits (PS1, PS2) determine the initial beam shape. The X-ray beam must first pass through the optics hutch, where the energy is adjusted by a two-bounce Si(111) high heat load monochromator (HHM). The monochromator is able to increase the longitudinal coherence length by reducing the bandwidth to

$$\frac{\Delta\lambda}{\lambda} \approx 10^{-4}\,.$$

In order to filter the higher harmonics of the undulator spectrum, two incidence mirrors (M1 and M2) are installed. The main wavelength is fully reflected whereas higher-

frequency photons are absorbed because the critical angle is proportional to the X-ray wavelength. Thus, the heat generated by the subsequent optical components is diminished. Inside the first experimental hutch, a fast shutter (FS) operating at 10 Hz is placed. The beam size at the sample is defined by the guard slits (G1, G2), which also serve to attenuate parasitic scattering. Focusing the beam and shrinking its size on the sample to a few micrometers is made possible by compound refractive lenses (CRLs). The detectors (D) are positioned on a moveable table following a 5-meter-long flight path that is evacuated. In USAXS geometry, the sample is placed in EH1, and the beam size on the sample is set by G1. This size is usually a few tens of micrometers .

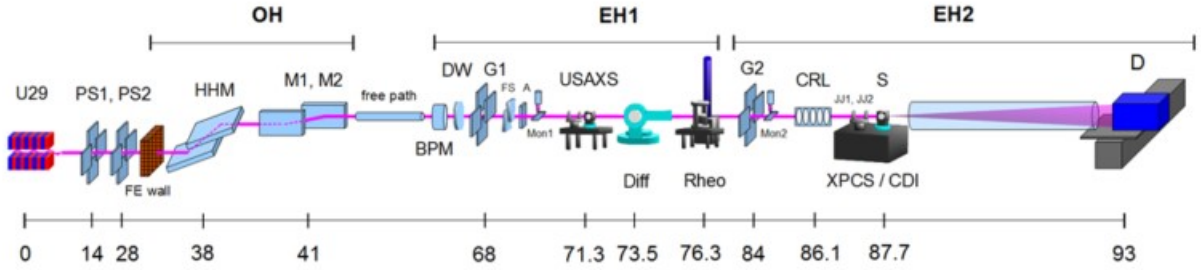


Figure 3.5: The configuration of DESY's Coherence Applications Beamline P10. The beamline consists of three parts: the optics hutch (OH), the first experimental hutch, and the second experimental hutch (EH1, EH2). The most important parts of the XPCS study are the undulator (U29), the power slits (PS1, PS2), the high heat load monochromator (HHM), the two mirrors (M1, M2), the guard slits (G1, G2), the sample chamber position (USAXS), and the detector (D) at the end of the beamline. In the SAXS XPCS configuration, the sample is placed at position S, and the X-ray beam is focused using compound refractive lenses (CRL) [1].

### 3.2.2 SAXS Setup

The sample is placed in EH2 in the SAXS geometry, and the beam size on the sample is determined by slit G2. For the measurements, an X-ray beam with a photon energy of 13.1 keV, a focusing beam size of 21.4 × 12.6 $\mu m^2$, and a maximum photon density of $F_{ph} \approx 10^7$ photons $s^{-1}$ $\mu m^2$ have been used. At a distance of 5 m from the sample, a 4-megapixel EIGER detector was employed to record time series of coherent diffraction patterns over a q range of

$$0.03\,\mathrm{nm}^{-1} \leq q \leq 1\,\mathrm{nm}^{-1}\,.$$

Due to the high sensitivity of protein samples to x-ray radiation, silicon absorbers are used to attenuate the incident beam and an x-ray shutter were utilized to control the photon density and reduce the absorbed dose.

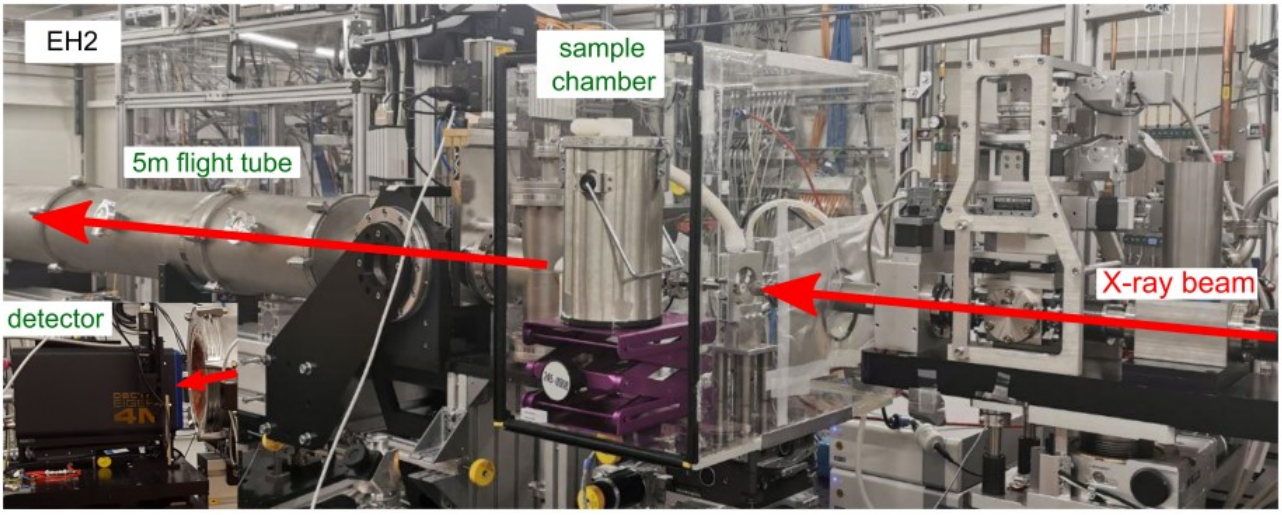


Figure 3.6: P10 Coherence applications Beamline SAXS configuration. The configuration of the sample chamber corresponds to the USAXS configuration [98].

### 3.2.3 USAXS Setup

In the USAXS geometry, the sample is placed in EH1, and the beam size on the sample is determined by slit G1, which is typically a few tens of micrometers in size. In this configuration, it would be possible to use a reasonably large beam size in order to facilitate the performance of low-dose XPCS experiments. For the measurements, an X-ray beam with a photon energy of 8.1 keV, a beam size of $100 \times 100\ \mu\text{m}^2$, and a maximum photon density of $F_{ph} \approx 10^7$ photons $\text{s}^{-1}\ \mu\text{m}^2$ have been used. At a distance of 21.2 m from the sample, a 4-megapixel EIGER detector was employed to record time series of coherent diffraction patterns over a q range of

$$0.003\,\text{nm}^{-1} \leq q \leq 0.05\,\text{nm}^{-1}\,.$$

In order to adjust the photon density and reduce the absorbed dose, silicon absorbers and X-ray shutter were used as a means of attenuating the incident beam.

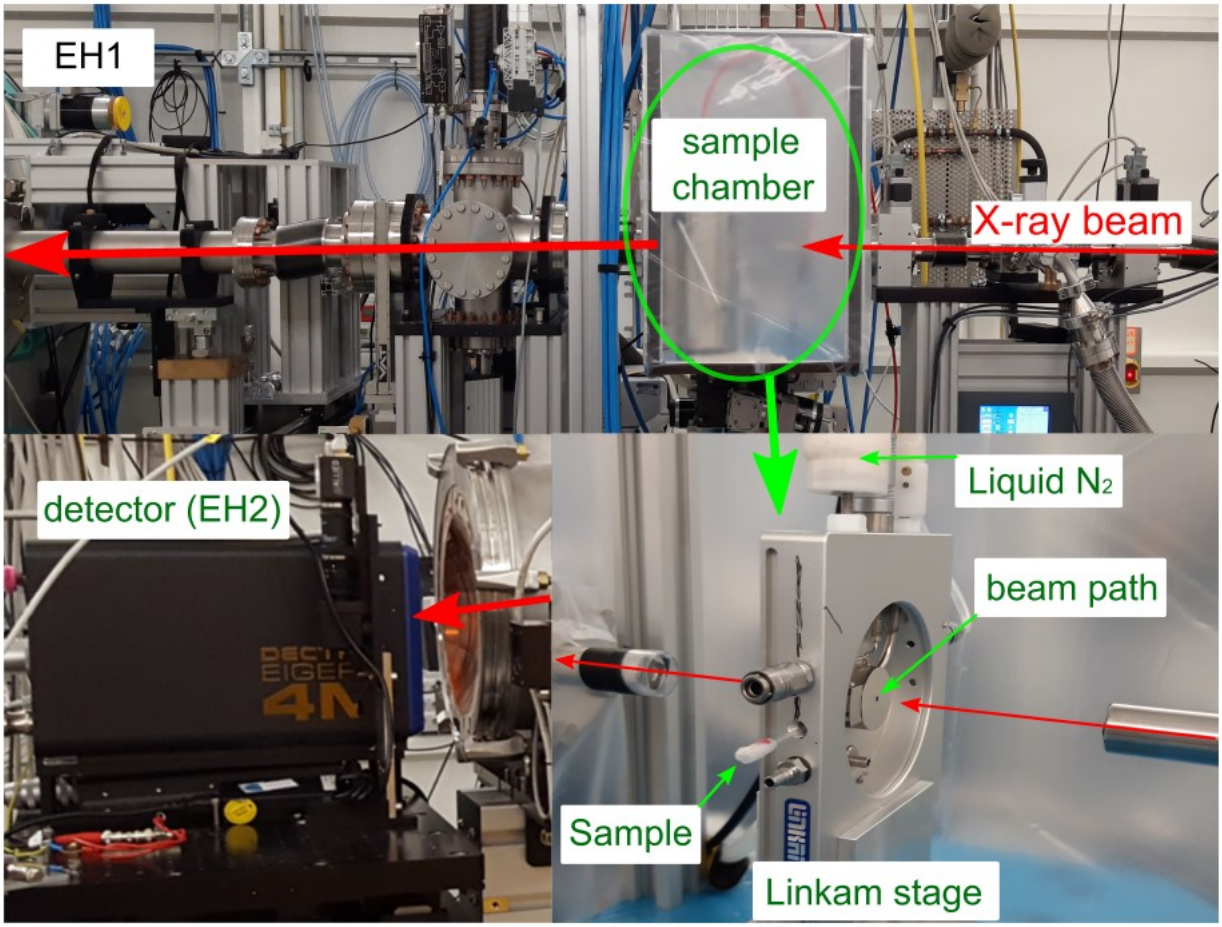


Figure 3.7: USAXS configuration at the P10 Coherence applications Beamline. Sample chamber within the first experimental enclosure. EIGER 4M detector fitted at the end of the 21 m evacuated flight tube in the second experimental hutch (bottom left) [98].

### 3.2.4 Acquisition of data using the EIGER 4M detector

The XPCS measurements were conducted with an EIGER 4M detector, which was used to collect the X-ray scattering series. In order to take measurements with delay times in the microsecond regime, fast X-ray detectors that can acquire data at repetition rates of kHz or faster are required. The shortest time scale observable by XPCS is restricted by the maximum repetition rate of the detector, $f_{max}$. It indicates the minimum delay time, which is the first point on the correlation function. The EIGER 4M detector has the capability to record X-ray scattering series with the parameters of the number of images $N_{im}$ and the single image exposure time $t_{exp}$. The EIGER 4M has a reading time of $t_r = 10\ \mu$s [59]. It can't measure photons for the whole period $\Delta t_0$ because it needs time to

| Specifications of EIGER 4M detector | |
|---|---|
| Pixel size (W x H) | 75 $\mu$m × 75 $\mu$m |
| Number of pixels | 2070 × 2167 |
| Maximum frame rate | 750 Hz |
| Adjustable threshold energy range | 2.7-18 keV |
| Sensor materia | Silicon (Si) |
| Sensor thickness | 450 $\mu$m |
| Inactive area | 5.6 % |

Table 3.1: Technical specifications of EIGER 4M detector at DESY P10 beamline [2, 59].

read out the data and get ready for the next capture. Therefore,

$$\Delta t_0 = t_{del} + t_f + t_r \tag{3.7}$$

where $t_f$ represents the frame time, and $t_{del}$ is the delay time. The measurement time $T_m$ determines the maximum correlation time

$$T_m = N_{img} \times \Delta t_0 \tag{3.8}$$

where $N_{img}$ represents the number of acquired images. Table 3.1 summarizes the different technical specifications of the EIGER 4M detector.


Figure 3.8: The high-resolution photon counting x-ray detector known as the EIGER 4M has been installed at the USAXS and SAXS setups of the P10 beamline [2, 59].

### 3.2.5 Linkam Stage

The protein samples were set up inside a Linkam heating stage, which has the capability of adjusting the temperature of the sample at a quench rate of up to 150 K per minute. Electric heaters is applied by the Linkam stage in order to increase the sample's temperature up to the desired level, and a connection to liquid nitrogen is responsible for providing the cooling function. As shown in Figure 3.9, the Linkam stage has a slot that can accommodate sample capillaries with a diameter of 1.7 mm, and it can be moved in all three spatial directions using motors. The stage consists of a silver block through which the capillary passes and a 2 mm hole where the X-ray beam could interact with the sample without touching the block itself. The temperature stability is within 0.1 °C, and the temperature range is from -195 °C to 350 °C.

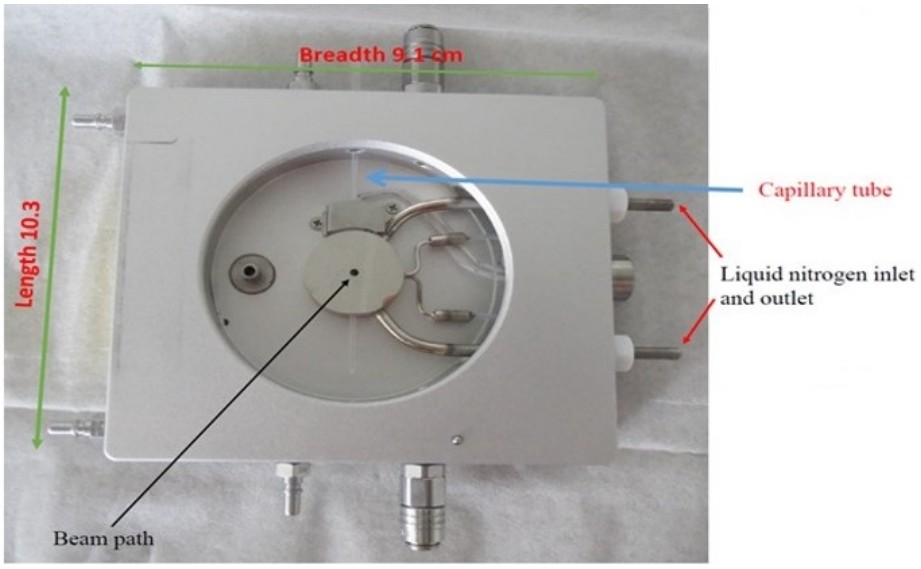


Figure 3.9: Schematic representation of the Linkam stage, with the capillary tube for the liquid sample measuring 1.7 mm in diameter and passing through the heating blocks [3].

## 3.3 Measurements protocol

The sample capillary was inserted within the sample chamber of the Linkam stage, as shown in Figure 3.9. The sample's temperature is controlled by the Linkam stage. In both the USAXS and SAXS setups, the experiment began with the identification of the sample beam damage threshold. Thus, the temperature of the sample was fixed at 37

°C, where there is no phase separation. By analyzing X-ray-induced modifications to the static SAXS patterns of the homogeneous sample, the thresholds of maximal photon densities and X-ray exposure times were defined. For this purpose, a series of X-ray scattering measurements were performed with different numbers of images and intensities of radiation. Following the determination of these thresholds for radiation damage, a protocol for XPCS measurements was developed that satisfied the standards for the safest possible dose. To prevent avalanche events produced by elastic rearrangements within the sample, both the USAXS and SAXS measurements were taken at sample spots about 1 cm from the bottom of the capillary.

### 3.3.1 Measurements using the Linkam stage

Experimental difficulties arise when working with temperature-sensitive samples in systems that are sensitive to changes in temperature, such as the polymer-protein combination in solution studied in this thesis. At a high temperature (T > 21 °C), the IgG solution is homogeneous and in one phase with a concentration of $C_i$. However, when the solution is quenched to a temperature below 21 °C, the solution separates into two phases with concentrations $C_{dilute}$ and $C_{dense}$, and domains grow over time. By bringing the temperature down to T, the separation will occur once more. This separation can be triggered again by lowering the temperature to $T_l < T$ . By raising the temperature above 21 °C and allowing it to equilibrate, it is possible to erase the system's memory. In this manner, the solution can reach its original condition, where all domains have been dissolved and it is stable at its initial concentration $C_i$. Each temperature quench was executed by decreasing the system's temperature from 37 °C to a predetermined temperature $T_q$. Subsequently, the system was allowed to reach equilibrium at $T_q$ for a period of 10 minutes.

### 3.3.2 Measurements using SAXS-XPCS setup

In the SAXS setup, the goal was to evaluate dynamics on the length scale of a single protein and examine the influence of X-ray dose and dose rate on the dynamics of phase-separated IgG proteins. The dynamic parameters of the phase-separated protein solution were studied by taking measurements at different temperature. The sample was quenched to the target temperature $T_q$, and measurements were taken 10 minutes later to ensure that this stage had been reached. The biggest challenge was the fact that the scattering intensity at large q values ($\approx 1$ nm$^{-1}$) decreases by four orders of magnitude in comparison to the intensity of the q values obtained by the USAXS experiment. Thus,

| $T_q$ (°C ) | $N_{img}$ | $N_{rep}$ | $t_{del}(s)$ | $t_{exp}$ | $N_{att}$ |
|---|---|---|---|---|---|
| 6 | 800 | 200 | 0 | 0.005 | 0 |
| 6 | 600 | 100 | 0.5 | 0.1 | 4 |
| 0 | 600 | 5 | 0 | 0.1 | 6, 8, 12, 16, 18 |
| 6 | 600 | 5 | 0 | 0.1 | 6, 8, 12, 16, 18 |

Table 3.2: The SAXS-XPCS measurement parameters.

it was not possible to generate a correlation function capable of analysis from a single X-ray scattering series. In order to get an acceptable signal-to-noise ratio (SNR), the number of repetitions (Nrep) was raised and the correlation functions of many series were combined. Figure 3.10 depicts that each repetition was recorded at a distinct fresh sample point, with a total of 60 spots per capillary. Table 3.2 displays the obtained SAXS-XPCS measurement parameters.

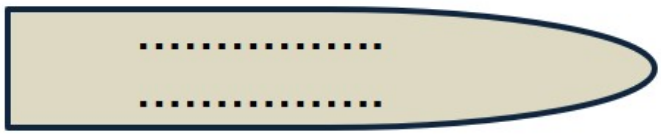

Figure 3.10: Each repetition was recorded in a fresh sample point.

### 3.3.3 Measurements using USAXS-XPCS setup

The goal of the USAXS-XPCS experiments was to understand the influence of X-ray dose and dose rate on the structure and dynamics of phase-separated IgG proteins. Table 3.3 displays the obtained USAXS-XPCS measurement parameters. The sample of the IgG model system was measured through quenches from the homogeneous phase at 37 °C to various temperatures below the binodal line. In this setup also, the sample was quenched to the target temperature $T_q$, and measurements were taken 10 minutes later to ensure that this stage had been reached, and each repetition was recorded in a fresh sample spot. A summary of the USAXS-XPCS measurement parameters is provided in Table 3.3.

### 3.3.4 Calculation of Flux and Dose rate

Proteins and numerous other soft matter or biological samples are highly sensitive to radiation damage. Therefore, in order to optimize the experiment, it is also necessary

| $T_q$ (°C ) | $N_{img}$ | $N_{rep}$ | $t_{del}(s)$ | $t_{exp}$ | $N_{att}$ |
|---|---|---|---|---|---|
| 6 | 5000 | 5 | 0.1 | 0.1 | 0, 4, 8, 12, 16 |
| 0 | 5000 | 5 | 0.1 | 0.1 | 0, 4, 8, 12, 16 |

Table 3.3: The USAXS-XPCS measurement parameters.

| $N_{att}$ | Si. $d(\mu m)$ | $T_{att}$ (%) | Flux (ph $s^{-1}$) | Dose (kGy $s^{-1}$) |
|---|---|---|---|---|
| 0 | 0 | 100 | $13\times10^{10}$ | 286 |
| 4 | 100 | 72.60 | $9.4\times10^{10}$ | 208 |
| 6 | 150 | 61.87 | $8.04\times10^{10}$ | 177 |
| 8 | 200 | 52.70 | $6.86\times10^{10}$ | 151 |
| 12 | 300 | 38.28 | $5\times10^{10}$ | 109 |
| 16 | 400 | 27.79 | $3.9\times10^{10}$ | 89 |
| 18 | 450 | 23.68 | $3\times10^{10}$ | 67 |

Table 3.4: The transmission values $T_{att}$ of Si attenuator, the incident flux, and the dose rate for the SAXS-XPCS setup.

to take into account the radiation dose, D, absorbed by the illuminated sample volume during a measurement. The dose D at which radiation-induced damage begins to degrade a sample can be expressed as follows:

$$D = \frac{F_{ph}E(1 - T_{sample})t_{exp}}{d(E)a^2\rho}\,, \tag{3.9}$$

where $F_{ph}$ represents the photon flux on the sample, $T_{sample}$ is the sample transmission, $t_{exp}$ is the exposure time, $d(E)$ is the energy-dependent sample thickness, $a^2$ is the beam area, E is the photon energy, and p is the mass density of a water equivalent (1000 kg $m^{-3}$) [83, 80].

The flux was reduced further by sets of silicon attenuators, with attenuator number n equal to the thickness of a silicon wafer $d = n \times 25\,\mu$m. The experimental attenuation unit is achieved through combinations of attenuators of different thicknesses, allowing for only particular values of n. The reduced flux for attenuator n is derived from the X-ray transmission of a single silicon wafer (73%), using the formula:

$$F_{ph}^n = F_0 \times (0.73)^n\,, \tag{3.10}$$

| $N_{att}$ | Si. $d(\mu m)$ | $T_{att}$ (%) | Flux (ph $s^{-1}$) | Dose (kGy $s^{-1}$) |
|---|---|---|---|---|
| 0 | 0 | 100 | $6\times10^{10}$ | 4 |
| 4 | 100 | 28.72 | $1.7\times10^{10}$ | 1.1 |
| 8 | 200 | 8.25 | $5\times10^{9}$ | 0.3 |
| 12 | 300 | 2.37 | $1.4\times10^{9}$ | 0.09 |
| 16 | 400 | 0.68 | $0.4\times10^{9}$ | 0.032 |

Table 3.5: The transmission values $T_{att}$ of Si attenuator„ the incident flux, and the dose rate for the USAXS-XPCS setup.

where $F_0$ represents the photon flux without an attenuator [83, 80]. The transmission values $T_{att}$ of Si attenuator, the incident flux, and the dose rate for the SAXS-XPCS setup are shown in Table 3.4, and these parameters for the USAXS-XPCS setup are shown in Table 3.5.

### 3.3.5 Signal-to-Noise Ratio (SNR)

The XPCS technique depends on the accurate determination of the scattered signal visible in each diffraction pattern. Therefore, it is essential to optimize the experimental parameters to achieve a sufficient signal-to-noise ratio (SNR) [83, 33]. The signal-to-noise ratio (SNR) affects the quality of the obtained TTCs and autocorrelation function $g^2(t)$. It can be determined through the following equation [83, 33]

$$SNR = \beta \times I_{pix} \times \sqrt{N}\,, \tag{3.11}$$

with

$$N = N_{pix} \times N_{Ima} \times N_{rep}. \tag{3.12}$$

In this expression, $I_{pix}$ represents the average intensity across all pixels, $\beta$ is the contrast, $N_{pix}$ denotes the number of pixels, $N_{Ima}$ is the total number of frames captured during the XPCS experiment, and $N_{rep}$ is the number of repetitions the experiment was repeated. The relation between the signal-to-noise ratio (SNR) and the experimental parameters was determined in reference, and Equation 3.11 can be modified accordingly

$$SNR = \beta(a,\lambda,L) \times I_{pix}(\lambda,L) \times \sqrt{N_{pix}(L,\lambda) \times N_{Ima}(a,\lambda) \times N_{rep}}\,, \tag{3.13}$$

where L is the sample-to-detector distance, a is the beam size, and $\lambda$ is the x-ray wavelength. The $I_{pix}$ value is directly proportional to the incoming coherent flux $F_c$ and can be given by

$$I_{pix} = F_c \times t_{ex} \times T_{sample} \times d \times \frac{d\Sigma}{d\Omega} \times \Delta\Omega_{pix}, \tag{3.14}$$

where $t_{ex}$ is the exposure time for each frame, $T_{sample}$ is sample transmission, and $\Omega_{pix}$ represents the solid angle covered with a single pixel. The incident coherent photon flux can be given as

$$F_c = B\frac{\lambda^2}{4}, \tag{3.15}$$

where

$$B = \frac{F_0}{4\pi^2\,\epsilon_x\epsilon_y}\,. \tag{3.16}$$

In this context, B represents the source brilliance, $F_0$ is the total incoming flux, and $\epsilon_x$ and $\epsilon_y$ represents the emittances in the horizontal and vertical beam directions, respectively [33].

Hence, improving the incoming coherent flux, $F_c$, is one of the basic approaches to enhancing the signal-to-noise ratio (SNR). However, in the case that the sample is susceptible to radiation, this approach may result in degradation or breakdown of the system as a consequence of exceeding the critical threshold dose ($D_c$) [83, 80]. In order to use the enhanced coherent flux for Bio-XPCS investigations, the experimental configuration requires improvements in the areas of focusing, photon energy, the creation of a high-frequency shutter, and an extended sample-to-detector distance.

# Chapter 4

# Data processing and analysis

The following chapter involves an overview of the analysis of the X-ray scattering data. The subsequent sections detail the procedures for data collection, the preparation of raw data for analysis, and the identification of outliers. The Python software package Xana, developed by Mario Reiser, was utilized to extract the SAXS and USAXS scattering intensities as well as to compose 1D and 2D correlation functions from speckle patterns in the data. Additional analysis was conducted using MATLAB.

## 4.1 The XPCS data collection process

A typical X-ray Photon Correlation Spectroscopy (XPCS) experiment involves the acquisition of a sequence of scattering patterns that are consecutively captured over time at a single sample position. Modern X-ray facilities, such as X-ray free-electron lasers (XFEL) and Synchrotrons, exhibit enhanced brilliance and fast repetition rates. Consequently, the quantity of data collected during one week of beamtime can quietly accumulate to hundreds of terabytes. The PETRA III facility, where these experiments were conducted, demonstrates high data acquisition rates, resulting in the generation of millions of images. The real-time processing and analysis of this data remain a significant challenge to the existing file system and computational capabilities. Therefore, the transfer of data to the host computer's storage device for analytical purposes is almost impossible. The only possible way to access and analyze the data during and after beamtime is online.
The amount of data acquired by an XPCS experiment depends primarily on several key parameters, including the number of recorded scattering patterns, the delay time between the scattering patterns, and the exposure time. The number of collected scattering

patterns in the SAXS-XPCS method usually ranges from 600 to 1000, and for the USAXS-XPCS method, it ranges from 1000 to 5000. Typically, the duration of exposure time was set between 5 and 100 milliseconds. In some cases, the duration of exposure time was defined as 10 milliseconds. The estimated dynamics of the sample determined the delay time between the scattering patterns. Therefore, the duration of the delay time in this work was systematically modified within the range of 0 to 0.5 seconds and maintained constant throughout every XPCS run. The introduction of such a delay time by using a shutter helps to prevent beam damage. The XPCS experiment was conducted in different operational modes, namely continuous or frame modes, depending on the delay time. Under the "continuous mode" setup, the delay parameter is set to 0 and the beam shutter remains open throughout the entire duration of the run. However, in the data processing, a delay of 1 $\mu s$ between scattering patterns must be taken into account due to the detector's dead read-out time. In frame mode, if the delay time is not equal to zero, the shutter remains closed for the duration of the delay time and is then opened during the exposure time.

### 4.1.1 Raw data preparation

The Eiger 4M detector captures a series of unprocessed X-ray diffraction images that include diffraction from the protein sample as well as diffraction originating from the experimental arrangement. The Eiger 4M detector is made up of eight individual detector modules. The Xana software package in Python is utilized for loading and preprocessing data in preparation for subsequent analysis. The 2D scattering patterns obtained from the IgG model system during an XPCS measurement was recorded in the SAXS setup and are illustrated in Figure 4.1. and 4.2.

In the SAXS configuration, the detector records a time series of coherent diffraction patterns throughout a q range of $0.03\,\mathrm{nm}^{-1} \leq q \leq 1\,\mathrm{nm}^{-1}$ in the USXAS setup, the q range is $0.003\,\mathrm{nm}^{-1} \leq q \leq 0.05\,\mathrm{nm}^{-1}$. The region of the beam center is covered by the beamstop until reaching magnitudes that correspond to a scattering vector of q = 0.03 $\mathrm{nm}^{-1}$ for the SAXS setup and 0.003 $\mathrm{nm}^{-1}$ for the USAXS setup, as depicted in Figure 4.2.
Prior to analyzing the unprocessed data, it is necessary to establish a baseline of zero for the detector region, which records signals coming from other sources than the scattering of the protein sample. Therefore, a mask is generated with the purpose of removing the

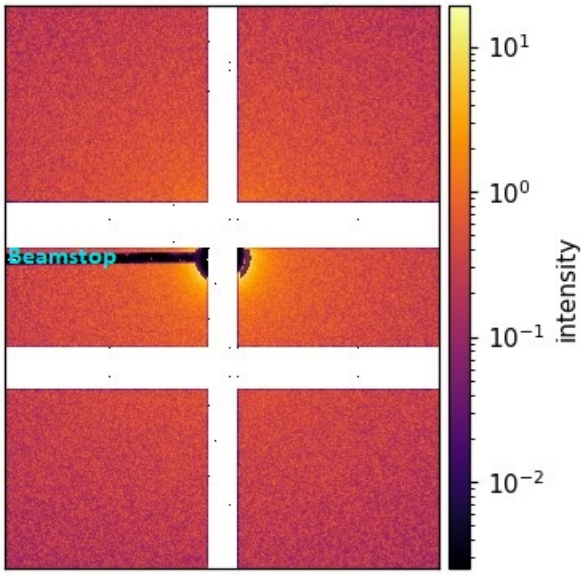


Figure 4.1: The Eiger 4M detector was employed to capture the scattering pattern recorded in the SAXS configuration. This image depicts the mean value derived from six hundred individual exposures, each with a duration of 0.1 seconds.

signal coming from the beamstop, the gap between the detector modules, and any parasitic scattering. Furthermore, the detector exhibits specific hot pixels that have been properly masked. The scattering pattern obtained through the use of the mask is presented in Figure 4.2.

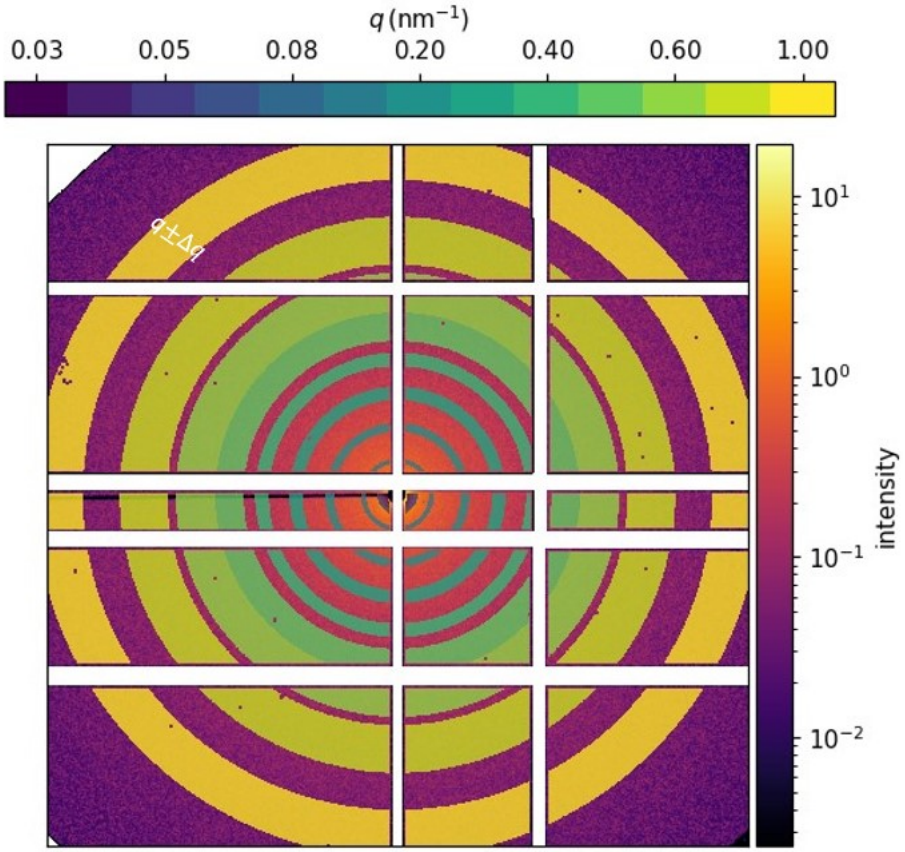


Figure 4.2: The scattering pattern is observed after defining the scattering vector ($q \pm \Delta q$) in the range of $0.03\,\mathrm{nm}^{-1} \leq q \leq 1\,\mathrm{nm}^{-1}$ and applying the mask.

## 4.2 Composing 1D and 2D correlation functions from speckle patterns

The Xana module in Python is used for the purpose of constructing one and two dimensional correlation functions from speckle patterns, as well as for the analysis of large amounts of X-ray scattering data. The software offers methods for applying SAXS-XPCS and USAXS-XPCS analysis schemes, such as the computation of correlation functions and azimuthal integration. Xana uses algorithms to parallelize both data access and analysis processes, which reduces computation time [99]. This feature is particularly significant for online data analysis during beamtime. The use of data chunking enables the execution of code on devices with limited memory capacity, such as laptops. Xana's primary characteristic is its database, which archives the outcomes and includes metadata linked

to the datasets and analysis. Thus, it enables us to easily search, find, and combine outcomes. In addition, it includes techniques for data filtering and averaging, along with algorithms for estimating parameters and fitting models with multiple exponential components [99].

In protein solutions and other disordered samples, dynamics cause fluctuations in speckles. By collecting time series of speckle patterns and generating intensity autocorrelation functions, XPCS is able to quantify these fluctuations. Each XPCS time series was measured at a distinct sample position due to radiation sensitivity. Consequently, the analysis of time-resolved 2D speckle patterns obtained from XPCS measurement involves the usage of a two-time correlation function (TTC) C(q, $t_1, t_2$) [9]

$$C(q, t_1, t_2) = \frac{\langle I_p(q, t_1) I_p(q, t_2) \rangle_q}{\langle I_p(q, t_1) \rangle \langle I_p(q, t_2) \rangle_q} \tag{4.1}$$

where $I_p$ represents the intensity value at a given pixel $p$ [49, 89]. The symbol $\langle .... \rangle$ denotes the average computed over a range of q-values ($q \pm \Delta q$), as used in the present study. The variables $t_1$ and $t_2$ correspond to different experimental time. The selection of the number of images per series $N_{img}$ and frame time $t_f$ was made to ensure that the correlation functions involve the complete spectrum of temporal scales, ranging from tens of microseconds to hundreds of seconds.

Given that correlation functions are typically calculated on a logarithmic time scale, it is intuitive to compute the data points using logarithmic spacing. A so-called multi-tau correlator classifies this by binning images along the time axis. Thereby, the number of data points is reduced, which increases the signal-to-noise ratio. If the last bin does not have enough data points, the correlation functions may be suddenly cut off as a side effect of logarithmic binning [99]. Figure 4.3 displays the typical outcomes of the TTC approach corresponding to the obtained data. The stability of the diagonal's width over 500 s indicates that the phase-separated IgG+PEG systems have an equilibrium dynamics. The chapter at hand does not go further into the physical phenomena that underlie TTC features, as this topic will be expounded upon extensively in Chapter 5.

The constant width of the diagonal in Figure 4.3 indicates equilibrium dynamics. Therefore the extraction of $g^{(2)}(t)$ functions that measure dynamics from a specific moment during the measurement can be achieved through cuts made on the two-time correlation function, which are perpendicular to the diagonal [89, 97]. Figure 4.4 demonstrates the usual results of the $g^{(2)}(t)$ approach at different q-values derived from the collected data.

The $g^{(2)}(t)$ cuts have varying lengths due to the slightly varied starting times on the

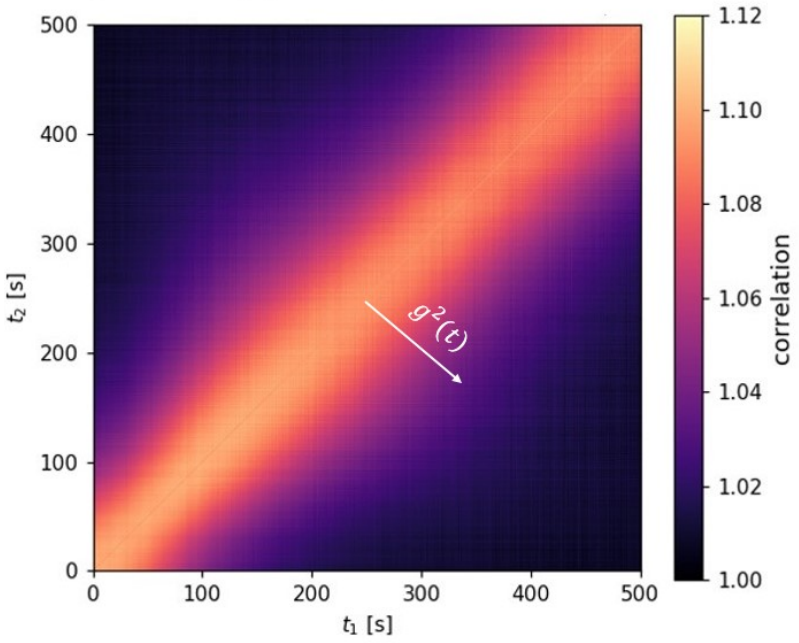


Figure 4.3: The measured TTC over 500 s demonstrates that the primary relaxation along the diagonal exhibits almost constant behavior. This indicates that, in this case, the phase-separated IgG+PEG systems have equilibrium dynamics throughout the duration of the measurement.

diagonal of the TTC. The problem of averaging over nan-type values is solved by shortening the longer $g^{(2)}(t)$ s to the dimension of the cut with the fewest data points, yielding a parallelogram-shaped section of the TTC. The Kohlrausch-Williams-Watts (KWW) relation can be applied to fit $g^{(2)}(t)$ functions, thereby enabling the determination of the characteristic relaxation time ($\tau$) as well as the shape parameter ($\gamma$) as a function of q and t.

$$g^{(2)}(q,\tau) = 1 + \beta(q)\, e^{(-2\Gamma(q)\tau)^{\gamma}} \tag{4.2}$$

where $\Gamma(q)$ is the decay rate, $\beta(q)$ is the q-dependent speckle contrast, and $\gamma$ is the KWW exponent that determines the type of motion [83]. The chapter at hand does not go further into the physical phenomena that underlie $g^{(2)}(t)$ features, as this topic will be expounded upon extensively in Chapter 5.

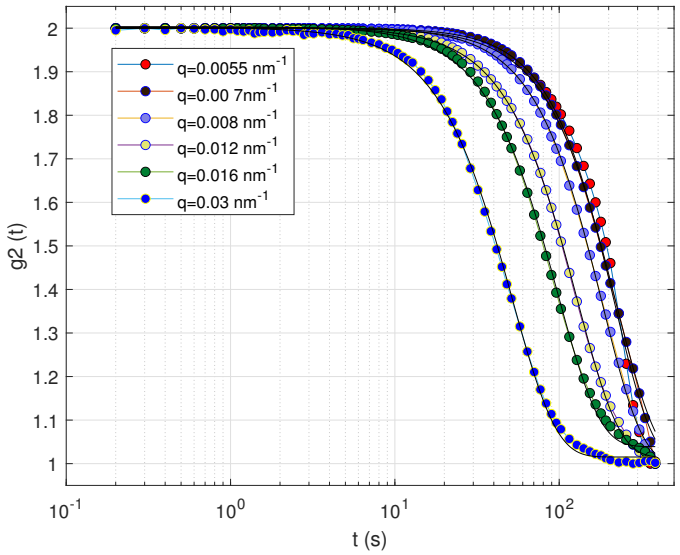


Figure 4.4: Typical correlation function $g^{(2)}(t)$ at different q-values derived through diagonal TTC cuts.

## 4.3 The identification of Outliers

Scanning capillaries containing protein samples with an X-ray beam may result in the formation of bubbles or aggregation. Additionally, spatially heterogeneous dynamics may arise due to effects such as sedimentation [19]. Hence, it is important to detect artifacts and quantify measurements that exhibit indications of beam-induced effects for the purpose of data analysis. The data presented in Figure 4.5 a and b exhibit different two-time correlations that show significant heterogeneity throughout the measurements. This phenomenon is not limited to the IgG+PEG sample but is also visible in other samples, including egg white, BSA-$YCl_3$ and metallic glasses [97, 26].

The typical TTC displays three distinct attributes, namely, modulation along the diagonal, a square-shaped feature, and a tail. Initially, the modulation, which is usually the most significant aspect to look at when using XPCS to study dynamics, is related to the growth of the domains, where the rate of growth slows down over time. The square-like appearance of the TTC is the result of rapid changes in shape and concentration distribution, as well as a transition from the rapid growth of domains in the early stage to their subsequent gradual dissolution. The observed phenomenon can be related to the shift in size and average interparticle distance, leading to a displacement in the scattering intensity I(q) [39, 97].

The correlation maps recorded from different points of the capillary display a clear trend in which the correlation function slowly decreases at the bottom of the capillary, whereas near the capillary's midpoint, the loss of correlation shows a sudden decrease or increase. This can be observed, particularly when the Linkam stage is heating or cooling. Probably, a temperature gradient within the sample is causing flow within the sample. The loss of correlation can be explained by avalanche events resulting from elastic rearrangements within the sample. In order to accurately reduce this problem, the measurements were simply conducted in a position where scattering have not exhibited anisotropy.

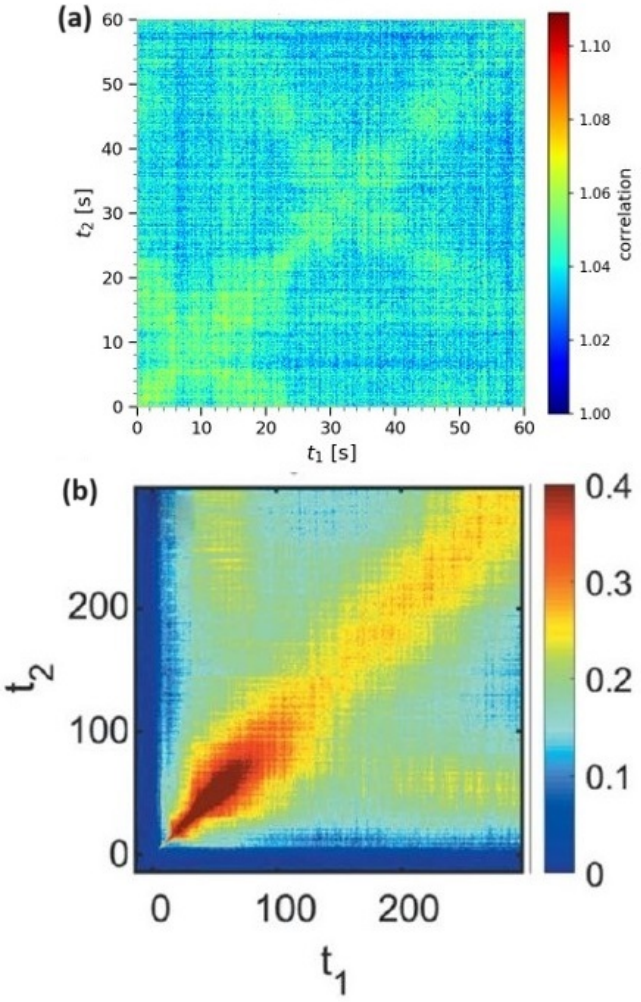


Figure 4.5: Two-time correlation functions of (a) IgG+PEG and (b) BSA shows a significant heterogeneity throughout the measurements [97].

### 4.3.1 Sorting data

In the USXAS-XPCS setup, it is possible to compute the intensity autocorrelation function $g^{(2)}(t)$ from a single measurement and acquire dynamics information. However, in the SAXS-XPCS configuration, the main problem is that the scattering intensity at large q values decreases by four orders of magnitude in comparison with the intensity of the q values observed in the USAXS measurements. Therefore, it was not possible to extract a correlation function suitable for analysis from a single X-ray scattering series. In order to achieve an appropriate signal-to-noise ratio, the number of repetitions ($N_{rep}$) was increased, and the correlation functions of several series were merged together. This approach allowed us to obtain a more reliable statistical average, which was subsequently used to determine an appropriate $g^{(2)}(t)$.

Undesirable data are frequently observed in datasets due to impurities in the sample, bubble formation, aggregation, and beam-induced damage, as previously mentioned. Consequently, the use of sorting methods enables the identification and elimination of outliers data points from a given dataset. The outlier correlation function of 230 correlation functions, $g^{(2)}(t)$, is shown in Figure 4.6 (a). The measurements were conducted with an exposure time of 4 seconds and a corresponding q value of 0.04 nm.

To identify outliers in the correlation function, all correlation functions were plotted. So, an outlier correlation function is identified when its value differs significantly from the mean value of correlation functions, as illustrated in Figure 4.6(a). They may deviate significantly more from the actual correlation function and cause considerable average deviations. Hence, it is essential to carefully address even a small number of outlier datasets. For the given dataset, at q = 0.04 $nm^{-1}$, only one correlation function from 230 was recognized as an outlier. However, the number of outliers will rise with higher q values because of the low SNR at those levels, and the tail feature rises earlier for higher q values [97]. Consequently, after reducing the outliers from the dataset, the final correlation function, which is denoted by the blue line in Figure 4.6 (a, b), will be the combination of all remaining correlation functions.

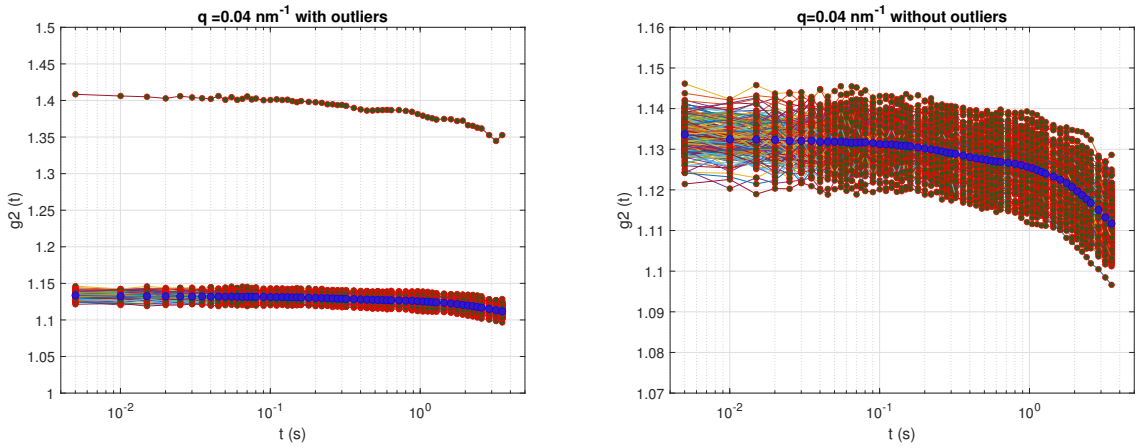


(a) (b)

Figure 4.6: Data processing to find outliers (a) presented an outlier correlation function among the correlation functions, and an outlier have a value far from the mean value of correlation functions. (b) After removing the outlier correlation from the dataset.

### 4.3.2 Combination of two correlation functions

It is clear that individual correlation functions that cover a range of time from the smallest delay time of ms to hundreds of seconds and more can be used to make complete correlation functions. A correlation function will be obtained for each exposure time; however, it may not be suitable for analysis. To achieve a nearly comprehensive $g^{(2)}(t)$ function across multiple orders of magnitude in time, data was collected through a two-step process. Initially, measurements were taken over a total duration of 4 seconds at a high frame rate and a short exposure time. Subsequently, measurements were taken over a duration of 300 seconds at a lower frame rate, with a time delay between each frame achieved through the use of a shutter. The problem at hand refers to the absence of a baseline for short-time measurements, specifically those running for 4 seconds. This is due to the fact that the correlation does not decrease to zero, instead, it exhibits a decay in between, thereby preventing accurate fitting. In order to solve this issue, the correlation functions are stitched across both temporal scales.

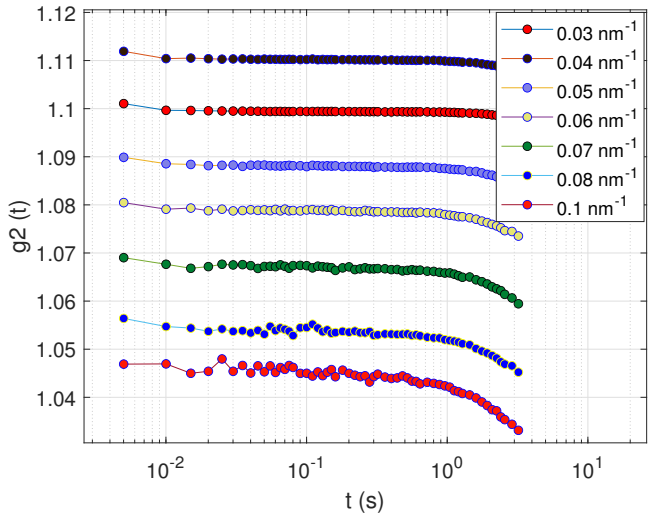


(a)

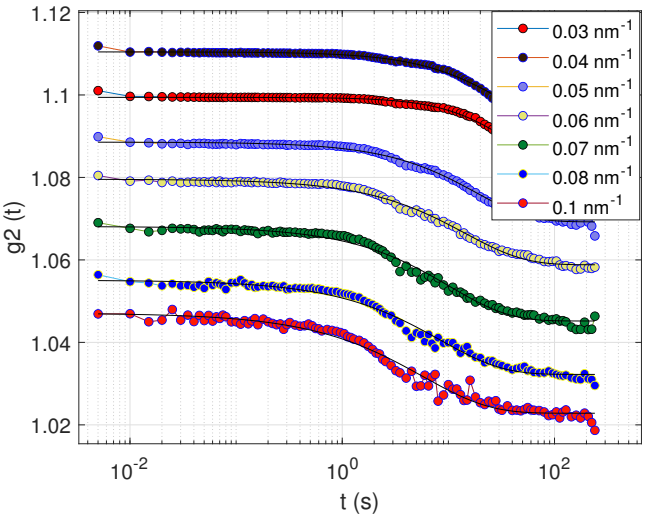


(b)

Figure 4.7: The combined effect of two correlation functions: (a) a 4-second measurement at a high frame rate and a short exposure time; (b) the correlation functions were stitched together in both time scales of 4 seconds and 300 seconds.

# Chapter 5

# Data Discussions and Conclusions

The most important findings from this study will be described in the following sections. Section 5.1 will start with a discussion of the results, mainly the SAXS-XPCS data of quenched IgG+PEG and BSA at large q values to obtain dynamical information of protein solutions. In Section 5.2, we describe the influence of different doses and dose rates on the dynamics of protein solutions. Finally, Section 5.3 will demonstrate conclusion and the possibility of using Bio-XPCS techniques for the purpose of investigating protein dynamics.

## 5.1 SAXS analysis of large q-value data

It is possible to obtain information about microscopic and macroscopic features, including viscosity, movement, aggregation, stability, and protein interactions, by studying the molecular diffusion of protein solutions. Proteins exhibit complex movements at the nanoscale in terms of both time and length [43]. On short time scales, the protein molecule undergoes diffusion in the cage of the surrounding molecules, exhibiting both translational and rotational displacements. In Y-shaped antibodies like IgG, the domain dynamics, or the way the lobes move relative to each other, is a prominent motif [38]. Unfortunately, the existing literature lacks comprehensive information regarding out-of-cage diffusion on longer intervals ranging from micro- to millisecond timescales. X-ray photon correlation spectroscopy (XPCS) is the only experimental approach capable of investigating the diffusion of proteins, considering their characteristic length scale of approximately a few nanometers [20, 33]. This limitation needs to be revised when studying proteins within a naturally crowded environment, such as the cytoplasm, or when their concentration

is exceptionally high. One instance illustrating this natural occurrence is the protein known as crystal, which is found within the lenses of the eye [33, 11]. When the protein concentration is increased, it is possible for the solution to undergo a glass or gel transition, resulting in a subsequent reduction in the diffusion coefficient [38, 39, 97].
In order to obtain a comprehensive understanding of the molecular factors, this study aims to investigate the molecular-level dynamics of protein solutions. This study employs a protein-polymer model system to investigate the dynamic behavior of almost at the length scale q $\cong$ 1 $nm^{-1}$ within a crowded environment using X-ray scattering techniques. The process of quenching the temperature of protein solutions from ambient conditions to a significantly lower temperature, close to the freeze point, causes a transformation from a uniformly dispersed solution to a system that is separated into distinct phases and is unable to undergo further macroscopic changes. Due to the occurrence of an arrested phase separation in this system, the investigation of its dynamics is not simple to perform. The dynamics of the proteins were investigated while the system was undergoing LLPS and at low temperatures (Tq = 6 °C and -5 °C), when the phase separation is delayed to the point that domain growth is almost totally arrested. The system was evaluated at various temperatures and photon fluxes.

### 5.1.1 SAXS analysis of the quenched IgG+PEG model system

The IgG model system was quenched to a temperature of Tq = 6 °C, and the measurements were initiated after a waiting time of $t_w$ = 10 minutes to ensure that the system had reached the arrested state. Every measurement has been recorded at a new sampled spot. Proteins are expected to show a temporary sub-diffusion time for a specific time range known as the interaction time ($\tau_i$). This time interval is defined as the duration it takes for a particle to traverse a distance equivalent to its radius ($R_p$), which can be calculated using the formula $\tau_i = R_p^2/D_0$ [106, 53, 38]. Here, $R_p$ represents the protein's radius, while $D_0$ represents the short-time diffusion coefficient With the given parameters of $R_p = 5.5\,nm$ and the diffusion coefficient in the one-phase region obtained by [38] $D_0 = 0.3\ Å^2\,ns^{-1}$, the resulting value of $\tau_i \sim 9\ \mu s$. In order to obtain a comprehensive understanding of protein diffusion, it is essential to observe diffusion over extended periods of time, exceeding the temporal scale of $\tau_i$. In order to acquire correlation functions spanning a wide range of time scales, measurements were conducted with a cumulative measurement duration of 4 and 300 seconds.
Several challenges were encountered in extracting accurate dynamic information from the

correlation functions. One issue arises when conducting short-time measurements (e.g., 4 seconds) due to the absence of a baseline. This absence is attributed to the correlation not reaching zero but rather exhibiting a decay in between. Consequently, this limitation prevents the ability to achieve an accurate fitting. Therefore, to avoid this issue, the obtained correlation functions at different time scales were combined. Another problem arises at q values greater than 0.1 $nm^{-1}$, where the decorrelation starts within a time frame of less than 10 milliseconds. The measured correlation with the existing setup does not display the upper baseline of the correlation function, which poses challenges in accurately fitting the data and extracting dynamic information at large q-values. Consequently, a theoretical difference [83] was determined based on the q value and the setup parameter and subsequently used to fit the correlation functions.
The experiment successfully demonstrated the possibility of achieving a high SNR for the measurement of correlation functions up to a wave vector value of q = 1 $nm^{-1}$, which is comparable to the length scale of individual proteins. Figure 5.1 displays the merged correlation functions up to a wavevector of q = 1 $nm^{-1}$. The calculation of the dynamical parameter can be achieved by using Equation 4.2. Figure 5.2 displays the decay rate $\Gamma$, and shape component KWW as a function of q at different temperatures.

On the nanometer-length scale, a subquadratic ratio was determined between the decay rates $\Gamma$, and q. Therefore, Brownian motion does not govern the dynamics on the scale of single proteins. Similar anomalous mechanisms of diffusion in supercooled metallic liquids were discovered by Ruta et al [131, 102]. Although the dynamics are arrested by the length scale of protein droplets at these quenched temperatures [39, 97], here it is observed that at large q-values where $q > 0.1\,nm^{-1}$, the decorrelation times are shorter than 1 sec. Cluster fluctuations within protein-rich domains can explain this dynamic process. The calculated correlation functions at large q values exhibit stretched KWW exponents of 0.5, which suggests the presence of significantly heterogeneous dynamics [37]. At $T_q$= -5 °C, the shape of the KWW exponent transforms from compressed (KWW > 1) to stretched (KWW < 1).

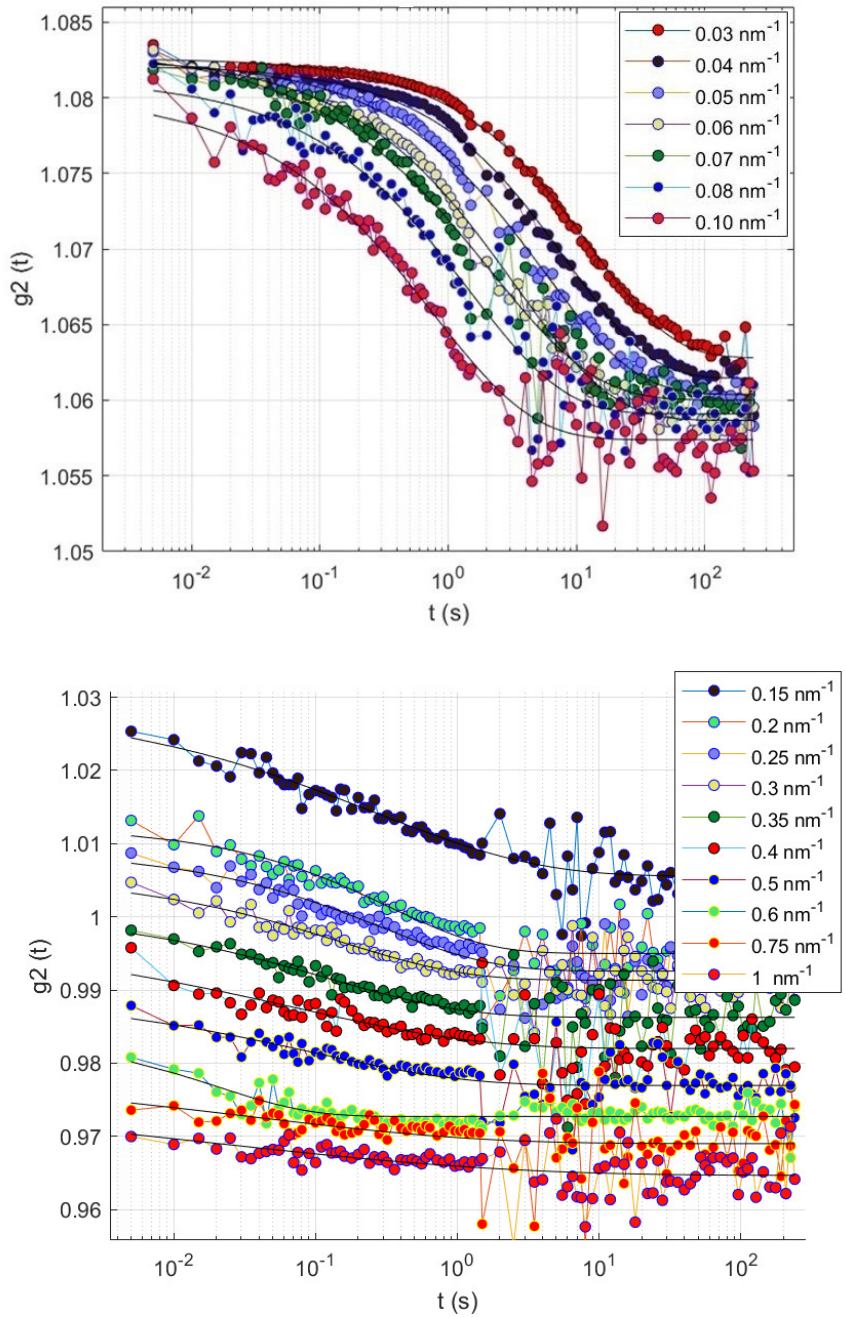


Figure 5.1: The correlation functions for the IgG protein sample after quenching the system from T = 37 °C to $T_q$ = 6 °C in the q-range of 0.03 $nm^{-1}$ to 1 $nm^{-1}$ and the fit is displayed in the black line. The correlation functions were stitched together in both time scales of 4 s and 300 s.

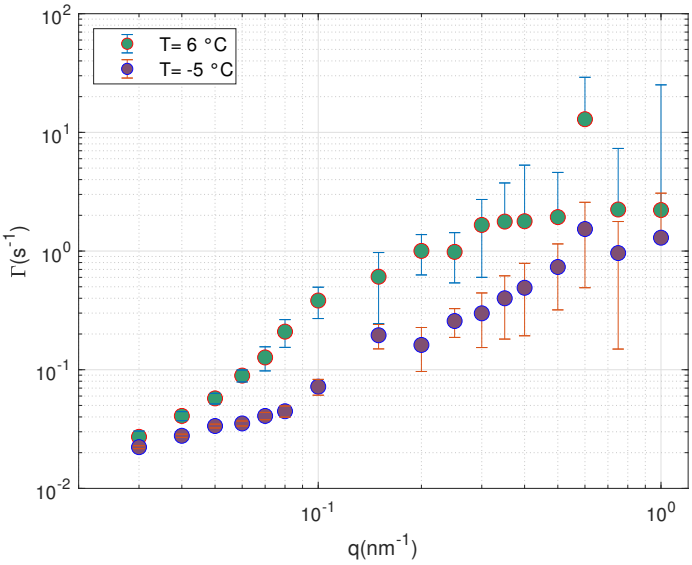


(a)

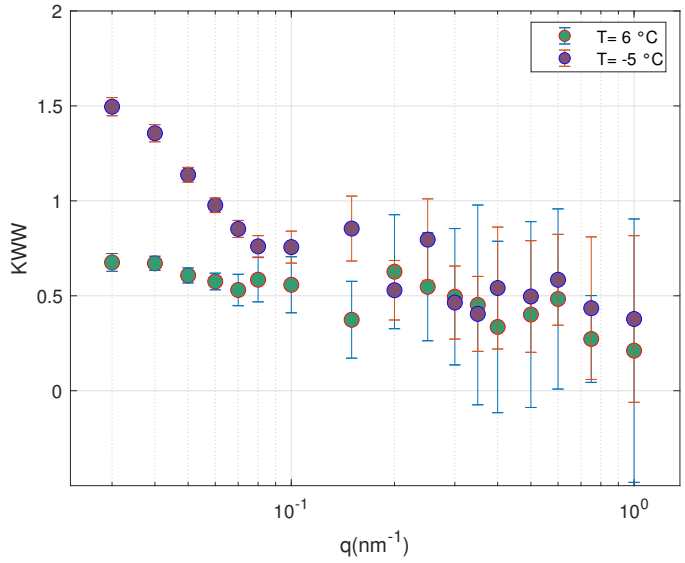


(b)

Figure 5.2: (a) Temperature and q dependence of the decay rats Γ at all q-values, but the KWW exponent does not follow these dependencies at large q-values. (b) At $T_q$ = 6 °C and -5 °C, the (KWW) exponents changes from a compressed (KWW > 1) to a stretched shape (KWW < 1).

## 5.2 Discussion

The study successfully demonstrated the practicality of achieving a satisfactory signal-to-noise ratio (SNR) for the computation of correlation functions up to q = 1 $nm^{-1}$, which corresponds to the length scale of individual proteins. The signal-to-noise ratio (SNR) in the above setup increases with an increasing number of measurement repetitions, as illustrated in Figure 5.12 for different q-values. Generally, an SNR of 1 or above is considered appropriate for fundamental measurements since it indicates that the signal strength exceeds the level of the noise. Whereas, an uncertainty regarding the feasibility of constructing a comprehensive and analyzable correlation function by combining multiple correlation functions that span different time intervals will be arise due to the possible influence of the beam. It is essential for all components of the correlation functions to be measured under identical photon fluences.

This study represents the first achievement in conducting a successful SAXS-XPCS experiment designed for exploring the dynamics of proteins at nanometer-length scales. The correlation function was measured at various temperatures, demonstrating a temperature dependence. However, it has been observed that varying measurements and beam times have brought to light a discrepancy in the results obtained from the same sample and experimental setup when different photon fluxes are used. It indicates that the beam had an effect on the dynamic information of the collected data during the SAXS configuration measurements. Therefore, this finding shows that we were unable to record unaffected dynamic information at these length scales.

Even though we have extensively investigated various time and length scales, our curiosity regarding the specific type of diffusion at large q values in the state of arrested phase separation remains unanswered. The restriction on the magnitude of beam damage within the SAXS range remains in the outcome. One potential solution to address this issue involves modifying the setup configuration by using a fast shutter and increasing the distance between the sample and the detector. This adjustment aims to enhance the contrast, thereby resulting in an improved signal-to-noise ratio.

In the subsequent section, our objective is to characterize the effects of the beam and determine the specific type of dynamics that are induced on the sample. Our primary emphasis lies in the study and assessment of the dynamic changes that arise as a consequence of the interaction between the beam and sample in the SAXS and USAXS configurations.

## 5.3 Beam-induced effects on protein solutions

In recent years, there has been a growing understanding of the enormous use of powerful X-ray sources such as synchrotrons and free-electron lasers in the investigation of the microscopic properties of materials.The findings of these studies have demonstrated that the X-ray beam can, in fact, induce chemical modifications in soft materials such as biological samples and polymers [103, 20, 35]. Nevertheless, an in-depth understanding of how the beam influences the characteristics of the sample is necessary for accurately interpreting these investigations. Unfortunately, there is currently not sufficient of research in this area, particularly in relation to powerful X-rays [103]. The high brilliance of a third-generation synchrotron source results in an increased X-ray dose that penetrates within the sample, potentially leading to significant changes in the characteristics of the sample material. This issue is commonly referred to as radiation-induced damage. One of the primary obstacles experienced in conducting an XPCS experiment with protein samples is how to achieve accurate measurements with a high SNR while ensuring the integrity of the sample remains unharmed.
In order to assess the impact of the beam on the sample, it is necessary to categorize these effects into two separate categories: structural changes and dynamic modifications. Indirect effects occur when X-rays interact with water molecules, resulting in the formation of hydroxyl and hydroperoxyl radicals. These radicals have the potential to bind to proteins. In contrast, direct radiation damage refers directly to changes in the molecular structure [125, 105]. The first category refers to changes in intensity as a function of dose, whereas the second refers to changes in dynamics caused by the beam and can be measured through changes in correlation functions. The origins of these entities may differ, and changes in dose levels and dose rates might result in different kinds of damage [74, 106]. Therefore, it is possible in principle to see two different effects resulting from the use of synchrotron radiation: beam effects on the structure and beam effects on the dynamics.

### 5.3.1 Beam effects on the structure

To achieve a high SNR, it is essential to have a high intensity of X-rays. The ionizing effect of the radiation may change the structure of the system or even cause total damage [35, 103]. In order to assess the impact of structural changes on the sample, the intensity was observed at various exposure times, representing varying levels of accumulated doses

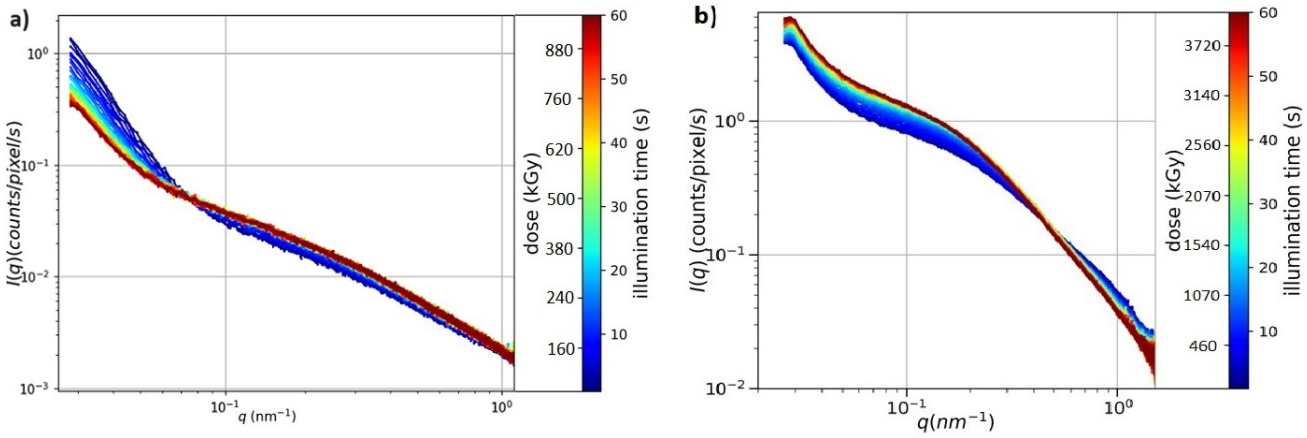


Figure 5.3: The SAXS-XPCS setup was used to record the scattering intensity at various times of illumination after a quench to a) 6 °C b) 37 °C. Changes in the intensity of X-ray scattering as a function of time and doses are visible.

on the sample. The intensity profile after a quench to 6 °C exhibits variations in response to changes in dose, specifically, for values of $q < 0.1\,\mathrm{nm}^{-1}$, a drop in intensity is observed, whereas for values of $q > 0.1\,\mathrm{nm}^{-1}$, an increase in intensity appears, as illustrated in Figure 5.3 a. In contrast, Figure 5.2 b depicts the scattering intensity profile obtained under constant temperature conditions (T = 37 °C) when the sample is in a homogeneous phase. An observed feature is the increase in intensity at low q values and the subsequent decrease in intensity at large q values as a function of dose. The observed shift in intensity at lower q values can be caused by radiation damage resulting from the protein aggregation [64, 39].

The variations in intensity observed at $q < 0.1\,\mathrm{nm}^{-1}$ reveals the formation of X-ray-induced protein aggregation. These variations can also be attributed only to modifications in the structure factor or a reduction in protein domain size, indicating the occurrence of aggregation or protein fragmentation [100, 130, 115]. Nevertheless, it is unclear that aggregation is the main basis for this decrease, as it would instead lead to an increase in intensity. The phenomenon of intensity reduction at varying dose rates on the structure is similarly found in a lipid membrane system. The damage results in the widening of higher-order lamellar reflections and a decrease in intensity [100, 103, 64]. Changes in the structure may be caused by radicals generated in the solvent, which may affect the surface charge of the proteins as a result of their interaction with proteins via ionization and subsequent ability to fragment and crosslink proteins [125, 130].

### 5.3.2 Beam effects on the dynamics

The understanding of cellular mechanisms depends extensively on the study of protein diffusion taking place at length scales comparable to their own size[20]. X-ray photon correlation spectroscopy (XPCS) currently represents the only technique available for investigating long-term collective diffusion at these specific length scales [83, 20]. However, its applicability in biological systems is currently constrained due to radiation-induced damage. In this study, we employ a new approach using XPCS for the purpose of investigating the impact of dose and dose rate on the dynamic behavior of protein solutions, specifically Immunoglobulin G (IgG) and Bovine Serum Albumin (BSA).
It has been previously discovered that the X-ray beam has the effect of fluidizing the material and inducing localized changes [92, 103]. The mentioned effect has been observed in protein solutions, specifically $\alpha$-crystallin [20], as well as in metallic glasses such as $SiO_2$. As shown in Figure 5.4a, the auto-correlation functions show that the incoming X-ray flux causes the atomic motion in the $SiO_2$ sample. The relaxation time scale of this motion has an inverse relationship with the incoming photon flux [103].

### 5.3.3 X-ray induced dynamics at the SAXS-XPCS setup

The SAXS-XPCS experiments were conducted at the DESY P10 beam line. In this study, our objective was to investigate the impact of an X-ray beam on the dynamics of Immunoglobulin G (IgG) and Bovine Serum Albumin (BSA). Therefore, we conducted a comparative analysis of dynamical data obtained from various sample positions and incoming fluxes, which were adjusted by adding X-ray attenuators along the beam path. Table 3.4 displays the X-ray flux reduction achieved by using various attenuators constructed from silicon single crystals. The highest flux used on the sample for the focused beam was $8.04\times10^{10}$ ph $s^{-1}$.
The material's density fluctuations are closely related to the autocorrelation function $g^2(q,t)$, which reveals information about the material's relaxation dynamics [75]. Therefore, as depicted in Figure 5.4a, we tried to extract the normalized intensity autocorrelation function $g^2(q,t)$ of IgG-PEG at a quenching temperature of $T_q = 0$ °C and a wave-vector q = 0.1 $nm^{-1}$ for various photon fluxes. In order to provide a quantitative analysis of this finding, we used the Kohlrausch-Williams-Watts (KWW) expressions (Equation 4.2) to fit the curves. In this equation, the parameter KWW characterizes the shape of the curve, while $\tau$ represents the relaxation time. The relaxation exponent KWW indicates the characteristics of the dynamical process. It covers a range, with values of KWW $< 1$

corresponding to a stretched decay, KWW = 1 corresponding to a simple exponential decay, and KWW > 1 corresponding to a compressed function [31].
Figure 5.4 c,and d indicates that the dose rate influences both the shape parameter KWW and the average relaxation time $\langle\tau\rangle = (\frac{\tau}{KWW})\Gamma(\frac{1}{\tau})$ [102, 20], and increasing the dose rates leads to a decrease in the average relaxation time. It is obvious that the larger dose rates or fluxes result in faster dynamics and induce a shift from nearly stretched to compressed signatures at this q-value. This indicates that the dose rate, rather than the accumulated dose itself, is the most important factor in determining beam-inducing dynamics in XPCS measurements.

The observed susceptibility of the samples to modifications caused by radiation seems to be related with their physical state. The presence of X-ray-induced motion can be observed in the IgG+PEG sample at both quenched temperatures of 0 °C and 6 °C. Typically, the dynamics of the sample at $T_q$ = 6 °C are faster than at $T_q$ = 0 °C, as indicated at the lower flux, because the physical state of the IgG+PEG sample at $T_q$ = 0 °C is near the glass transition and demonstrates slower dynamics. Therefore, the data should exhibit a temperature dependence similar to the systems demonstrated at lower fluences in Figure 5.5. However, it is notable that the system deviates from this behavior at high fluences as a result of the structural changes that occur at $T_q$ = 6 °C.

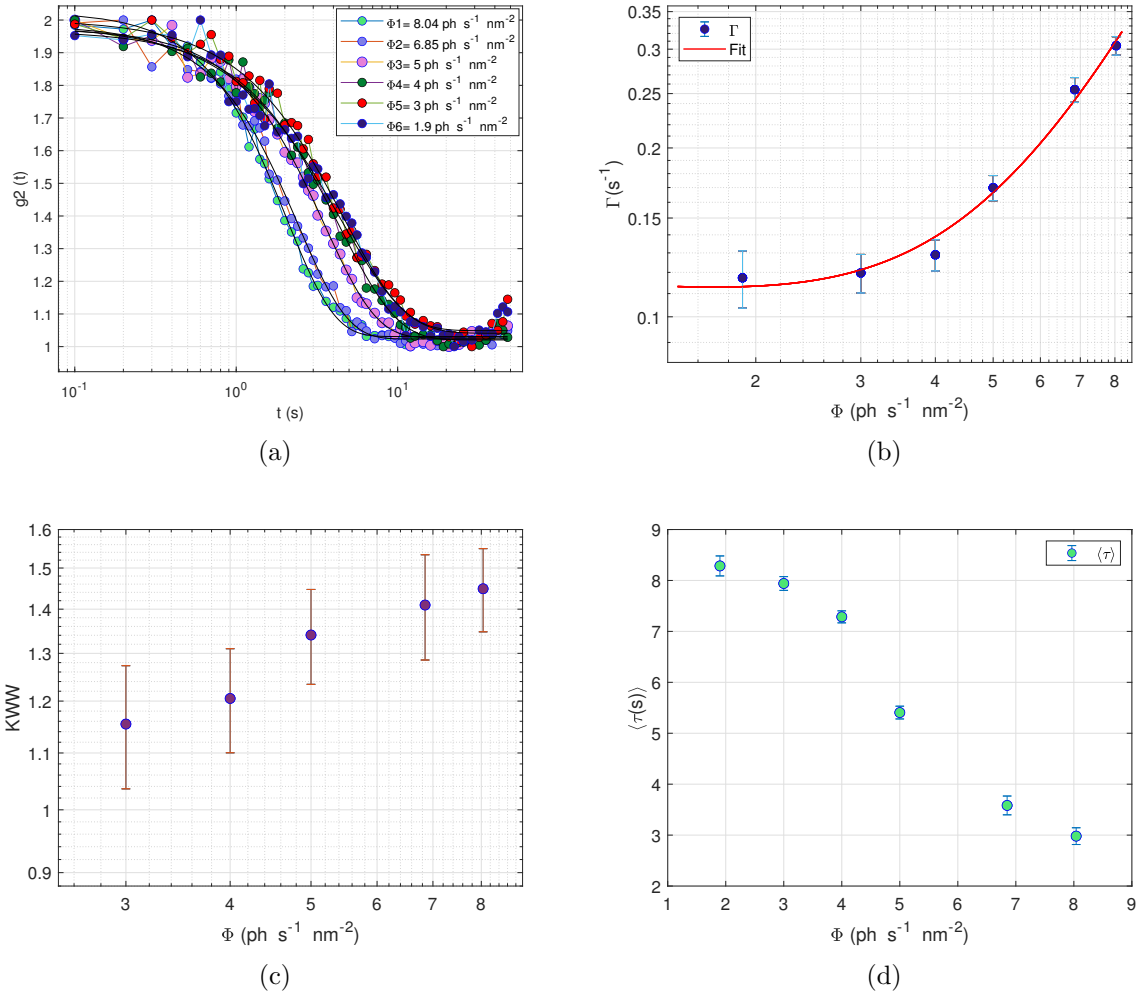


Figure 5.4: The intensity autocorrelation function $g^2(q,t)$ of IgG-PEG at a quenching temperature of $T_q = 0$ °C and a wave-vector q = 0.1 nm$^{-1}$ for various photon fluxes ($\Phi$) The incident x-ray beam thus fluidizes the sample and induces driven dynamics. Here we can observe that the average relaxation time decreases as a function of incident X-ray flux.

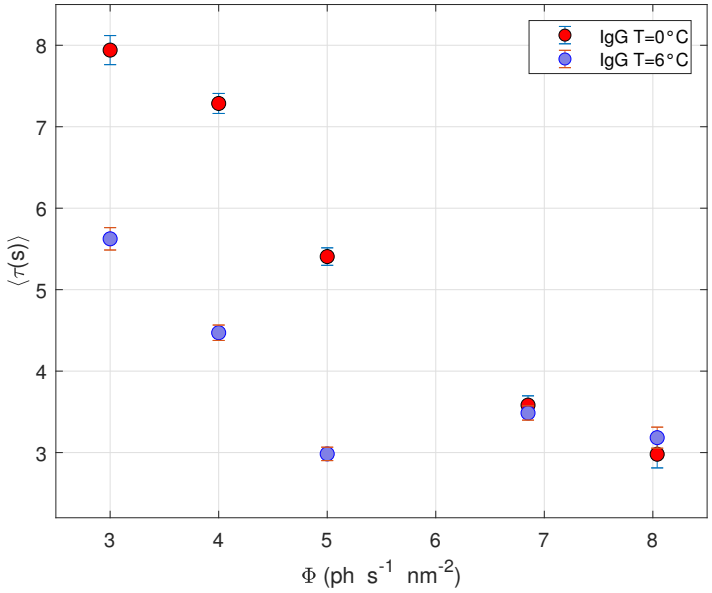


Figure 5.5: The susceptibility of the samples to radiation-induced changes appears to be related to their physical state. The higher flux at $T_q = 6$ °C has a greater impact on the sample due to its ability to induce structural changes more rapidly in this state.

### X-ray induced dynamics on BSA+$YCl_3$ system

To investigate the potential effect of the X-ray beam on the dynamic properties of a different protein solution, we used a solution consisting of Bovine Serum Albumin (BSA) and Yttrium trichloride ($YCl_3$). BSA is a type of globular protein that comes from cows and has a molecular weight of about 66 kDa. It is made up of 583 amino acid residues and has hydrodynamic measurements of 140 x 40 x 40 Å, which are similar to the shape of an ellipsoid. Albumin is a key part of controlling the pressure in the plasma. Because it has the same structure as human blood albumin (HSA), BSA has been studied a lot as a model protein. In comparison to the IgG+PEG system, which exhibits an upper critical solution temperature (UCST), the BSA+$YCl_3$ system demonstrates a lower critical solution temperature (LCST) [96]. The sample that had been used is described in more detail in section 3.1.2.

In this section, our primary emphasis was on investigating the impact of the dose rate on the system rather than the accumulated dose. Hence, a comparative analysis was performed on dynamical data acquired from different sample positions and incoming fluxes. The analysis was performed at a constant accumulated dose of 200 kGy. As displayed in Figure 5.6a, we tried to extract the normalized intensity autocorrelation

function $g^2(q,t)$ of the BSA+$YCl_3$ system at a quenching temperature of $T_q = 49$ °C and a wave-vector q = 0.04 $nm^{-1}$ for different photon fluxes. The decay rate is proportional to the incoming flux and rises in a linear fashion as the flux increases Figure 5.6b. As illustrated in Figure 5.6 d, and c, it can be observed that the dose rate has a significant effect on both the shape parameter KWW and the average relaxation time $\langle\tau\rangle$, even when the dose remains constant. Moreover, an increase in dose rates results in a decrease in the average relaxation time. With the exception of the initial point, the KWW or shape component exhibits an increase as a function of dose rate. In this context, the impact of the cumulative dose on dynamics is far less apparent.

### 5.3.4 X-ray induced dynamics at the USAXS-XPCS setup

The assumption is established that the beam-induced dynamics and intrinsic dynamics are two distinct and parallel relaxation processes [20]. This hypothesis serves as a basis for the need to account for the influence of dose rate in order to accurately determine the intrinsic dynamics of protein solutions. In the SAXS setup, in order to obtain a high SNR, it is necessary to have a high X-ray intensity, which causes rapid beam damage. Therefore, we conducted a USAXS-XPCS experiment at the DESY P10 beamline to avoid fast beam damage and to determine how to distinguish the beam-induced dynamics from intrinsic dynamics. Section 3.3 provides comprehensive information regarding the measurement parameters used in the USAXS-XPCS setup.

The effect of the X-ray beam on the sample's dynamics was measured by comparing the obtained dynamical properties at various dose rates. The control of photon fluence is achieved through the use of a silicon attenuator, with varying thicknesses of up to 25 $\mu$m. This attenuator is capable of being placed along the beam path, thus enabling the adjustment of X-ray fluence.

For the purpose of better understanding of the changes in diffusion resulting from the beam, the two-time correlation functions (TTC) were calculated using Equation 4.1. Figure 5.7 displays the calculated TTCs of IgG+PEG at different sample positions and incoming fluxes for scans with a maximum flux of 1.99 $\times 10^{10}$ ph $s^{-1}$ and a minimum flux of 0.04 $\times 10^{10}$ph $s^{-1}$. The decay rates in the TTCs exhibit a significant dose-rate dependence. To quantify this dose rate effect, $g^2(q,t)$ functions of the IgG+PEG system are extracted at a quenching temperature of $T_q = 0$ °C and a wave-vector q = 0.016 $nm^{-1}$ for different photon fluxes from these TTCs, which is illustrated in Figure 5.8a. The $g^2(q,t)$ functions similarly demonstrate significant dependence on fluence at high flux values. However, at

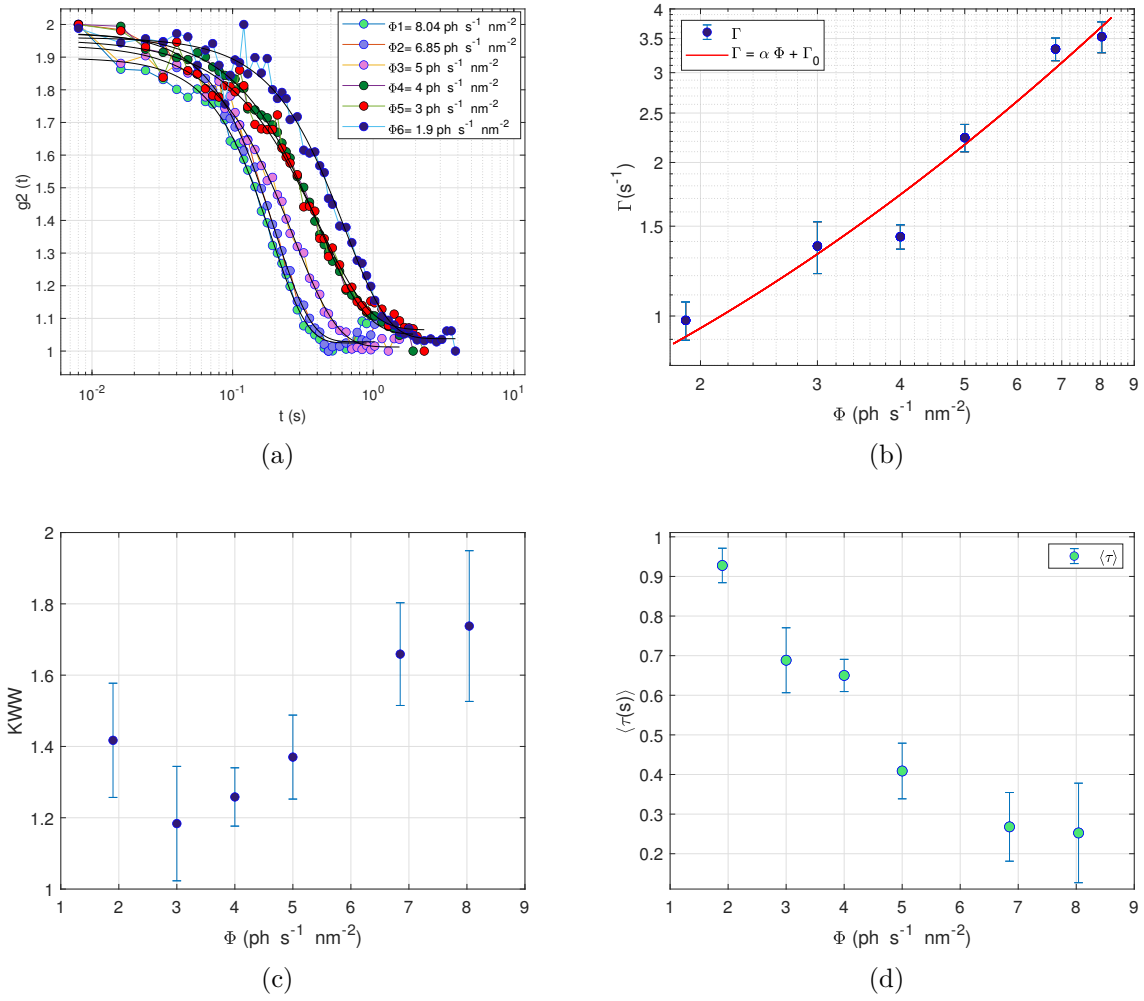


Figure 5.6: (a) The normalized intensity autocorrelation function $g^2(q,t)$ of the BSA+$YCl_3$ system at a quenching temperature of $T_q = 49$ °C and a wave-vector q = 0.04 $nm^{-1}$ for different photon fluxes (b) The decay rate increases linearly as the incoming flux increases. (c) and (d) Both the shape parameter KWW and the average relaxation time $\langle\tau\rangle$ affected by the beam, even when the dose remains constant.

lower flux levels, there is an observable overlap between the last two $g^2(q,t)$ functions, indicating that the beam does not induce dynamic effects on the sample at these flux levels. The data presented in Figure 5.8c demonstrates that the decay rate $\Gamma$ is influenced by the dose rate. Specifically, it is observed that the lower dose rate has a smaller effect on inducing driven motion compared to the higher dose rate.

The resulting values of the shape component KWW as a function of the dose rate are displayed in Figure 5.8b. In contrast to the SAXS data obtained at higher q-values, the KWW relaxation parameter exhibits a decrease with increasing dose rate. This implies that the beam can force the sample into a less compressed diffusion at these length scales. Therefore, under the influence of X-ray radiation, the data indicate that the dynamics of IgG+PEG system increasing as a function of dose rate.

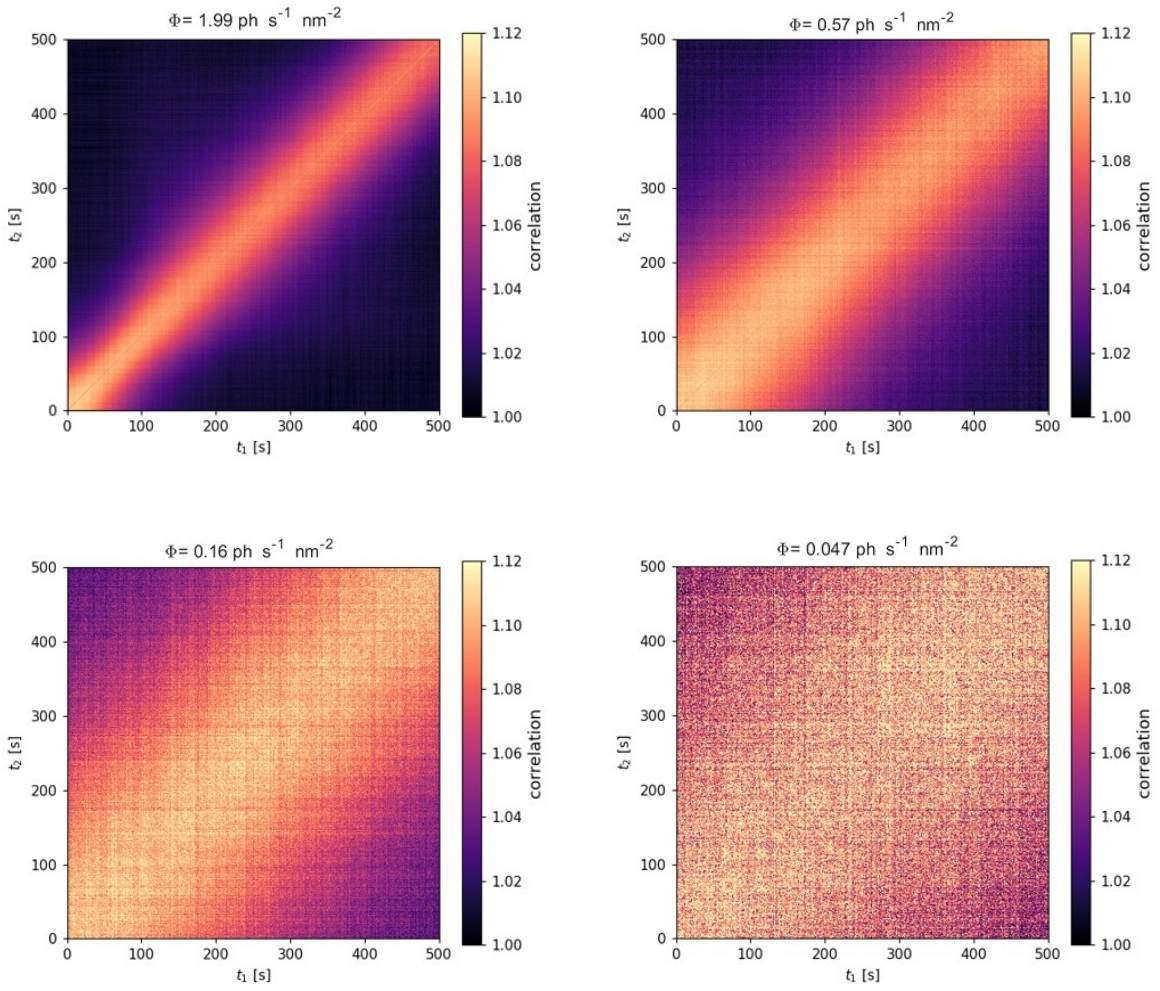


Figure 5.7: The TTC is derived from illuminating a single point on the sample capillary continuously at q= 0.016 nm$^{-1}$. By measuring the two-time correlation function TTC of IgG+PEG at different X-ray doses and dose rates, we can observe a pronounced dose rate dependence of the relaxation rate.

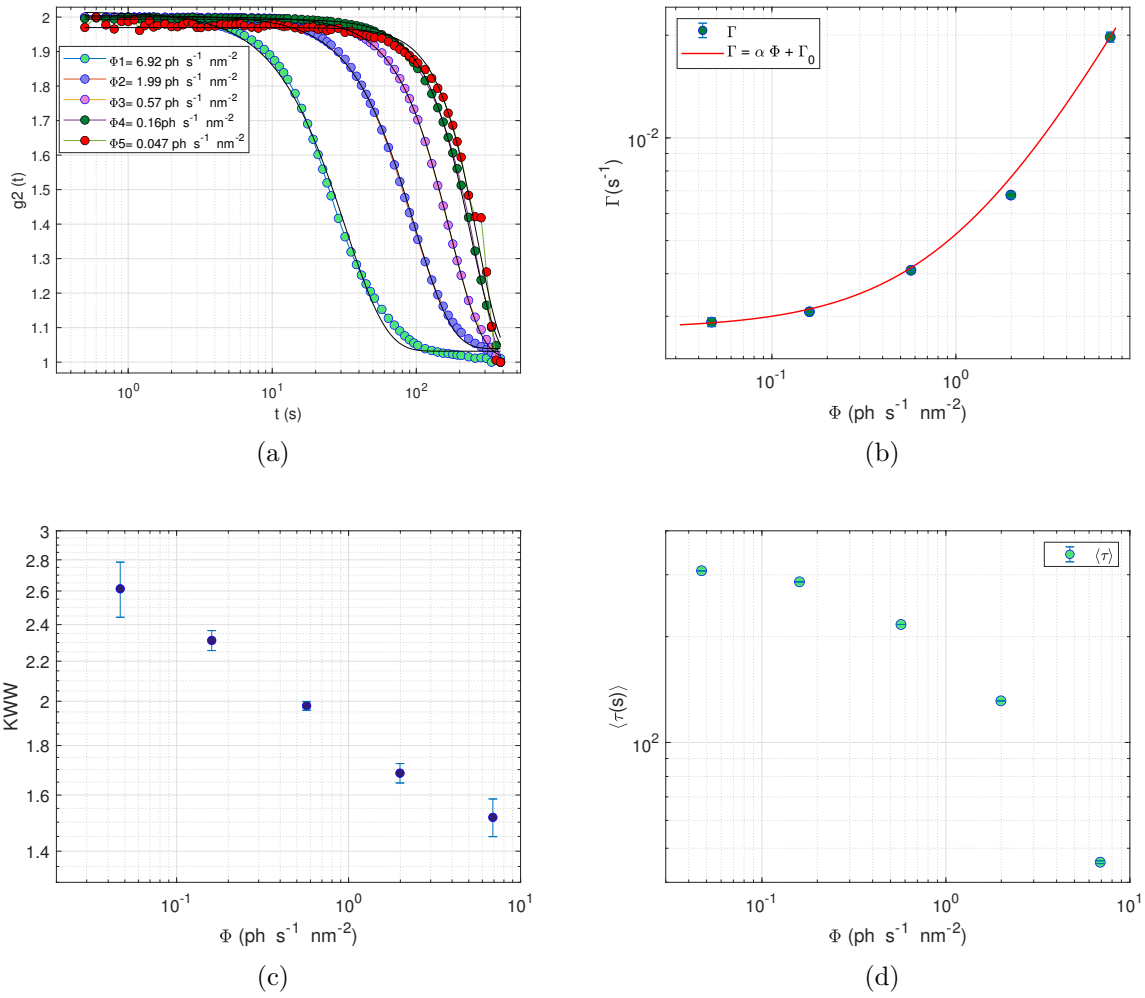


Figure 5.8: The $g^2(q,t)$ functions of the IgG+PEG system are extracted at $T_q = 0$ °C and a wave-vector q = 0.016 nm$^{-1}$ for various photon fluxes from the TTCs. Several dynamics factors, such as the decay rate Γ, the shape exponent KWW, and the average relaxation time $\langle\tau\rangle$, showing a clear dose rate dependence.

In order to identify the distinct impacts of dose and dose rate, we evaluate the dynamics of the sample as a function of photon fluence and dose rate for a fixed accumulated dose value of 55 kGy, as illustrated in Figure 5.9. Multiple dynamics parameters, including decay rate $\Gamma$, shape exponent KWW, and average relaxation time $\langle\tau\rangle$, appear to exhibit a significant dependence on dose rate than dose, as previously demonstrated. This findings suggest that the IgG+PEG sample in the arrested state exhibits a higher susceptibility to the dose rate compared to the accumulated dose. Consequently, it becomes imperative to enhance the precision in determining the damage threshold dose, or critical dose $D_c$. This is necessary due to the fact that the definition of the critical dose $D_c$ for a given system will fluctuate with changes in the dose rate.

The q-dependence of the $g^2(q,t)$ functions for different momentum transfers q is examined at a dose rate of 1.1 kGy $s^{-1}$, as illustrated in Figure 5.10. The analysis reveals a linear relationship, $\Gamma = v\,.\,q$, where $v$ represents the induced velocity. This specific type of motion enables the extraction of mobility $v$ as a q-independent convey of the dynamics of the sample. The observed ballistic motion is a characteristic behavior exhibited by gels and can be attributed to the process of stress release following gel formation [131, 9, 67]. Figure 5.10c displays the velocities as a function of the incoming X-ray fluence for the IgG+PEG sample at a quenching temperature of $T_q = 0$ °C. At the given temperature, the behavior of the sample demonstrates a notable increase in velocity when exposed to high flux levels, while the effect is considerably less prominent at lower flux levels.

The observed induced dynamics can be related to the presence of free radicals in the sample. The primary cause of beam damage in aqueous solutions is the radiolysis product. The decomposition of water under X-ray illumination results in the formation of highly reactive hydroxyl (OH) radicals [50]. Typically, the absorption of 100 eV photon energy leads to the generation of approximately three hydroxyl (OH) radicals [107, 105]. In highly concentrated protein solutions, hydroxyl (OH) radicals rapidly diffuse and interact with the protein surface, resulting in the formation of C-centered protein radicals [20, 50]. In close contact, protein radicals engage in a chemical reaction, resulting in the establishment of permanent covalent bonds among protein molecules [20, 50].

The radical reaction's nonequilibrium characteristics lead to modifications in the free energy landscape while forming bonds. The close interaction between two proteins induces the formation of a localized void inside the neighboring cages of the highly concentrated protein solutions. This void space allows the surrounding proteins to move in a specific direction and relax. Hence, it is anticipated that the active mechanism of radical bond formation will result in an observable quasi-ballistic movement, explaining the compressed

pattern observed in the overall relaxing process [20]. Furthermore, the change in protein activity caused by free radicals results in the formation of protein crosslinks and the fragmentation of proteins [130]. Thus, the above-mentioned processes occurring within the protein solution result in modifications to the dynamics of the sample.
The data can be well characterized using a simple phenomenological model [20, 121], as

$$v(\Phi) = v_0 + \alpha\Phi\,. \tag{5.1}$$

In the given equation, $v_0$ denotes the velocity of the sample at equilibrium, $\Phi$ represents the X-ray fluence, and $\alpha$ is a material-specific constant that characterizes the degree of the X-ray-matter interaction that is accelerating the dynamic of the sample. This linear relationship between dynamics and photon flux has also been discovered in other systems [103, 20]. The statement suggests that the presence of photon flux leads to the emergence of an extra relaxation mechanism where the rate of microscopic events is directly proportional to the applied fluence, as represented by the expression $v = \alpha\,\Phi$. Converting the velocities back into decay times $\Gamma = \alpha\,\Phi\,q$ for the correlation functions and subsequently calculating the dose rate equivalents of these decay lengths provides useful information. Through using this methodology, we will be able to evaluate the nature and magnitude of the induced dynamics caused by the X-ray beam on the sample. Since we already extracted the induced velocity on the IgG+PEG at different fluxes, we could use that information to derive the material-dependent constant $\alpha = 0.29 \pm 0.18\,\mathrm{nm^3\,ph^{-1}}$.
The sample was exposed to fluxes of 0.04 $\mathrm{ph\,nm^{-2}\,s^{-1}}$ and 0.014 $\mathrm{ph\,nm^{-2}\,s^{-1}}$, and the velocities linked to these fluxes were measured as 0.1803 $\mathrm{nm\,s^{-1}}$ and 0.1825 $\mathrm{nm\,s^{-1}}$, respectively. An overlap in the correlation function between the two fluxes is observed in Figures 5.8a and 5.9a. Furthermore, the corresponding velocity values exhibit similarities. Based on the available evidence, it can be concluded that the use of these photon fluxes does not result in any further induced motion in the sample by the beam. Therefore, these values can be considered representative of the intrinsic dynamics of the sample because the difference between them is comparable to the uncertainty value. It is possible to calculate the amount of induced motion the beam caused on the sample in accordance with the previously defined intrinsic dynamics (0.1803 $\mathrm{nm\,s^{-1}}$) of the sample.
The most interesting feature of this investigation is that the high flux used in this experiment can induce driven motion in the sample that is approximately one order of magnitude larger than the sample's intrinsic dynamics. The previously mentioned numerical value is derived from the ratio between the high induced velocity of 2.2041

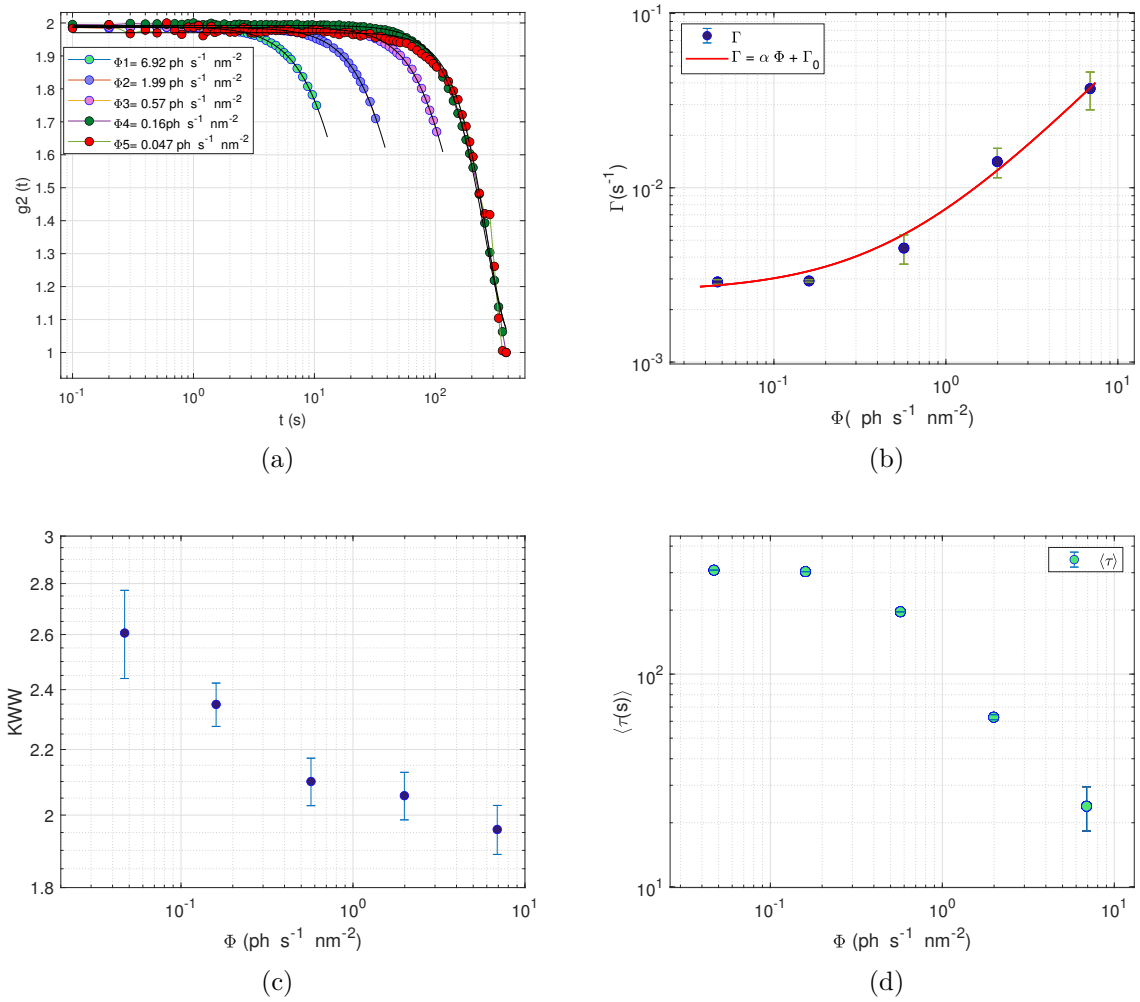


Figure 5.9: For a constant accumulated dose of 55 kGy, the $g^2(q,t)$ functions of the IgG+PEG system and other dynamic parameters are calculated as a function of photon fluence and dose rate.

| $N_{att}$ | Flux (ph $s^{-1}$ $nm^{-2}$) | Dose rate (kGy $s^{-1}$) | $v(nm\,s^{-1})$ | $\Delta v(nm\,s^{-1})$ |
|---|---|---|---|---|
| 0 | 6 | 4 | 2.2041 | 2.02 |
| 4 | 1.7 | 1.1 | 0.9245 | 0.74 |
| 8 | 0.9 | 0.3 | 0.3229 | 0.14 |
| 12 | 0.14 | 0.09 | 0.1825 | 0.0022 |
| 16 | 0.04 | 0.032 | 0.1803 | 0.0 |

Table 5.1: The incident flux, dose rate, velocity related to each photon flux, and the induced velocity, which is calculated as the difference with respect to the defined intrinsic dynamic (0.1803 $nm\,s^{-1}$).

$nm\,s^{-1}$, corresponding to the high flux, and the lowered value of 0.1803 $nm\,s^{-1}$, corresponding to the lower flux used in the present study. This indicates that we must always include the fluence dependence of the dynamics in our XPCS measurements, as this is the only method to distinguish between beam-induced dynamics and the intrinsic dynamics that come from the sample itself. The corresponding calculations for each flux are presented in Table 5.1.

In summary, the findings from our experimental study demonstrate multiple and complicated dynamic reactions of protein solutions when exposed to X-ray radiation. The experimental results obtained from various configurations and samples indicate that exposure to X-ray doses has the potential to induce fluidization in the sample. In addition to the dose, we demonstrated that the dose rate remains an important parameter to control in XPCS measurements. The increased flux has more influence on the sample exhibiting gel-like behavior. The obtained results hold significant relevance for synchrotron experiments that are aimed at studying dynamic phenomena in soft and biological materials. The X-ray fluence has an essential role in determining the shift between the dynamics induced by the X-ray beam and the equilibrium dynamics of the sample. It is essential to improve the accuracy of determining the damage threshold dose, also known as the critical dose $D_c$. This is required because the definition of the critical dose $D_c$ for a given system will fluctuate as the dose rate changes.

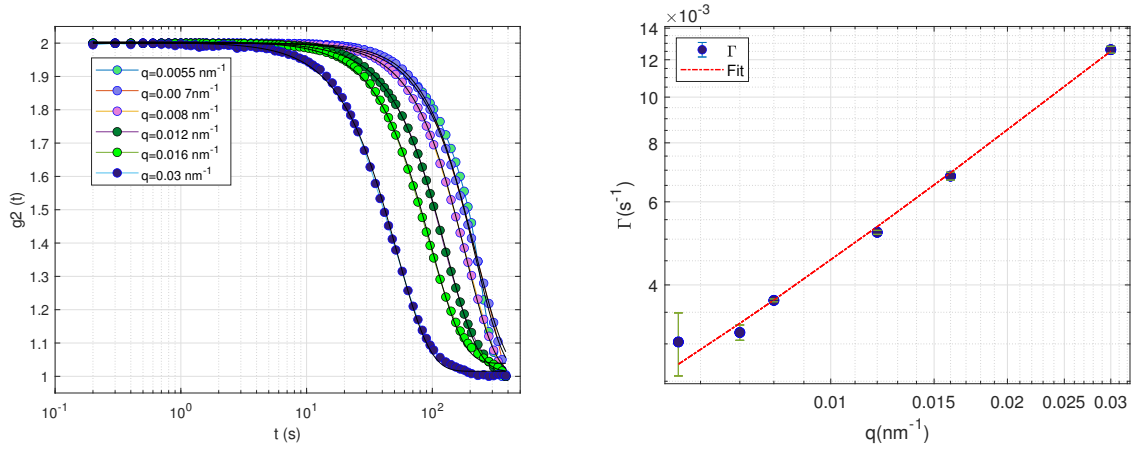


Figure 5.10: (a) At a dose rate of 1.1 kGy $s^{-1}$, the q-dependence of the $g^2(q,t)$ functions for distinct momentum transfers q is determined. (b) The relationship between the decay rates as a function of flux is linear, and (c) represents the corresponding induced velocity as a function of dose rate .

## 5.4 Conclusion

The primary aim of this dissertation was to investigate the possibility of using X-ray photon correlation spectroscopy (XPCS) to investigate the dynamics of phase-separated protein solutions at large q-values. For the purpose of conducting SAXS-XPCS measurements, the conditions for experimental setups and measurement techniques were developed with the objective of minimizing photon density while maintaining an acceptable signal-to-noise ratio. The research successfully demonstrated the possibility of achieving a desirable signal-to-noise ratio (SNR) for the analysis of correlation functions up to q = 1 $nm^{-1}$, which corresponds to the scale of individual proteins. The possible impact of the beam may give rise to uncertainty over the feasibility of constructing a complete and analyzable correlation function by merging numerous correlation functions that cover different time intervals. It is essential that all elements of the correlation functions be measured using photon fluences should be identical.

This study represents the potential and limitations of conducting a successful SAXS-XPCS experiment designed to explore the dynamics of proteins at nanometer-length scales. The correlation function was measured at different quenched temperatures, revealing a clear dependence of protein dynamics on temperature. However, it has been observed that there is a discrepancy in the results obtained from the same sample and experimental setup when different photon fluxes are used. This suggests that the beam had an impact on the dynamic information of the collected data in the SAXS configuration measurements.

Despite conducting thorough investigations across different time and length scales, we still have not been able to answer our questions regarding the specific type of diffusion that occurs at large q values in the state of arrested phase separation. The restriction on the magnitude of beam damage within the SAXS range still remain an open question. A possible solution to address this issue is to modify the setup configuration. This can be done by using a fast shutter and increasing the distance between the sample and the detector. The purpose of this adjustment is to improve the contrast and reduce photon density on the sample, which will eventually lead to a better signal-to-noise ratio and safe measurements.

The second objective of this thesis was to characterize the effects of the beam and determine the type of dynamics that are induced in the sample. Our main focus is on studying and evaluating the dynamic changes that occur when the beam interacts with the sample in the SAXS-XPCS and USAXS-XPCS configurations. To provide more detailed information on this subject, we conducted an experiment to investigate the dynamics

induced by X-ray radiation at different dose rates in dense antibody-protein solutions (Ig+PEG) and BSA+$YCl_3$.

The SAXS-XPCS and USAXS-XPCS experiments were conducted at the DESY P10 beamline. In this study, we performed a comparative analysis of dynamical data collected from different sample positions and incoming fluxes. To ensure accuracy, we adjusted the data by adding X-ray attenuators along the beam path. To conduct a quantitative analysis of this finding, we used the Kohlrausch-Williams-Watts (KWW) expressions (Equation 4.2) to accurately fit the curves. On the base of mentioned analysis, we have observed that the dose rate has an impact on both shape parameter KWW and average relaxation time. Specifically, increasing the dose rate results in a decrease in the average relaxation time $\langle\tau\rangle$. In the SAXS-XPCS setup, it is evident that higher dose rates or fluxes result in faster dynamics and a transition from nearly stretched to compressed signatures. This suggests that the dose rate, rather than the total accumulated dose, is the most important factor in determining beam inducing dynamics in XPCS measurements. The physical states of the sample have a significant role on the susceptibility of the samples to radiation-induced dynamics. The effect of a higher flux on a sample exhibiting gel-like behavior is stronger in comparison to softer gels. In the BSA+$YCl_3$ system, it was also observed that the dose rate has a significant effect on both the shape parameter KWW and the average relaxation time $\langle\tau\rangle$, even if the accumulative dose remains constant. Also, when the dose rates are increased, the average relaxation time decreases, and the KWW shape component increases in relation to the dose rate. In this particular context, the influence of the cumulative dose on dynamics is far less apparent.

A USAXS-XPCS experiment was conducted in order to prevent fast beam damage and to determine the method for distinguishing between beam-induced dynamics and intrinsic dynamics. The results suggest that the lower dose rate has a smaller effect on inducing driven motion in comparison to the higher dose rate, even when the accumulative dose remains constant. In contrast to the SAXS data obtained at higher q-values, the relaxation parameter for KWW shows a decrease as the dose rate increases. This suggests that the beam has the ability to induce diffusion in the sample, which is less compressed at these length scales. A notable feature of this inquiry is the use of high flux in the experiment, which has the capability to create driven motion in the sample. Remarkably, the size of this induced motion is roughly one orders of magnitude larger, than the intrinsic dynamics of the sample. This observation suggests that it is essential to take into consideration the fluence dependency of the dynamics in XPCS measurements. This approach is crucial for distinguishing between the dynamics caused by the X-ray beam and the intrinsic dynamics

originating from the sample itself.

The techniques developed in this thesis serve as a foundation for further investigation in the realm of highly concentrated proteins and soft materials using X-ray methods. XPCS investigations using novel X-ray sources can employ measurement methodologies to clarify phenomena occurring throughout a broad temporal spectrum, spanning from femtoseconds to hours and length scales from droplet size to the nanometer scale. The results of our studies on antibody-protein solutions (IgG+PEG and BSA+$YCl_3$) and egg white protein gels [121], suggest that in order to properly use the high brilliance of 4th generation X-ray sources, experimental setups and synchrotron instruments need to have the capability of effectively reducing photon density. The use of the extended coherence lengths of new sources and the conduct of experiments using large beams are necessary for this purpose. Additionally, fast X-ray detectors with small pixel sizes and increasing the distance between the sample and the detector play important roles in achieving this resolution.

# Acknowledgment

I would like to express my sincere gratitude and appreciation to my supervisor, Prof. Dr. Christian Gutt. His kindness and enthusiasm have been invaluable to me throughout my study journey, from my master's thesis to the present. I am grateful for your insightful feedback, patient mentoring, and unwavering encouragement, as they have been instrumental in shaping and improving this work. I greatly appreciate your expertise and willingness to share your knowledge, as it has significantly contributed to expanding my understanding of the subject matter.

I would like to express my sincere gratitude to my colleagues (Dr. Mario Reiser, Dr. Hendrik Rahmann, Dr. Lisa Randolph, Sonja Timmermann, Clementine Lovato, Ahmed Al-Masoodi , Dr. Amir Tosson, Marvin Kowalski, Michelle Dargasz, Dr. Nimmi Das Anthuparambil, Dr. Dmitriy Ksenzov and Dr. Özgül Öztürk) for their valuable collaboration, which has greatly enhanced my academic experience. Each one of you has made a valuable contribution in your own unique way, resulting in really collaborative and fulfilling work. I greatly appreciate the impact that your input, discussions, and shared insights have had on shaping the direction and enhancing the quality of this thesis. Additionally, the exceptional assistance provided by the team in the preparation and execution of the beam times at DESY is remarkable. The individuals in question consistently showed expertise in problem-solving when faced with challenges, and participating in discussions with them was an enjoyable experience.

I would like to express my sincere gratitude to Dr. Mario Reiser for his valuable assistance at the beginning of my research project. The Xana software has greatly assisted in data analysis. I appreciate the opportunity to work with Xana, and I am grateful for your time and patience in answering my questions regarding the software. And also, a special thanks to Dr. Hendrik Rahmann and Sonja Timmermann for their time and patience in answering my questions about the analysis of the data.

I would also like to express my appreciation to all the collaborators and colleagues from Tübingen University, including PD. Dr. Fajun Zhang, Prof. Dr. Frank Schreiber,

Dr. Anastasia Ragulskaya, Dr. Anita Girelli, Dr. Nafisa Begam, Hanna-Friederike Poggemann, Sebastian Retzbach, and Maximillian Senft, for their collaboration in preparing samples and investigating the dynamics of the IgG-PEG and BSA+$YCl_3$ model systems. I would like to extend my thanks for the numerous shifts we have shared during our beamtimes. It has been a pleasure to collaborate with you, not only in discussing data but also in enjoying many friendly moments among the demanding beamtimes.
Additionally, I would like to say thanks to Fabian Westermeier for his valuable support as a beamline scientist throughout the beamtimes. You were always available to assist us with controlling the beamline, regardless of the time of day or night. Your patience in solving our problems was greatly appreciated.
I am also grateful to all those who have supported me in various ways, be it through encouragement, valuable discussions, or practical assistance. This thesis would not have been possible without your collective influence and contributions.
Specifically, I want to acknowledge the collaboration of my kind friend, Dr. S. Mohamed Yonos Qattali, throughout the editing and correction process.
Finally, I would like to extend my thanks to all my family and friends for their unwavering encouragement and understanding throughout this academic journey. Thanks to my beloved wife, Malina Kamali, for her unwavering support, understanding, and patience throughout this thesis journey. I am also deeply thankful to my parents, my father Abdul Rahim Akhundzadeh, and My lovely mother Najiba Ghafari, for their endless love, guidance, and sacrifices that have paved the way for my academic pursuits. Their unwavering faith in my abilities has been a driving force behind my achievements.

# Abbreviations

**XPCS** X-Ray Photon Correlation Spectroscopy.

**SAXS** Small Angle X-Ray Scattering.

**USAXS** Ultra Small Angle X-Ray Scattering.

**LLPS** liquid-liquid phase separation.

**CHE** Cahn-Hilliard Equation.

**DESY** Deutsches Elektronen-Synchrotron.

**KWW** Kohlrausch–Williams–Watts.

**DLS** Dynamic Light Scattering.

**MW** Molecular Weight.

**PCS** Photon Correlation Spectroscopy.

**PEG** Poly Ethylene Glycol.

**TTC** Two-time correlation function.

**UV-vis** Ultraviolet–Visible Spectroscopy.

**XFEL** X-Ray Free Electron Laser.

**SNR** Signal-to-noise Ratio

**SD** Spinodal Decomposition

**BSA** Bovine Serum Albumin

**IgG** Immunoglobulin G

**LCST/UCST** Lower/Upper Critical Solution Temperature Phase Behaviour

# Appendix

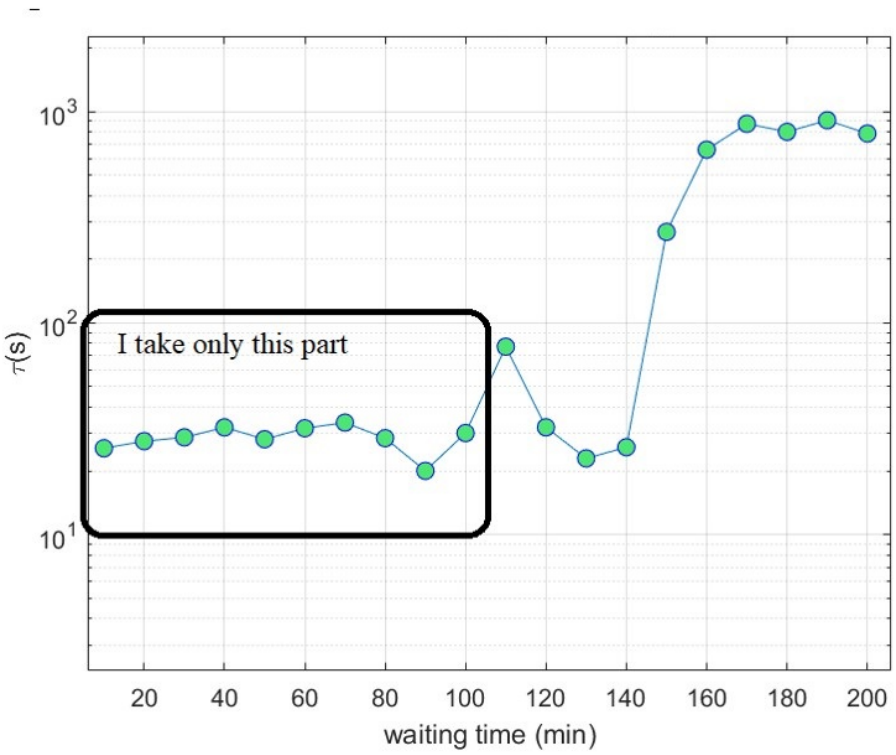


Figure 5.11: In the framework of long-time measurements, one observes a sudden increase in relaxation time, potentially attributable to either the aging features of the sample or the sample becoming freezing at the given temperature. Hence, the relaxation time was measured as a function of waiting time, and only the part of the relaxation time that remained constant with respect to waiting time was included in the calculation.

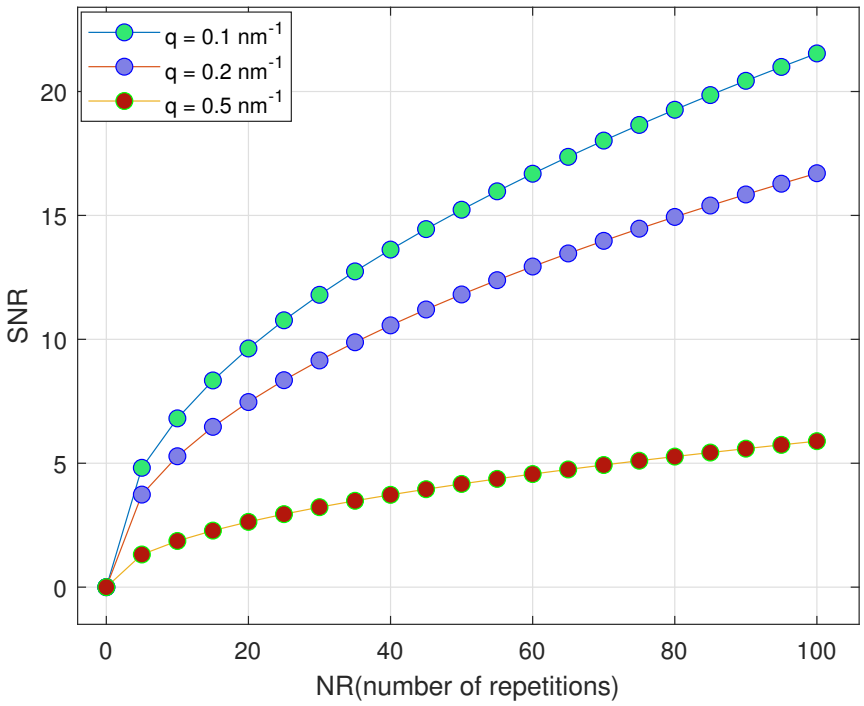


Figure 5.12: The signal-to-noise ratio (SNR) in the above setup increases with an increase in the number of measurement repetitions. Most of the time, an SNR of 1 or higher is good enough for basic measures because it shows that the signal strength is higher than the noise level.

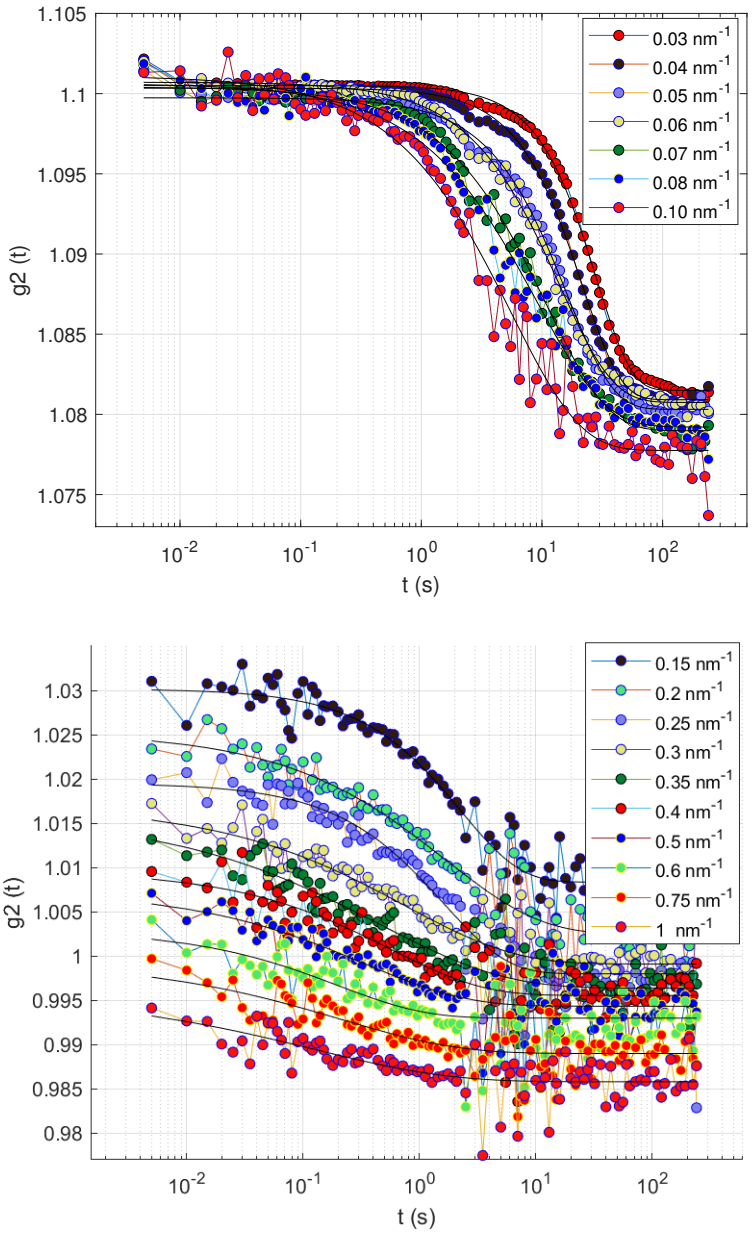


Figure 5.13: The correlation function for the IgG protein sample after quenching the system from T = 37 °C to $T_q$ = -5 °C in the q-range of 0.03 $nm^{-1}$ to 1 $nm^{-1}$ and the fit is displayed in the black line. The correlation functions were stitched together in both time scales of 4 s and 300 s.

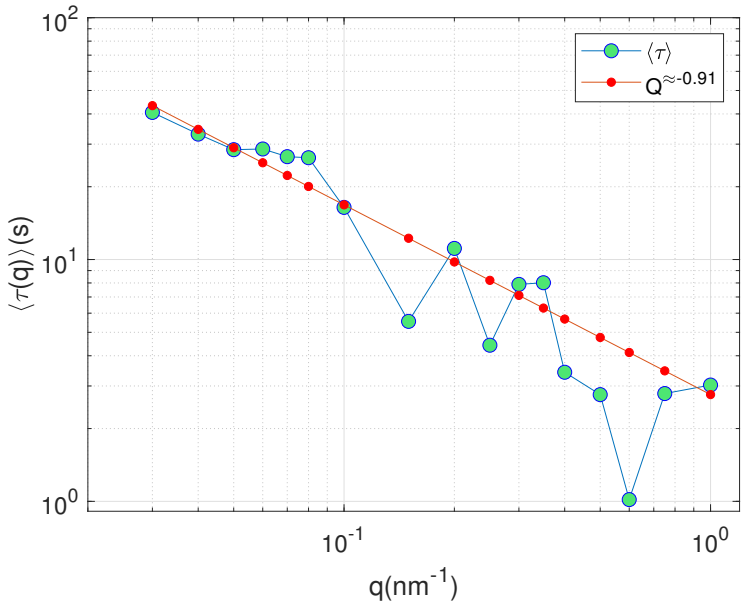


(a)

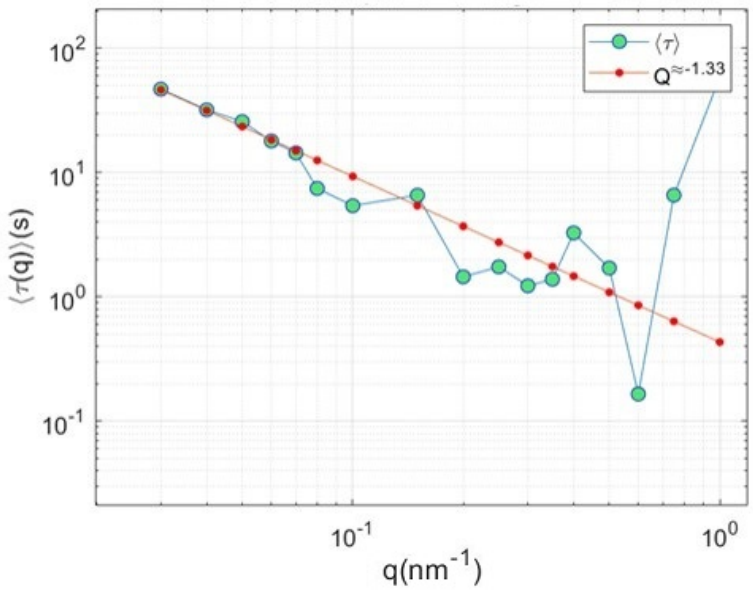


(b)

Figure 5.14: The displayed figures indicate the wave vector dependency of the average relaxation time as a function of q at different temperatures (a) T= -5 °C (b) T= 6 °C. The observed wave vector dependencies of the relaxation times suggest that the dynamics of the sample in the arrested state have features like ballistic motion, particularly at lower temperatures.

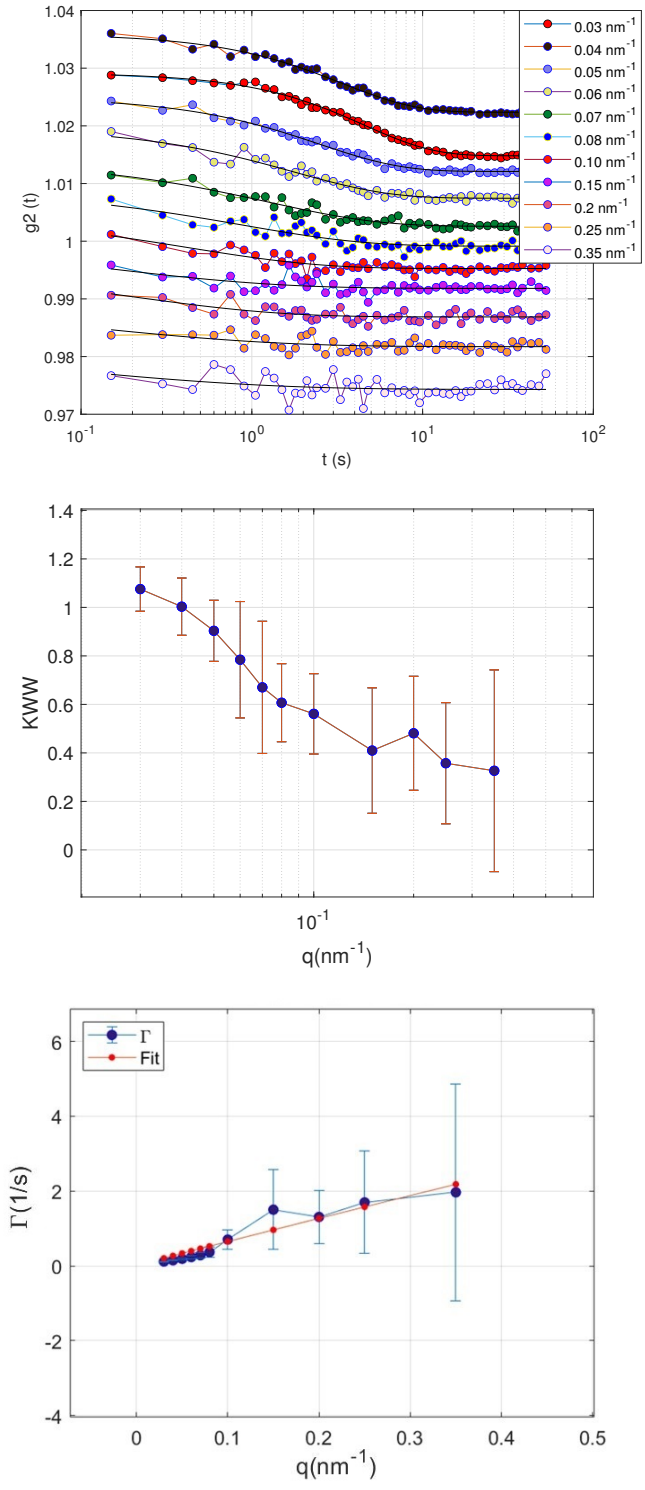


Figure 5.15: The correlation functions for the BSA protein sample after quenching the system from T = 37 °C to $T_q$ = 49 °C in the q-range of 0.03 $nm^{-1}$ to 0.35 $nm^{-1}$ and the fit are displayed in the black line. Both the decay rate G and the KWW exponent exhibit a clear dependence on the wave vector q.

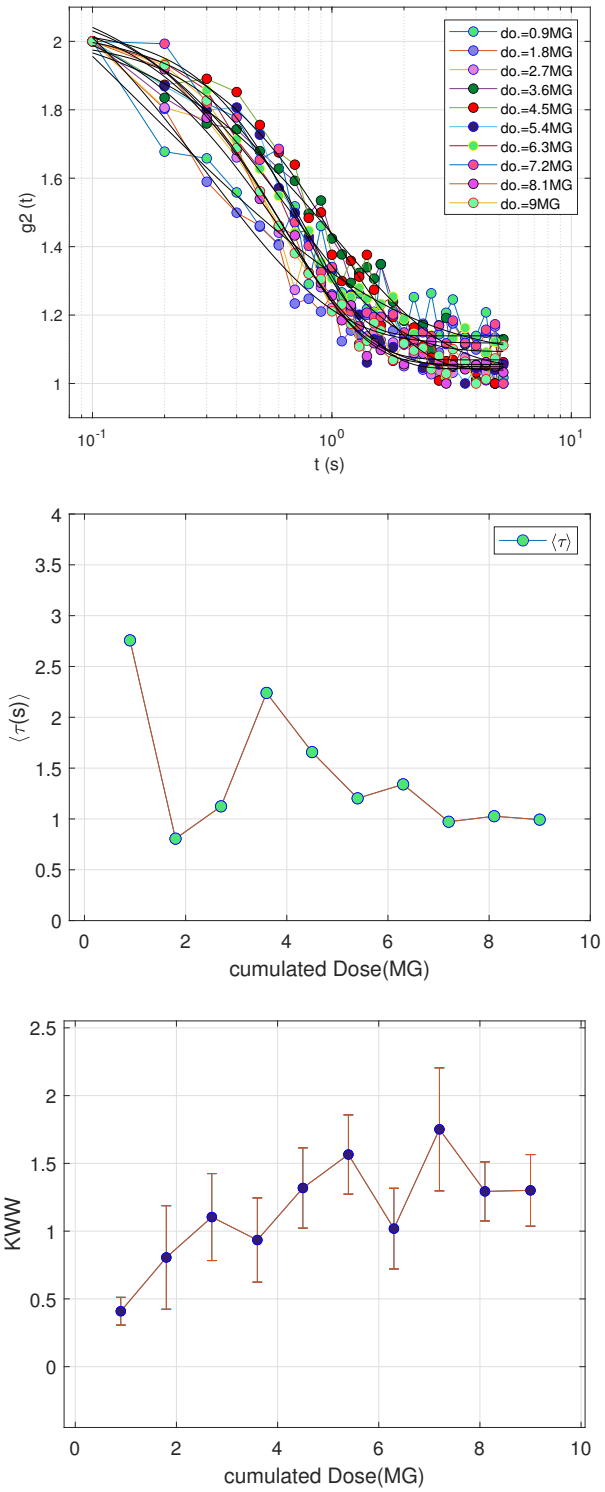


Figure 5.16: The correlation function measured at constant photon flux and different accumulated doses for the IgG protein sample after quenching the system from T = 37 °C to $T_q$ = 0 °C with a q-value of 0.35 $nm^{-1}$ is displayed in the black line. The KWW exponent is increasing as a function of the accumulated dose, but the average relaxation time exhibits a small variation.

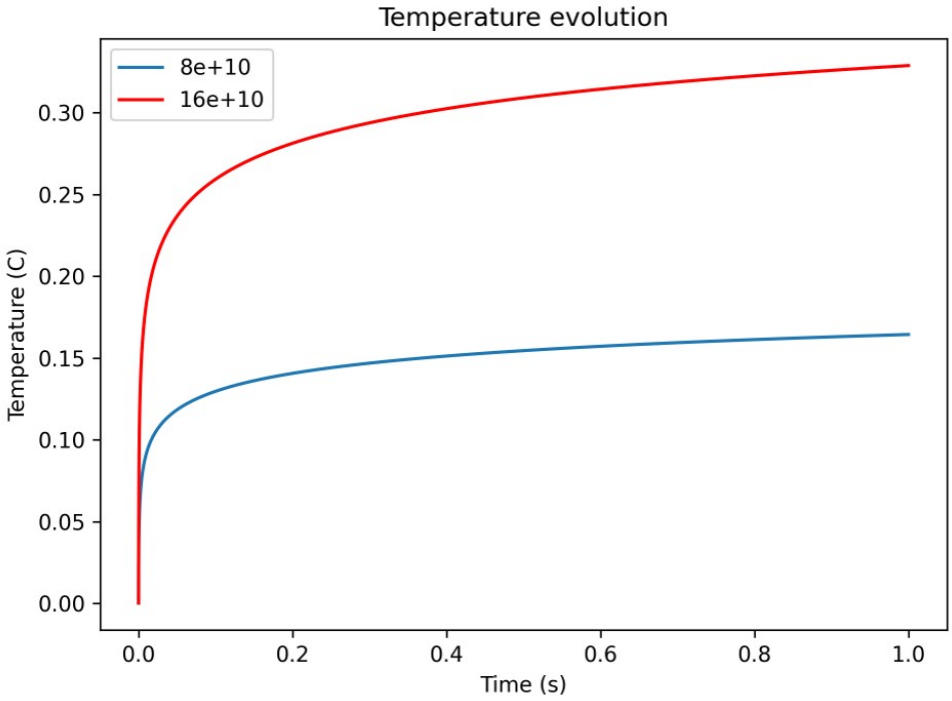


Figure 5.17: The high photon flux has the potential to generate thermal effects within the sample. However, as illustrated in the accompanying figure, the resulting temperature increase is only 0.15 °C, which is insufficient to significantly change the dynamic characteristics of the sample. The above-mentioned calculation was performed by Yuriy Chushkin.

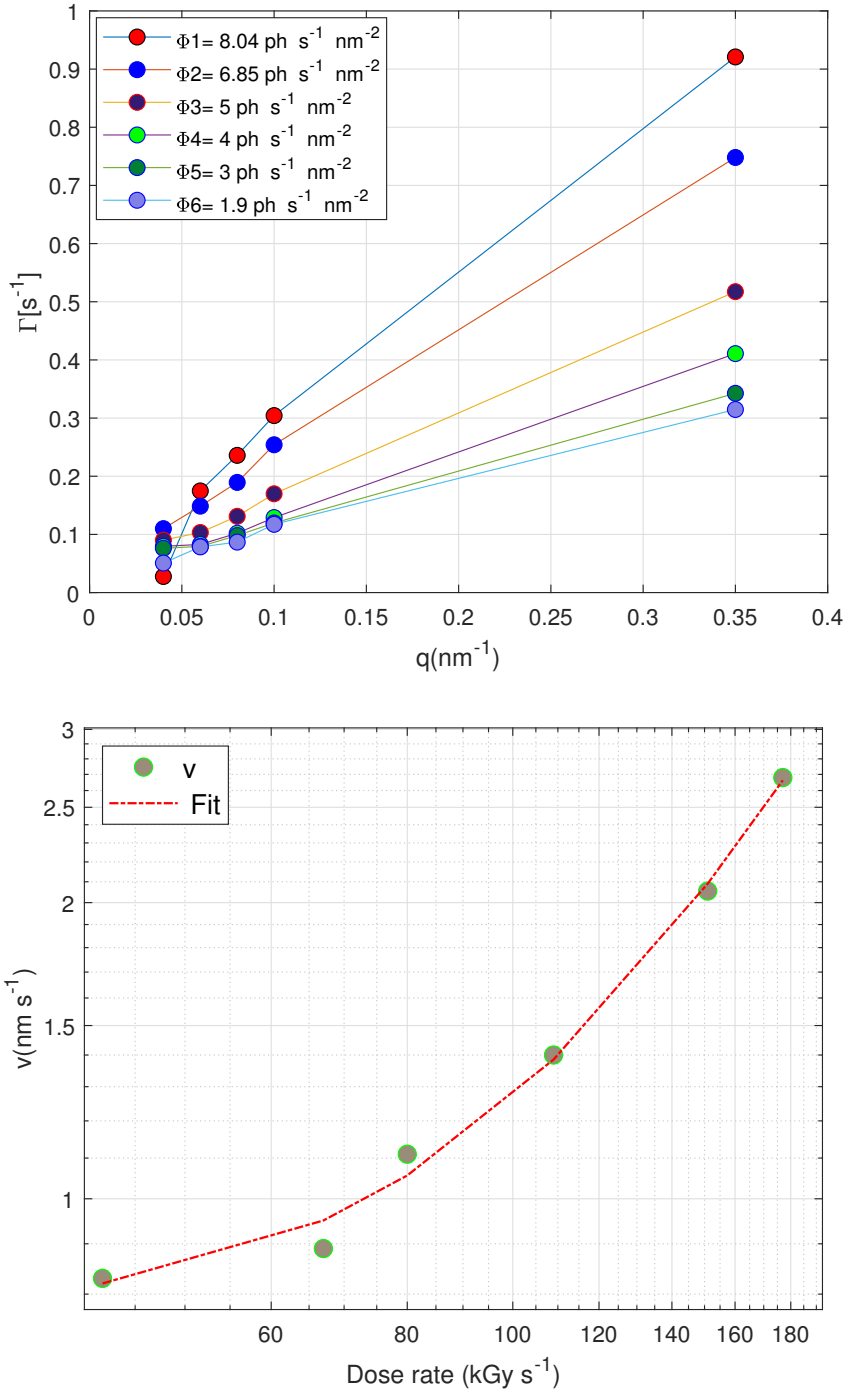


Figure 5.18: In the SAXS-XPCS configuration, the decay rates as a function of photon flux are linear and measured for various fluxes, and the induced velocity increases as a function of dose rate.

# Bibliography


[1] Desy, p10 - coherence applications beamline. https://photon-science.desy.de/facilities/petraiii/beamlines/p10coherenceapplications/indexeng.html.

[2] High-resolution photon counting x-ray detectors from dectris eiger r series. https://www.rigaku.com/products/detectors/eiger.

[3] Linkam hfsx350 heating freezing stag. https://www.meyerinst.com/home/linkam-scientific-instruments/linkam-hfsx350/.

[4] Polyethylene glycol 1,000. https://hamptonresearch.com/product-Polyethylene-glycol-1-000-154.html.

[5] Jens Als-Nielsen and Des McMorrow. *Elements of modern X-ray physics*. John Wiley & Sons, 2011.

[6] Narges Amini, Fan Yang, E Pineda, Beatrice Ruta, M Sprung, and A Meyer. Intrinsic relaxation in a supercooled zrtinicube glass forming liquid. *Physical Review Materials*, 5(5):055601, 2021.

[7] Alain AM André and Evan Spruijt. Liquid–liquid phase separation in crowded environments. *International Journal of Molecular Sciences*, 21(16):5908, 2020.

[8] Roberta Angelini, Emanuela Zaccarelli, Flavio Augusto de Melo Marques, Michael Sztucki, Andrei Fluerasu, Giancarlo Ruocco, and Barbara Ruzicka. Glass–glass transition during aging of a colloidal clay. *Nature communications*, 5(1):4049, 2014.

[9] Nafisa Begam, Anastasia Ragulskaya, Anita Girelli, Hendrik Rahmann, Sivasurender Chandran, Fabian Westermeier, Mario Reiser, Michael Sprung, Fajun Zhang, Christian Gutt, et al. Kinetics of network formation and heterogeneous

dynamics of an egg white gel revealed by coherent x-ray scattering. *Physical review letters*, 126(9):098001, 2021.

[10] Martin J Berger. Xcom: photon cross sections database. *http://physics. nist. gov/PhysRefData/Xcom/Text/XCOM. html*, 8:3587, 1998.

[11] Joel Berry, Clifford P Brangwynne, and Mikko Haataja. Physical principles of intracellular organization via active and passive phase transitions. *Reports on Progress in Physics*, 81(4):046601, 2018.

[12] Oier Bikondoa. On the use of two-time correlation functions for x-ray photon correlation spectroscopy data analysis. *Journal of applied crystallography*, 50(2):357–368, 2017.

[13] Kurt Binder and Peter Fratzl. Spinodal decomposition. *Phase transformations in materials*, pages 409–480, 2001.

[14] S Brauer, GB Stephenson, M Sutton, R Brüning, E Dufresne, SGJ Mochrie, G Grübel, Jens Als-Nielsen, and DL Abernathy. X-ray intensity fluctuation spectroscopy observations of critical dynamics in f e 3 al. *Physical review letters*, 74(11):2010, 1995.

[15] John W Cahn and John E Hilliard. Free energy of a nonuniform system. i. interfacial free energy. *The Journal of chemical physics*, 28(2):258–267, 1958.

[16] Li-Heng Cai, Sergey Panyukov, and Michael Rubinstein. Mobility of nonsticky nanoparticles in polymer liquids. *Macromolecules*, 44(19):7853–7863, 2011.

[17] Jerome Carnis, Wonsuk Cha, James Wingert, Jinback Kang, Zhang Jiang, Sanghoon Song, Marcin Sikorski, Aymeric Robert, Christian Gutt, San-Wen Chen, et al. Demonstration of feasibility of x-ray free electron laser studies of dynamics of nanoparticles in entangled polymer melts. *Scientific reports*, 4(1):6017, 2014.

[18] Chiara Caronna, Yuriy Chushkin, Anders Madsen, and Antonio Cupane. Dynamics of nanoparticles in a supercooled liquid. *Physical review letters*, 100(5):055702, 2008.

[19] Miaoqi Chu, Jeffrey Li, Qingteng Zhang, Zhang Jiang, Eric M Dufresne, Alec Sandy, Suresh Narayanan, and Nicholas Schwarz. pyxpcsviewer: an open-source interactive tool for x-ray photon correlation spectroscopy visualization and analysis. *Journal of Synchrotron Radiation*, 29(4):1122–1129, 2022.

[20] Yuriy Chushkin, Alessandro Gulotta, Felix Roosen-Runge, Antara Pal, Anna Stradner, and Peter Schurtenberger. Probing cage relaxation in concentrated protein solutions by x-ray photon correlation spectroscopy. *Physical Review Letters*, 129(23):238001, 2022.

[21] Protein Condensation. Kinetic pathways to crystallization and disease, ed. jd gunton, a. shiryayev and dl pagan, 2007.

[22] Heiko Conrad, Felix Lehmkuehler, Birgit Fischer, Fabian Westermeier, MA Schroer, Yuriy Chushkin, Christian Gutt, Michael Sprung, and Gerhard Gruebel. Correlated heterogeneous dynamics in glass-forming polymers. *Physical Review E*, 91(4):042309, 2015.

[23] Stefano Da Vela, Michal K Braun, Andreas Dörr, Alessandro Greco, Johannes Möller, Zhendong Fu, Fajun Zhang, and Frank Schreiber. Kinetics of liquid–liquid phase separation in protein solutions exhibiting lcst phase behavior studied by time-resolved usaxs and vsans. *Soft Matter*, 12(46):9334–9341, 2016.

[24] Stefano Da Vela, Christian Exner, Richard Santiago Schäufele, Johannes Möller, Zhendong Fu, Fajun Zhang, and Frank Schreiber. Arrested and temporarily arrested states in a protein–polymer mixture studied by usaxs and vsans. *Soft Matter*, 13(46):8756–8765, 2017.

[25] Stefano Da Vela, Felix Roosen-Runge, Maximilian WA Skoda, Robert MJ Jacobs, Tilo Seydel, Henrich Frielinghaus, Michael Sztucki, Ralf Schweins, Fajun Zhang, and Frank Schreiber. Effective interactions and colloidal stability of bovine $\gamma$-globulin in solution. *The Journal of Physical Chemistry B*, 121(23):5759–5769, 2017.

[26] Amlan Das, Peter M Derlet, Chaoyang Liu, Eric M Dufresne, and Robert Maaß. Stress breaks universal aging behavior in a metallic glass. *Nature communications*, 10(1):5006, 2019.

[27] SB Dierker, R Pindak, RM Fleming, IK Robinson, and L Berman. X-ray photon correlation spectroscopy study of brownian motion of gold colloids in glycerol. *Physical Review Letters*, 75(3):449, 1995.

[28] Dennis J Dietzen. Amino acids, peptides, and proteins. In *Principles and Applications of Molecular Diagnostics*, pages 345–380. Elsevier, 2018.

[29] Ruo-Yu Dong and Steve Granick. Reincarnations of the phase separation problem. *Nature Communications*, 12(1):911, 2021.

[30] Anisha A D'souza and Ranjita Shegokar. Polyethylene glycol (peg): a versatile polymer for pharmaceutical applications. *Expert opinion on drug delivery*, 13(9):1257–1275, 2016.

[31] Zach Evenson, Beatrice Ruta, Simon Hechler, Moritz Stolpe, Eloi Pineda, Isabella Gallino, and Ralf Busch. X-ray photon correlation spectroscopy reveals intermittent aging dynamics in a metallic glass. *Physical review letters*, 115(17):175701, 2015.

[32] Andrei Fluerasu, Abdellatif Moussaïd, Anders Madsen, and Andrew Schofield. Slow dynamics and aging in colloidal gels studied by x-ray photon correlation spectroscopy. *Physical Review E*, 76(1):010401, 2007.

[33] Giuseppe Foffi, Gabriela Savin, Saskia Bucciarelli, Nicolas Dorsaz, George M Thurston, Anna Stradner, and Peter Schurtenberger. Hard sphere-like glass transition in eye lens $\alpha$-crystallin solutions. *Proceedings of the National Academy of Sciences*, 111(47):16748–16753, 2014.

[34] Erwin Frey and Klaus Kroy. Brownian motion: a paradigm of soft matter and biological physics. *Annalen der Physik*, 517(1-3):20–50, 2005.

[35] Janusz M Gebicki and Thomas Nauser. Initiation and prevention of biological damage by radiation-generated protein radicals. *International Journal of Molecular Sciences*, 23(1):396, 2021.

[36] Thomas Gibaud, Najet Mahmoudi, Julian Oberdisse, Peter Lindner, Jan Skov Pedersen, Cristiano LP Oliveira, Anna Stradner, and Peter Schurtenberger. New routes to food gels and glasses. *Faraday discussions*, 158(1):267–284, 2012.

[37] Valeriy V Ginzburg. A simple mean-field model of glassy dynamics and glass transition. *Soft matter*, 16(3):810–825, 2020.

[38] Anita Girelli. *Dynamics of Antibodies in Solution: from Individual Proteins to Phase Separation Domains*. PhD thesis, Universität Tübingen, 2024.

[39] Anita Girelli, Hendrik Rahmann, Nafisa Begam, Anastasia Ragulskaya, Mario Reiser, Sivasurender Chandran, Fabian Westermeier, Michael Sprung, Fajun Zhang,

Christian Gutt, et al. Microscopic dynamics of liquid-liquid phase separation and domain coarsening in a protein solution revealed by x-ray photon correlation spectroscopy. *Physical Review Letters*, 126(13):138004, 2021.

[40] Otto Glatter. Small angle x-ray scattering. *(No Title)*, 1982.

[41] Joseph W Goodman. Some fundamental properties of speckle. *JOSA*, 66(11):1145–1150, 1976.

[42] Joseph W Goodman. *Statistical optics*. John Wiley & Sons, 2015.

[43] Marco Grimaldo, Felix Roosen-Runge, Fajun Zhang, Frank Schreiber, and Tilo Seydel. Dynamics of proteins in solution. *Quarterly Reviews of Biophysics*, 52:e7, 2019.

[44] G Grübel, J Als-Nielsen, D Abernathy, G Vignaud, S Brauer, GB Stephenson, SGJ Mochrie, M Sutton, IK Robinson, R Fleming, et al. Scattering with coherent x-rays. *ESRF Newslett.*, (20):14–15, 1994.

[45] G Grübel, GB Stephenson, C Gutt, H Sinn, and Th Tschentscher. Xpcs at the european x-ray free electron laser facility. *Nuclear Instruments and Methods in Physics Research Section B: Beam Interactions with Materials and Atoms*, 262(2):357–367, 2007.

[46] Jörg Gsponer and M Madan Babu. Cellular strategies for regulating functional and nonfunctional protein aggregation. *Cell reports*, 2(5):1425–1437, 2012.

[47] Hongyu Guo, Gilles Bourret, R Bruce Lennox, Mark Sutton, James L Harden, and Robert L Leheny. Entanglement-controlled subdiffusion of nanoparticles within concentrated polymer solutions. *Physical review letters*, 109(5):055901, 2012.

[48] Hongyu Guo, S Ramakrishnan, James L Harden, and Robert L Leheny. Gel formation and aging in weakly attractive nanocolloid suspensions at intermediate concentrations. *The Journal of chemical physics*, 135(15), 2011.

[49] C Gutt, L-M Stadler, Agnes Duri, T Autenrieth, O Leupold, Y Chushkin, and G Grübel. Measuring temporal speckle correlations at ultrafast x-ray sources. *Optics express*, 17(1):55–61, 2009.

[50] Clare L Hawkins and Michael J Davies. Generation and propagation of radical reactions on proteins. *Biochimica et Biophysica Acta (BBA)-Bioenergetics*, 1504(2-3):196–219, 2001.

[51] Richard Henderson. The potential and limitations of neutrons, electrons and x-rays for atomic resolution microscopy of unstained biological molecules. *Quarterly reviews of biophysics*, 28(2):171–193, 1995.

[52] Karel Heremans and L Smeller. Protein structure and dynamics at high pressure. *Biochimica et Biophysica Acta (BBA)-Protein Structure and Molecular Enzymology*, 1386(2):353–370, 1998.

[53] Felix Höfling and Thomas Franosch. Anomalous transport in the crowded world of biological cells. *Reports on Progress in Physics*, 76(4):046602, 2013.

[54] Taiki Hoshino, Yasushi Okamoto, Atsushi Yamamoto, and Hiroyasu Masunaga. Heterogeneous dynamics in the curing process of epoxy resins. *Scientific reports*, 11(1):9767, 2021.

[55] JH Hubbell. Photon cross sections, attenuation coefficients and energy absorption coefficients. *National Bureau of Standards Report NSRDS-NBS29, Washington DC*, 1969.

[56] Gary L Hunter and Eric R Weeks. The physics of the colloidal glass transition. *Reports on progress in physics*, 75(6):066501, 2012.

[57] Rintaro Inoue, Takashi Oda, Hiroshi Nakagawa, Taiki Tominaga, Tomohide Saio, Yukinobu Kawakita, Masahiro Shimizu, Aya Okuda, Ken Morishima, Nobuhiro Sato, et al. Dynamics of proteins with different molecular structures under solution condition. *Scientific Reports*, 10(1):21678, 2020.

[58] Louise Jawerth, Elisabeth Fischer-Friedrich, Suropriya Saha, Jie Wang, Titus Franzmann, Xiaojie Zhang, Jenny Sachweh, Martine Ruer, Mahdiye Ijavi, Shambaditya Saha, et al. Protein condensates as aging maxwell fluids. *Science*, 370(6522):1317–1323, 2020.

[59] I Johnson, Anna Bergamaschi, Heiner Billich, S Cartier, Roberto Dinapoli, Dominic Greiffenberg, Manuel Guizar-Sicairos, B Henrich, J Jungmann, Davide Mezza,

et al. Eiger: a single-photon counting x-ray detector. *Journal of Instrumentation*, 9(05):C05032, 2014.

[60] Robertus Petrus Joosten. *X-Ray structure re-refinement. Combining old data with new methods for better structural bioinformatics.* [Sl: sn], 2010.

[61] Karin Julius, Jonathan Weine, Mimi Gao, Jan Latarius, Mirko Elbers, Michael Paulus, Metin Tolan, and Roland Winter. Impact of macromolecular crowding and compression on protein–protein interactions and liquid–liquid phase separation phenomena. *Macromolecules*, 52(4):1772–1784, 2019.

[62] Toshimitsu Kanai, Niels Boon, Peter J Lu, Eli Sloutskin, Andrew B Schofield, Frank Smallenburg, René van Roij, Marjolein Dijkstra, David A Weitz, et al. Crystallization and reentrant melting of charged colloids in nonpolar solvents. *Physical Review E*, 91(3):030301, 2015.

[63] Tatiana Konstantinova, Lutz Wiegart, Maksim Rakitin, Anthony M DeGennaro, and Andi M Barbour. Machine learning enhances algorithms for quantifying non-equilibrium dynamics in correlation spectroscopy experiments to reach frame-rate-limited time resolution. *arXiv preprint arXiv:2201.07889*, 2022.

[64] Shigeo Kuwamoto, Shuji Akiyama, and Tetsuro Fujisawa. Radiation damage to a protein solution, detected by synchrotron x-ray small-angle scattering: dose-related considerations and suppression by cryoprotectants. *Journal of synchrotron radiation*, 11(6):462–468, 2004.

[65] J Lal, D Abernathy, L Auvray, O Diat, and G Grübel. Dynamics and correlations in magnetic colloidal systems studied by x-ray photon correlation spectroscopy. *The European Physical Journal E*, 4:263–271, 2001.

[66] Jyotsana Lal, LB Lurio, Dennis Liang, Suresh Narayanan, SB Darling, and Mark Sutton. Kinetic viscoelasticity during early polymer-polymer spinodal dewetting. *Physical Review Research*, 3(4):043162, 2021.

[67] Domenico Larobina, Angelo Pommella, Adrian-Marie Philippe, Med Yassine Nagazi, and Luca Cipelletti. Enhanced microscopic dynamics in mucus gels under a mechanical load in the linear viscoelastic regime. *Proceedings of the National Academy of Sciences*, 118(45):e2103995118, 2021.

[68] Sooheyong Lee, W Roseker, C Gutt, B Fischer, H Conrad, F Lehmkühler, I Steinke, D Zhu, H Lemke, M Cammarata, et al. Single shot speckle and coherence analysis of the hard x-ray free electron laser lcls. *Optics express*, 21(21):24647–24664, 2013.

[69] Sooheyong Lee, W Roseker, C Gutt, B Fischer, H Conrad, F Lehmkuhler, I Steinke, D Zhu, H Lemke, M Cammarata, et al. Single shot speckle and coherence analysis of the hard x-ray free electron. Technical report, SLAC National Accelerator Lab., Menlo Park, CA (United States), 2014.

[70] Felix Lehmkühler, Birgit Hankiewicz, Martin A Schroer, Leonard Müller, Beatrice Ruta, Dina Sheyfer, Michael Sprung, Kensuke Tono, Tetsuo Katayama, Makina Yabashi, et al. Slowing down of dynamics and orientational order preceding crystallization in hard-sphere systems. *Science advances*, 6(43):eabc5916, 2020.

[71] Michael Leitner, Bogdan Sepiol, Lorenz-Mathias Stadler, and Bastian Pfau. Time-resolved study of the crystallization dynamics in a metallic glass. *Physical Review B*, 86(6):064202, 2012.

[72] Jianheng Li, Rahul Jangid, Weidi Zhu, Chris Kohne, Andrei Fluerasu, Yugang Zhang, Sabyasachi Sen, and Roopali Kukreja. Dynamics at the crystal-melt interface in a supercooled chalcogenide liquid near the glass transition. *Scientific reports*, 10(1):5881, 2020.

[73] Jie Lin. Modeling the aging of protein condensates. *Physical Review Research*, 4(2):L022012, 2022.

[74] Laurence B Lurio, George M Thurston, Qingteng Zhang, Suresh Narayanan, and Eric M Dufresne. Use of continuous sample translation to reduce radiation damage for xpcs studies of protein diffusion. *Journal of Synchrotron Radiation*, 28(2):490–498, 2021.

[75] Anders Madsen, Andrei Fluerasu, and Beatrice Ruta. Structural dynamics of materials probed by x-ray photon correlation spectroscopy. *Synchrotron Light Sources and Free-Electron Lasers: Accelerator Physics, Instrumentation and Science Applications*, pages 1989–2018, 2020.

[76] Anders Madsen, Robert L Leheny, Hongyu Guo, Michael Sprung, and Orsolya Czakkel. Beyond simple exponential correlation functions and equilibrium dynamics

in x-ray photon correlation spectroscopy. *New Journal of Physics*, 12(5):055001, 2010.

[77] Anupa Majumdar, Priyanka Dogra, Shiny Maity, and Samrat Mukhopadhyay. Liquid–liquid phase separation is driven by large-scale conformational unwinding and fluctuations of intrinsically disordered protein molecules. *The journal of physical chemistry letters*, 10(14):3929–3936, 2019.

[78] Suliana Manley, HM Wyss, K Miyazaki, JC Conrad, V Trappe, LJ Kaufman, DR Reichman, and DA Weitz. Glasslike arrest in spinodal decomposition as a route to colloidal gelation. *Physical review letters*, 95(23):238302, 2005.

[79] Olga Matsarskaia, Michal K Braun, Felix Roosen-Runge, Marcell Wolf, Fajun Zhang, Roland Roth, and Frank Schreiber. Cation-induced hydration effects cause lower critical solution temperature behavior in protein solutions. *The Journal of Physical Chemistry B*, 120(31):7731–7736, 2016.

[80] Steve P Meisburger, Matthew Warkentin, Huimin Chen, Jesse B Hopkins, Richard E Gillilan, Lois Pollack, and Robert E Thorne. Breaking the radiation damage limit with cryo-saxs. *Biophysical journal*, 104(1):227–236, 2013.

[81] SGJ Mochrie, AM Mayes, AR Sandy, M Sutton, S Brauer, GB Stephenson, DL Abernathy, and G Grübel. Dynamics of block copolymer micelles revealed by x-ray intensity fluctuation spectroscopy. *Physical review letters*, 78(7):1275, 1997.

[82] Johannes Möller, Mario Reiser, Jörg Hallmann, Ulrike Boesenberg, Alexey Zozulya, Hendrik Rahmann, Anna-Lena Becker, Fabian Westermeier, Thomas Zinn, Michael Sprung, et al. Using low dose x-ray speckle visibility spectroscopy to study dynamics of soft matter samples. *New Journal of Physics*, 23(9):093041, 2021.

[83] Johannes Möller, Michael Sprung, Anders Madsen, and Christian Gutt. X-ray photon correlation spectroscopy of protein dynamics at nearly diffraction-limited storage rings. *IUCrJ*, 6(5):794–803, 2019.

[84] Efstratios Mylonas and Dmitri I Svergun. Accuracy of molecular mass determination of proteins in solution by small-angle x-ray scattering. *Journal of applied crystallography*, 40(s1):s245–s249, 2007.

[85] Simone Napolitano, Emmanouil Glynos, and Nicholas B Tito. Glass transition of polymers in bulk, confined geometries, and near interfaces. *Reports on Progress in Physics*, 80(3):036602, 2017.

[86] David Paganin. *Coherent X-ray optics*. Number 6. Oxford University Press, USA, 2006.

[87] Pierre Papon, Jacques Leblond, and Paul HE Meijer. *Physics of Phase Transitions*. Springer-Verlag Berlin Heidelberg, Germany, 2002.

[88] Jan Skov Pedersen. Determination of size distribution from small-angle scattering data for systems with effective hard-sphere interactions. *Journal of applied crystallography*, 27(4):595–608, 1994.

[89] Fivos Perakis and Christian Gutt. Towards molecular movies with x-ray photon correlation spectroscopy. *Physical Chemistry Chemical Physics*, 22(35):19443–19453, 2020.

[90] Joachim Pflueger. Undulator technology. *CERN Yellow Reports: School Proceedings*, 1:55–55, 2018.

[91] Edward Roy Pike and John B Abbiss. *Light scattering and photon correlation spectroscopy*, volume 40. Springer Science & Business Media, 2012.

[92] Giovanna Pintori, Giacomo Baldi, Beatrice Ruta, and Giulio Monaco. Relaxation dynamics induced in glasses by absorption of hard x-ray photons. *Physical Review B*, 99(22):224206, 2019.

[93] Dariusz Plewczyński and Krzysztof Ginalski. The interactome: predicting the protein-protein interactions in cells. *Cellular and Molecular Biology Letters*, 14(1):1–22, 2009.

[94] D Pontoni, T Narayanan, J-M Petit, G Grübel, and Daniel Beysens. Microstructure and dynamics near an attractive colloidal glass transition. *Physical review letters*, 90(18):188301, 2003.

[95] PN Pusey. Statistical properties of scattered radiation. In *Photon correlation spectroscopy and velocimetry*, pages 45–141. Springer, 1977.

[96] Anastasia Ragulskaya. *Dynamics of liquid-liquid phase separation in protein solutions probed by coherent X-ray scattering.* PhD thesis, Universität Tübingen, 2023.

[97] Anastasia Ragulskaya, Vladimir Starostin, Nafisa Begam, Anita Girelli, Hendrik Rahmann, Mario Reiser, Fabian Westermeier, Michael Sprung, Fajun Zhang, Christian Gutt, et al. Reverse-engineering method for xpcs studies of non-equilibrium dynamics. *IUCrJ*, 9(4):439–448, 2022.

[98] Hendrik Rahmann. Realization of low dose xpcs experiments for the investigation of protein dynamics. 2020.

[99] Mario Reiser. A nanorheology study on the viscoelastic properties of photorheological liquids by x-ray photon correlation spectroscopy. 2020.

[100] Mario Reiser, Anita Girelli, Anastasia Ragulskaya, Sudipta Das, Sharon Berkowicz, Maddalena Bin, Marjorie Ladd-Parada, Mariia Filianina, Hanna-Friederike Poggemann, Nafisa Begam, et al. Resolving molecular diffusion and aggregation of antibody proteins with megahertz x-ray free-electron laser pulses. *Nature Communications*, 13(1):5528, 2022.

[101] A Robert, J Wagner, T Autenrieth, W Härtl, and G Grübel. Coherent x-rays as a new probe for the investigation of the dynamics of opaque colloidal suspensions. *Journal of magnetism and magnetic materials*, 289:47–49, 2005.

[102] Beatrice Ruta, S Hechler, N Neuber, D Orsi, L Cristofolini, O Gross, B Bochtler, M Frey, A Kuball, SS Riegler, et al. Wave-vector dependence of the dynamics in supercooled metallic liquids. *Physical review letters*, 125(5):055701, 2020.

[103] Beatrice Ruta, Federico Zontone, Yuriy Chushkin, Giacomo Baldi, Giovanna Pintori, Giulio Monaco, Benoit Ruffle, and Walter Kob. Hard x-rays as pump and probe of atomic motion in oxide glasses. *Scientific reports*, 7(1):3962, 2017.

[104] Alec R Sandy, Qingteng Zhang, and Laurence B Lurio. Hard x-ray photon correlation spectroscopy methods for materials studies. *Annual Review of Materials Research*, 48:167–190, 2018.

[105] Camillo Sartorio, Massimo Angiolini, Davide Flammini, Antonino Pietropaolo, Pietro Agostini, Ciro Alberghi, Luigi Candido, Marco Capogni, Mauro Capone,

Sebastiano Cataldo, et al. Preliminary assessment of radiolysis for the cooling water system in the rotating target of sorgentina-rf. *Environments*, 9(8):106, 2022.

[106] Michael J Saxton. A biological interpretation of transient anomalous subdiffusion. i. qualitative model. *Biophysical journal*, 92(4):1178–1191, 2007.

[107] Harold A Schwarz. Free radicals generated by radiolysis of aqueous solutions, 1981.

[108] Dina Sheyfer. *Structure and dynamics of glass-forming fluids*. PhD thesis, Staats- und Universitätsbibliothek Hamburg Carl von Ossietzky, 2017.

[109] Yongdae Shin and Clifford P Brangwynne. Liquid phase condensation in cell physiology and disease. *Science*, 357(6357):eaaf4382, 2017.

[110] Oleg G Shpyrko. X-ray photon correlation spectroscopy. *Journal of synchrotron radiation*, 21(5):1057–1064, 2014.

[111] Nicholas Skar-Gislinge, Fabrizio Camerin, Anna Stradner, Emanuela Zaccarelli, and Peter Schurtenberger. Cluster formation and the link to viscosity in antibody solutions. *arXiv preprint arXiv:2209.05182*, 2022.

[112] I Snook, W Van Megen, and RJA Tough. Diffusion in concentrated hard sphere dispersions: Effective two particle mobility tensors. *The Journal of Chemical Physics*, 78(9):5825–5836, 1983.

[113] Peter Sollich and Nigel B Wilding. Crystalline phases of polydisperse spheres. *Physical review letters*, 104(11):118302, 2010.

[114] Anna Stradner and Peter Schurtenberger. Potential and limits of a colloid approach to protein solutions. *Soft Matter*, 16(2):307–323, 2020.

[115] Michal Stransky, Zoltan Jurek, Carsten Fortmann-Grote, Libor Juha, Robin Santra, Beata Ziaja, Adrian P Mancuso, et al. Effects of radiation damage and inelastic scattering on single-particle imaging of hydrated proteins with an x-ray free-electron laser. *Scientific Reports*, 11(1):1–11, 2021.

[116] M Sutton. Evaluation of coherence factor for high q data, 2019.

[117] M Sutton, SGJ Mochrie, T Greytak, SE Nagler, LE Berman, GA Held, and GB Stephenson. Observation of speckle by diffraction with coherent x-rays. *Nature*, 352(6336):608–610, 1991.

[118] Dmitri I Svergun and Michel HJ Koch. Small-angle scattering studies of biological macromolecules in solution. *Reports on Progress in Physics*, 66(10):1735, 2003.

[119] Helena Taberman. Radiation damage in macromolecular crystallography—an experimentalist's view. *Crystals*, 8(4):157, 2018.

[120] Michio Tateno and Hajime Tanaka. Power-law coarsening in network-forming phase separation governed by mechanical relaxation. *Nature communications*, 12(1):912, 2021.

[121] Sonja Timmermann, Nimmi Das Anthuparambil, Anita Girelli, Nafisa Begam, Marvin Kowalski, Sebastian Retzbach, Maximilian Darius Senft, Mohammad Sayed Akhundzadeh, Hanna-Friederike Poggemann, Marc Moron, et al. X-ray driven and intrinsic dynamics in protein gels. *Scientific Reports*, 13(1):11048, 2023.

[122] Joseph J Valente, Robert W Payne, Mark C Manning, W William Wilson, and Charles S Henry. Colloidal behavior of proteins: effects of the second virial coefficient on solubility, crystallization and aggregation of proteins in aqueous solution. *Current pharmaceutical biotechnology*, 6(6):427–436, 2005.

[123] Jan Verwohlt, Mario Reiser, Lisa Randolph, Aleksandar Matic, Luis Aguilera Medina, Anders Madsen, Michael Sprung, Alexey Zozulya, and Christian Gutt. Low dose x-ray speckle visibility spectroscopy reveals nanoscale dynamics in radiation sensitive ionic liquids. *Physical review letters*, 120(16):168001, 2018.

[124] Elie Wandersman, Agnès Duri, Aymeric Robert, Emmanuelle Dubois, Vincent Dupuis, and Régine Perzynski. Probing heterogeneous dynamics of a repulsive colloidal glass by time resolved x-ray correlation spectroscopy. *Journal of Physics: Condensed Matter*, 20(15):155104, 2008.

[125] Hui Wang, Heng Jiang, Melissa Van De Gucht, and Mark De Ridder. Hypoxic radioresistance: can ros be the key to overcome it? *Cancers*, 11(1):112, 2019.

[126] Ying Wang, Aleksey Lomakin, Ramil F Latypov, Jacob P Laubach, Teru Hideshima, Paul G Richardson, Nikhil C Munshi, Kenneth C Anderson, and George B Benedek. Phase transitions in human igg solutions. *The Journal of chemical physics*, 139(12), 2013.

[127] E Weckert, K Balewski, W Brefeld, W Decking, W Drube, H Franz, P Gürtler, U Hahn, J Pflüger, H Schulte-Schrepping, et al. Petra iii: A new high brilliance synchrotron radiation source at desy. In *AIP Conference Proceedings*, volume 705, pages 73–76. American Institute of Physics, 2004.

[128] Edgar Weckert. The potential of future light sources to explore the structure and function of matter. *IUCrJ*, 2(2):230–245, 2015.

[129] Eric R Weeks, John C Crocker, Andrew C Levitt, Andrew Schofield, and David A Weitz. Three-dimensional direct imaging of structural relaxation near the colloidal glass transition. *Science*, 287(5453):627–631, 2000.

[130] Simon P Wolff, Anthony Garner, and Roger T Dean. Free radicals, lipids and protein degradation. *Trends in biochemical sciences*, 11(1):27–31, 1986.

[131] Zhen Wei Wu, Walter Kob, Wei-Hua Wang, and Limei Xu. Stretched and compressed exponentials in the relaxation dynamics of a metallic glass-forming melt. *Nature communications*, 9(1):5334, 2018.

[132] Katharina Wylon, Sabine Dölle, and Margitta Worm. Polyethylene glycol as a cause of anaphylaxis. *Allergy, Asthma & Clinical Immunology*, 12(1):1–3, 2016.

[133] Isseki Yu, Takaharu Mori, Tadashi Ando, Ryuhei Harada, Jaewoon Jung, Yuji Sugita, and Michael Feig. Biomolecular interactions modulate macromolecular structure and dynamics in atomistic model of a bacterial cytoplasm. *elife*, 5:e19274, 2016.

[134] Emanuela Zaccarelli. Colloidal gels: Equilibrium and non-equilibrium routes. *Journal of Physics: Condensed Matter*, 19(32):323101, 2007.

[135] Jixiang Zhu, P Chaikin, Min Li, WB Russel, R Rogers, W Meyer, and RH Ottewill. Hard spheres in space: Light scattering from colloidal crystals in microgravity. *Light Scattering and Photon Correlation Spectroscopy*, pages 387–387, 1997.

# Erklärung

Hiermit erkläre ich, dass ich die vorliegende Arbeit mit dem Titel "Röntgenphotonen-Korrelationsspektroskopie-Experimente zur Proteindynamik auf molekularen Längenskalen - Möglichkeiten und Grenzen." selbständig und ohne unzulässige Hilfe angefertigt habe. Alle benutzten Quellen und Hilfsmittel sind angegeben und in der Arbeit verzeichnet. Die Arbeit wurde bisher keiner anderen Prüfungsbehörde vorgelegt oder veröffentlicht.

Ort, Datum:.....

Unterschrift:.....

Akhundzadeh Mohammad Sayed